Ultraviolet line-driven disc winds as a feedback mechanism in bright active galactic nuclei

ARNAU QUERA-BOFARULL

Ultraviolet line-driven disc winds as a feedback mechanism in bright active galactic nuclei

Arnau Quera-Bofarull

Abstract: Astronomical observations have shown that galaxies and the supermassive black holes (BH) located at their centres have evolved together over cosmic time. BH grow by accreting matter from their surroundings and the gravitational potential energy released by the infalling matter can power the enormous luminosities we see in active galaxies and quasars, and is in principle sufficient to significantly disrupt the structure of the host galaxy. However, the particular physical processes through which such active galactic nuclei feedback affects the host galaxy are still poorly understood. One possibility is that the accretion process powers winds that travel through the galactic bulge, displacing the gas reservoir and thus quenching star formation in the galaxy. There are various mechanisms that could drive such winds. In this thesis, we focus on the study of UV line-driven winds originating from the surface of accretion discs, which are driven by radiation pressure on spectral lines and are also present in hot stars. We develop a numerical simulation method for the study of such systems, building up on existing models and incorporating modern computational techniques to study the conditions under which these winds can be launched and accelerated. The resulting model, called Qwind, features relativistic corrections to the radiation flux, as well as an algorithm to perform ray tracing on axisymmetric geometries. We also develop a model to compute the initial conditions to launch the wind from the surface of the accretion disc, based on theoretical frameworks employed in the study of O-star winds. Using this new model, we are able to investigate the dependence of the wind properties on the BH mass, mass accretion rate, and the innermost launching radius of the wind, thus deriving the amount of momentum and energy carried by the wind for different AGN systems.

Ultraviolet line-driven disc winds as a feedback mechanism in bright active galactic nuclei

Arnau Quera-Bofarull

A thesis presented for the degree of
Doctor of Philosophy

Institute for Computational Cosmology
Department of Physics
Durham University
United Kingdom

April 2022

Dedicat als meus pares

It has been said that astronomy is a humbling and character-building experience. There is perhaps no better demonstration of the folly of human conceits than this distant image of our tiny world. To me, it underscores our responsibility to deal more kindly with one another, and to preserve and cherish the pale blue dot, the only home we've ever known.

Carl Sagan

Contents

List of Figures

List of Tables

Declaration

The work in this thesis is based on research carried out in the Institute for Computational Cosmology, Department of Physics, Durham University, United Kingdom. No part of this thesis has been submitted elsewhere for any other degree or qualification and it is all my own work unless referenced to the contrary in the text.

The content presented in chapter 3 has been publised in

Quera-Bofarull, A., Done, C., Lacey, C., et al. *Qwind code release: a non-hydrodynamical approach to modelling line-driven winds in active galactic nuclei.* Monthly Notices of the Royal Astronomical Society, 495(1), 402. (2021)

The content presented in chapter 4 is undergoing peer review and an arXiv pre-print is accessible,

Quera-Bofarull, A., Done, C., Lacey, C., et al. *Qwind3: UV line-driven accretion disc wind models for AGN feedback.* arXiv e-prints, 2021arXiv211102742Q (2021)

The author has had a major contribution to the content summarised in chapter 6, with part of the work publised in

1. Aylett-Bullock, J., Cuesta-Lázaro, C., and **Quera-Bofarull, A.** *XNet: a convolutional neural network (CNN) implementation for medical x-ray image segmentation suitable for small datasets.* Medical Imaging 2019: Biomedical Applications in Molecular, Structural, and Functional Imaging vol 10953 (SPIE) pp 453–63 (2019)

2. Aylett-Bullock, J., Cuesta-Lázaro, C., **Quera-Bofarull, A.**, et al. *June: open-source individual-based epidemiology simulation.* Royal Society Open Science 8 210506 (2021)

3. Aylett-Bullock, J., Cuesta-Lázaro, C., **Quera-Bofarull, A.**, et al. *Operational response simulation tool for epidemics within refugee and IDP settlements: A scenario-based case study of the Cox's Bazar settlement.* PLOS Computational Biology 17 e1009360 (2021)

and an additional submission awaiting peer review, that can be accessed on medRxiv,

Cuesta-Lázaro, C., **Quera-Bofarull, A.**, Aylett-Bullock, J., et al. *Vaccinations or Non-Pharmaceutical Interventions: Safe Reopening of Schools in England.* medRxiv (2021).

The author of the thesis was primarily responsible for all aspects of this publication.

Acknowledgements

First and foremost, to Cedric and Chris. I'm grateful for the guidance provided during these years and for the support in my pursue of academic projects outside Astronomy.

To my colleagues at Ibex and Boeing, who made working in industry an absolute joy, especially to Millie for the provision of hops and the countless postcards.

To Ken for hosting me in Tsukuba University, and to all the friends I made during my magical stay in Japan.

To the JUNE team, Bryan, Frank, Henry, Ian, James, Joe, Julian, Kevin, Richard, Tristan, for turning a global pandemic into a fascinating scientific project.

To the COSMA team, for making HPC easier.

To my political tribe, Concha, Ludo, Queralt, Roger, Ryan, Tobias, Uri, thank you for all the pub nights that sometimes turned into productive discussions.

To the people that kept me moving, the Red Ramblers and the Ustinov football and ultimate teams.

To my astronomy colleagues, I can't name you all but you know who you are. Especial shout-out to my office mates, Aidan, Giorgio, Joaquin, Ra'ad, Raj, Willem.

To the Durham Data Miners, for making my first year at Rochester much more enjoyable!

To my housemates that made it feel like home, Bartek, Christoph, Dylan, Ellen, Miguel, Nick. To Tilly, for being an amazing lockdown companion.

To my travelling pals: Alan, Bex, Gao, Holly, James, Kevin, Mel, Ryan. I'll always be grateful for making this last year such a special one.

To Sara, for always being there. To Pep, for the long walks, the good food, and the good chats. To Carol, I will surely miss you.

To my family for the unconditional support throughout all these years, thank you for making me who I am.

I was supported by the STFC studentship ST/P006744/1 and the JSPS London Pre / Postdoctoral Fellowship for Foreign Researchers.

This work used the DiRAC@Durham facility managed by the Institute for Computational Cosmology on behalf of the STFC DiRAC HPC Facility (www.dirac.ac.uk). The equipment was funded by BEIS capital funding via STFC capital grants ST/K00042X/1, ST/P002293/1, ST/R002371/1 and ST/S002502/1, Durham University and STFC operations grant ST / R000832/1. DiRAC is part of the National e-Infrastructure.

This thesis made use of the Python (Van Rossum & Drake, 2009) and the following Python libraries: numpy (Harris et al., 2020), scipy (Virtanen et al., 2020), numba (Lam et al., 2015), and science plots (Garrett, 2021). This thesis also made use of the Julia programming language (Bezanson et al., 2017), and the following julia packages: ConcaveHull.jl (Stagner, 2021) and DifferentialEquations.jl (Rackauckas & Nie, 2017).

Chapter 1

Introduction

1.1 The Lambda-CDM paradigm

The ΛCDM model, also known as the standard cosmological model, is the current established physical theory that describes the evolution of the Universe up to the present day. The model assumes that the Universe is homogeneous and isotropic when observed at large enough scales, a hypothesis known as the cosmological principle. It also supposes that general relativity is the correct theory of gravity, explaining the accelerated expansion of the Universe (Riess et al., 1998) as a cosmological constant (Λ) or vacuum energy in Einstein's field equations. The model requires the existence of a form of matter that interacts solely with the gravitational field, with very weak coupling to the other forces. Such matter is known as dark matter (Zwicky, 1933; Rubin et al., 1980), and is not explained by the current Standard Model of particle physics (Bertone et al., 2005). Despite our lack of understanding of the nature of the physical components of the ΛCDM paradigm, the model has been widely successful in accounting for a diverse range of observations of the cosmos, from the structure of the cosmic microwave background (Planck Collaboration et al., 2016) to the large scale distribution of galaxies in the observable Universe (Percival et al., 2007).

1.1.1 Galaxy formation and evolution

Under the ΛCDM paradigm, quantum fluctuations in the primordial state of the Universe lead to the development of matter over-densities over large scales. These over-densities are primarily a consequence of dark matter clumping (Davis et al., 1985), since they are the most abundant form of matter. Gravitationally bound dark matter haloes can continue to

grow by accreting matter to them or by merging with other haloes (Lacey & Cole, 1993). Mostly guided by the gravitational potential set by the dark matter particles, baryonic matter eventually cools down enough to start collapsing into the first stars (Grudić et al., 2021) and thus form the first galaxies. The observed diversity in galaxy shapes and colours is then a consequence of their particular evolution history in their environments (Snyder et al., 2015). For instance, it is currently believed that elliptical galaxies are a consequences of mergers between smaller galaxies (Kormendy et al., 2009), while the spiral arms in spiral galaxies are produced by density waves along the galaxy plane (Lin & Shu, 1964).

1.1.2 The galaxy - halo mass function miss-match

A useful way of looking at the distribution of dark and baryonic matter in the Universe is to look at their mass functions, that is, the number density of bound objects of that kind of matter per logarithmic mass interval. Given that we would expect baryons to just follow the gravitational potential that is mostly set by dark matter particles, we would naively assume that inside a dark matter halo of mass $M_{\rm h}$ we have, at most, $f_{\rm b}M_{\rm h}$ mass in stars, where $f_{\rm b}$ is the mass fraction of baryons. In Figure 1.1, we show the halo mass function measured from cosmological simulations in Tinker et al. (2008) multiplied by $f_{\rm b}$, which we take to be approximately 0.1 (Crain et al., 2007), and we compare it to the observed stellar mass function from Baldry et al. (2012). As we can see, both the low and high tails of the stellar mass function are significantly supressed at both ends of the considered mass range compared to the halo mass function. Substantial research effort has gone, and continues to go, to explaining this discrepancy. The consensus in the literature is that the supression of the lower mass tail is caused by supernova feedback (Dekel & Silk, 1986). Supernova explosions that take place at the end of the stars' lifetime can carry enough energy to displace a significant fraction of the galaxy's gas reservoir outside the galaxy, negating further star formation and thus reducing the number of observed galaxies at the lower mass end. This is most effective in galaxies with lower stellar masses, where the gravitational potential is smaller, and thus the supernovae explosions can easily displace the gas. As for the discrepancy at the high end tail, it is common to postulate active galactic nuclei (AGN) feedback as its cause (Croton et al., 2006).

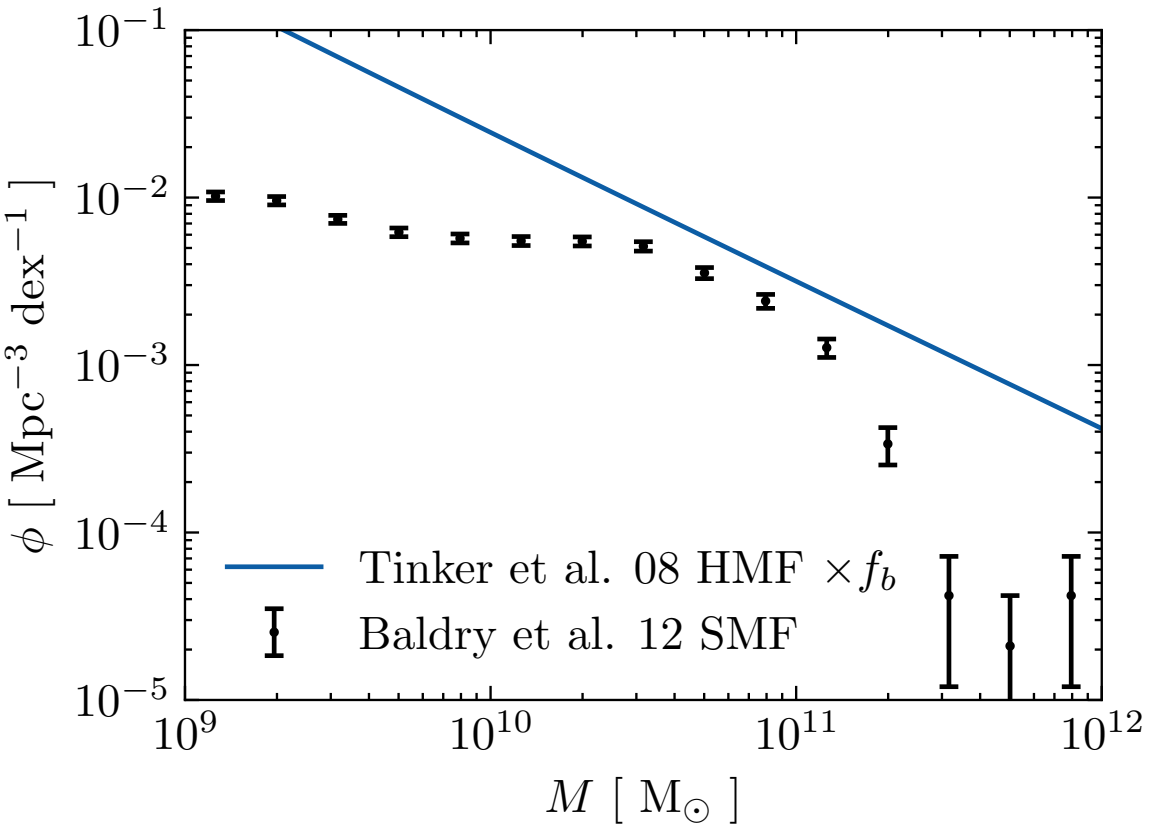

Figure 1.1: Halo mass function (HMF) from Tinker et al. (2008) and stellar galaxy mass function (SMF) from Baldry et al. (2012). The HMF has been multiplied by a baryon fraction of $f_b = 0.1$ (Crain et al., 2007) to illustrate the expected maximum number of baryonic matter that a halo should contain.

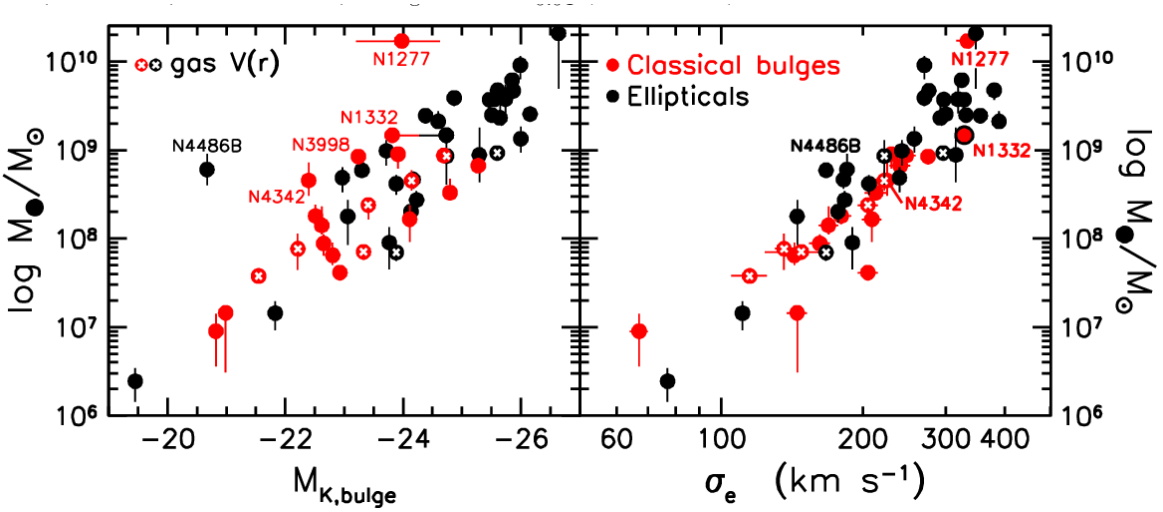

Figure 1.2: Black hole mass and bulge velocity dispersion data from Kormendy & Ho (2013)

1.2 Supermassive black holes and galaxies

The most central parts of high-mass galaxies tend to be occupied by a supermassive black hole (BH). There is a wide range of physical phenomena, mostly connected to BH accretion, that takes place around these BHs, and some of them, namely jets and winds, can have far-reaching impact in the galaxy structure. Similar to supernova feedback, the resulting effect of these phenomena on the galaxy is to empty it from its gas reservoir and preventing its cooling, diminishing the star formation rate and thus the amount of mass in stars. Since we observe more massive galaxies to also host more massive black holes, this effect is enhanced in the upper end of the galaxy mass distribution.

There are multiple observations that support a joint evolution between the BH and its host galaxy. This fact is in principle surprising given the massive difference in the scales involved: the Schwarzschild radius of Sagittarius A* is of the order of 10^{11} cm, while the radius of the Milky Way's bulge is of the order of 10^{21} cm. In Figure 1.2, we show a figure from Kormendy & Ho (2013) where we can see an observed correlation between the galaxy's central BH and the galactic bulge mass and velocity dispersion. The fact that these correlations hold for a wide range of BH masses suggests that there is a physical coupling between the BH and the galactic bulge, or that they both share a common component (such as common gas supply) that enables them to co-evolve together over cosmic time. These correlations, however, do not tell us much about what particular physical processes are responsible for the coupling between the two systems, thus making the study of AGN feedback channels a very active field of research (Fabian, 2012).

1.2.1 Active Galactic Nuclei

When BHs at the centre of galaxies grow through gas accretion, they release a very high amount of energy, making them visible in multiple radiation bands. This is indeed what Edward A Fath discovered in 1908 when he was studying the spectrum of the nearby galaxy NGC 1068 (Fath, 1909). Since the first observation made by Fath, the term AGN is used to refer to regions at the centres of galaxies where the luminosity emitted in a certain radiation band is much higher than the amount expected from the galactic stars' component.

The origin of the radiative emission from AGN was not always clear and was intensely debated. Initially thought to be supermassive stars (Hoyle & Fowler, 1963), the overwhelming consensus nowadays is that the many phases of BH accretion can explain the observed characteristics of AGN.

AGN can exhibit very different features in different energy bands and this has lead to a classification of AGN into a wide variety of categories depending on the observed characteristics (Urry & Padovani, 1995). The question then arises about the origin of such variation and whether it is an observational effect or a fundamental characteristic in the system at hand. The unified AGN model proposed in Urry & Padovani (1995) suggests that the angle at which we observe an AGN can explain the variance in many of the observed features, as we illustrate in Figure 1.3, taken from the same work. The unified AGN model proposes that, along certain lines of sight, obscuration by a dusty torus would prevent the optical emission from the inner accretion disc to be visible, as opposed to face on observations. Despite the success of the unified model in accounting for the variance in the spectrum data, not all observations can be explained by this model (Netzer, 2015), and there are possibly many other processes that control the emission like the gaseous environment in the galactic centre.

1.2.2 Active Galactic Nuclei feedback

As we hinted in subsection 1.1.2, the central BHs at the centres of galaxies are thought to be responsible for suppressing the higher mass tail of the galaxy stellar mass function. The action in which the AGN affects its host galaxy is known as AGN feedback, with the name capturing the fact that the BH accretion process can produce outflows or radiation with the capacity to alter the galactic structure.

We currently have access to a diverse range of observations providing evidence for the existence of AGN feedback (Fabian, 2012). The analysis of the data suggests two distinct modes

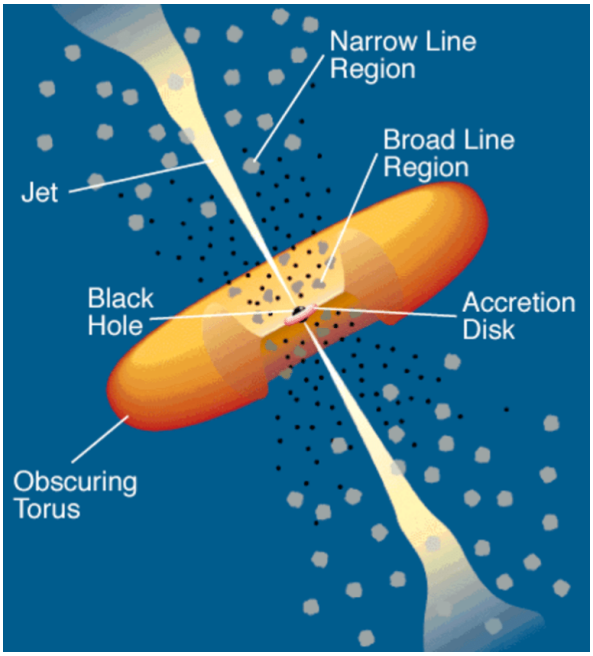

Figure 1.3: Schematic representation of the AGN standard model. Different observed types of AGN are mostly a consequence of the observer's viewing angle (Urry & Padovani, 1995). The broad-line region (BLR) and the narrow-line region (NLR) are the spatial regions where broad and narrow features in AGN spectra are thought to be produced.

of AGN feedback: the quasar mode, prevalent at high accretion rates, and the jet mode, more dominant at lower accretion rates.

In the jet mode, the radio component of the AGN provides the main source of energy launching a jet that travels to extra-galactic scales, heating the gas and preventing it to cool down back to the galaxy. A very clear observation of this phenomenon taking place is the galaxy cluster MS0735.6+7421, shown in Figure 1.4. The radio emission detected by the Very Large Array telescope (Condon et al., 1998) tracks the the relativistic particles in lobes accelerated by the jet (red). The interaction of the high energy particles with the surrounding gas heats the latter to high temperatures, making it visible on the X-ray band, as detected by the X-ray Chandra observatory (Beasley, 2005) (blue). The increased heating prevents the collapse of the gas, stopping it from forming new stars and thus reducing the star formation rate of the galaxy. This feedback channel has also been successful at explaining other observations, such as the rates of gas cooling in galaxy clusters (Peterson et al., 2003).

The quasar (QSO) mode feedback gets its name from QSO, which are the most luminous class of AGN in the Universe. This feedback channel is harder to observe directly than the jet mode because its action is limited to the central parts of the galaxy, in the galactic bulge. Nonetheless, multiple observations of AGN outflows have been made to date (Weymann et al.,

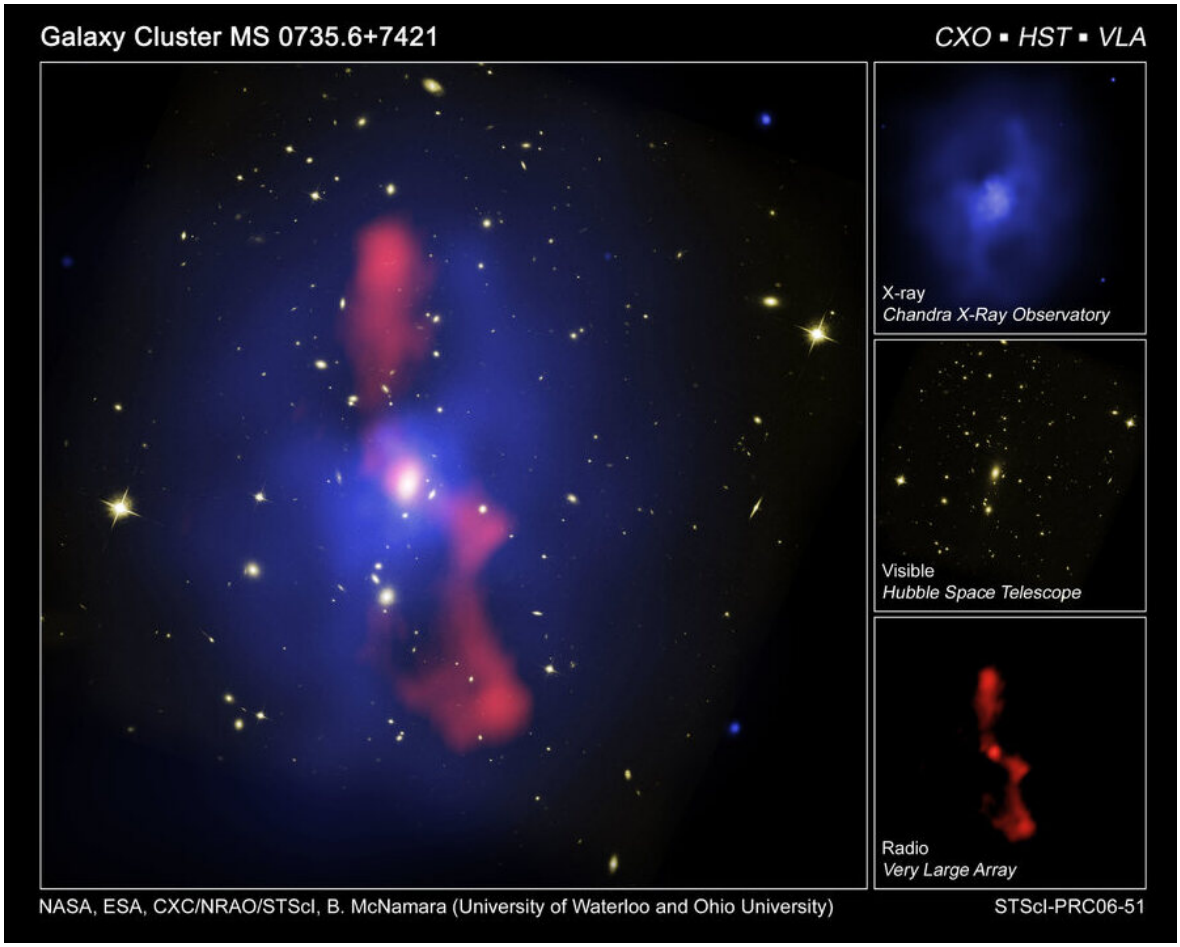

Figure 1.4: Galaxy Cluster MS 0735.6+7421 shown in 3 different energy bands: X-ray, visible, and radio.

1991; Ganguly et al., 2007; Liu et al., 2013). The QSO mode is thought to operate during periods of rapid BH accretion (Silk & Rees, 1998). The high luminosity of the system can power radiatively driven winds that escape the gravitational pull of the BH, reach galactic scales, and empty the cold gas reservoir. Furthermore, it has been shown that it is possible to explain the correlation between BH mass and bulge properties (Figure 1.2) through the effect of these BH generated outflows (Murray et al., 1995). While this feedback channel is capable of shutting down star formation, it is likely insufficient to account for the full dampening of the high mass end of galaxy mass function (Gabor et al., 2011; Bower et al., 2012).

1.2.3 Cosmological simulations

In recent times, the use of computer simulations in astronomical research has been of paramount importance. In particular, modern cosmology relies on simulations that aim to cover the entire history of the Universe, starting from a set of initial conditions and comparing the derived

observables to data as the simulation advances through cosmic time. The dynamic range over which relevant physical processes operate in the Universe is extremely large. For example, we have discussed earlier that galaxy evolution may be affected by BHs that are 10 orders of magnitude smaller in radius than their host galaxies. Likewise, particular galactic events can affect the evolution of entire clusters of galaxies. The impossibility of resolving all these physical processes in a single cosmological simulation is one of the most important challenges of modern computational cosmology.

Currently, the only way to deal with AGN feedback in cosmological simulations is to use sub-grid prescriptions, that is, to use some kind of formula to capture the transfer of energy between the AGN and their surroundings as a function of physical properties that are resolved by the cosmological simulation (Bower et al., 2006; Croton et al., 2006; Choi et al., 2012). Such prescriptions can be derived from smaller scale simulations, theoretical arguments, or heuristic formulations. The particular choice of a subgrid model can have a substantial effect on the results of the cosmological simulation (Sutter & Ricker, 2010). Furthermore, many of these subgrid models need to be calibrated to reproduce observable quantities, thus limiting the predictive power of cosmological simulations (Vogelsberger et al., 2014; Schaye et al., 2015; Davé et al., 2019a; Hopkins et al., 2018).

It is thus necessary to further develop subgrid models that are based on first physical principles, so that they can accurately produce physical outputs as a function of parameters that can be resolved in bigger simulations. Likewise, developing these models is also beneficial for BH specific research, since it sheds light on how these systems evolve as a function of their environment.

1.3 Black hole accretion

Through the study of compact objects in the Universe such as BHs and neutron stars, we now know that accretion plays a central role in powering many astronomical systems. The release of energy in accretion is a consequence of the conversion of gravitational potential energy into radiation, thus making it more relevant in systems where the gravitational potential is high. Given a body of mass M and radius R, the gravitational potential energy released by the accretion of another body of mass m to the surface of the first body is

$$\Delta E_{\rm p} = GMm/R. \tag{1.3.1}$$

Assuming a circular orbit, the kinetic energy of the body m at radius R is $1/2GMm/R$, which means that about a half of the gravitational potential energy has been radiated away before it is captured onto the BH. If we consider a non-rotating BH with $M = 10^8 \mathrm{M}_\odot$ and take R to be the innermost stable circular orbit (ISCO), $R = 6\ GM/c^2$, then the energy released per unit mass is $\Delta E/m \simeq 0.75 \times 10^{20}$ erg g^{-1}, or equivalently, $\eta = \Delta E/(mc^2) \simeq 1/12$. For comparison, nuclear fusion of hydrogen in stars gives $\eta = 0.007$, making accretion about 10 times more efficient in converting mass to energy than nuclear fusion, explaining why AGN can exhibit such high luminosities. The energy released by accretion thus depends on the compactness of the object (M/R) and on the amount of available mass to accrete (m). The naively derived efficiency of $\eta = 1/12 \simeq 0.083$ is clearly a simplification, a more careful derivation considering general relativity effects and angular momentum as well gives $\eta = 0.057$ for a non-rotating BH and $\eta = 0.4$ for a maximally rotating BH (Thorne, 1974). The luminosity produced by accretion is then given by

$$L = \eta \dot{M} c^2, \tag{1.3.2}$$

where $\dot{M}$ is the mass accretion rate.

It is worth now considering if BH accretion can alter the structure of the galactic bulge and thus be a good candidate for AGN feedback. The binding energy of a galaxy bulge with $M_{\mathrm{bulge}} = 10^{11} M_\odot$ and velocity dispersion $\sigma_v = 200$ km / s is

$$E_{\mathrm{binding}} \ \simeq \ M_{\mathrm{bulge}}\, \sigma_v^2 \ \simeq \ 10^{58} \text{ erg}. \tag{1.3.3}$$

On the other hand, the energy released by the accretion process of a BH with $M_{\mathrm{BH}} = 10^8 M_\odot$ is (taking $\eta = 0.1$)

$$E_{\mathrm{acc}} \ \simeq \ 0.1 M_{\mathrm{BH}} c^2 \ \simeq \ 10^{61} \text{ erg}, \tag{1.3.4}$$

showing that the energetics of accretion are more than capable of impacting the galactic bulge. The question that remains is whether the energy released from accretion can effectively couple to the AGN surrounding material and affect the galaxy structure.

1.3.1 The Eddington Limit

The electromagnetic radiation generated by accretion couples to the material being accreted, transferring part of its momentum and thus pushing it away from the BH. Therefore, we find a limit on the amount of mass per unit time that can be accreted. Considering a system with spherical symmetry, and assuming that the radiation couples to the material through electron

Thomson scattering (with cross-section $\sigma_{\rm T}$), then the net inward force on an electron-proton pair at a distance r from the BH is

$$F = \frac{1}{r^2}\left(GMm_{\rm p} - \frac{L\sigma_{\rm T}}{4\pi c}\right), \tag{1.3.5}$$

the condition that the material can transfer inwards is then $F > 0$, so that $F = 0$ yields a theoretical limit for the luminosity

$$L_{\rm Edd} = \frac{4\pi GMm_{\rm p}c}{\sigma_{\rm T}}, \tag{1.3.6}$$

which is commonly know as the Eddington luminosity. It is worth noting that the Eddington limit applies to spherically symmetric steady ionised flows, so in many cases this limit may not be satisfied. However, it is still useful to consider it in practice, since many systems change behaviour when they approach this limit, even though they may not exactly satisfy the conditions under which we have derived it. The Eddington mass accretion rate is defined as $\dot{M}_{\rm Edd} = L_{\rm Edd}/(\eta c^2)$, where η is a function of BH spin.

1.3.2 The standard model of black hole accretion

In our naive derivation of the energy released by accretion (equation 1.3.1), we have not considered how infalling matter can lose its energy and angular momentum so it can be transported inwards. Due to the conservation of angular momentum, the infalling mass forms an accretion disc around the BH, but to move further in at some point the gas needs to lose angular momentum. Salpeter and Zeldovich (Salpeter, 1964; Zel'dovich, 1964) proposed that hydrodynamic turbulence can transport angular momentum outwards, but this has shown to be insufficient (Pringle, 1981). The current established alternative is the magnetorotational instability (MRI) (Balbus & Hawley, 1998), in which the gas viscosity is enhanced by the presence of a magnetic field dynamo, effectively transporting angular momentum outwards. Other options are also considered, where the presence of an outflow can remove mass, energy, and angular momentum from the disc (Blandford & Payne, 1982; Knigge, 1999).

Shakura and Sunyaev (Shakura & Sunyaev, 1973) developed what would become the standard model of black hole accretion, usually referred to as the SS solution. The SS solution parametrises the effective viscosity in a practical way without considering the particular physical mechanism involved in the transport of angular momentum. Therefore the effective viscosity is defined as

$$\nu = \alpha H c_{\rm s}, \tag{1.3.7}$$

where H is the disc height, c_s is the speed of sound, and α is a free parameter. Fitting to observations suggests that α is in the range $0.1 - 0.4$, although this value is not recovered when performing magnetohydrodynamics simulations of thin discs, revealing a gap in our understanding of disc accretion King et al. (2007). Together with the assumption that the accretion disc is steady, geometrically thin, and optically thick, one can then derive (see, e.g. (Frank et al., 2002)) the SS disc solution, describing the properties of the disc as a function of the BH mass, mass accretion rate, α, and radius. Of particular interest is the obtained surface temperature profile as a function of radius, given by

$$\sigma_{\rm SB} T^4(R_d) = \frac{3GM\dot{M}}{8\pi R_d^3} f(R_{\rm d}, R_{\rm isco}), \tag{1.3.8}$$

where $\sigma_{\rm SB}$ is the Stefan-Boltzmann constant, $\dot{M}$ is the mass accretion rate, $R_{\rm d}$ is the disc radius, $R_{\rm isco}$ is the innermost stable orbit, and f is a function that takes into account inner boundary effects in the disc and relativistic corrections (Novikov & Thorne, 1973). Note that this expression does not depend on the value of α, conveniently.

We can then derive the disc spectral energy distribution (SED) as a collection of black-bodies at different temperatures given by equation 1.3.8. For high BH masses, this results into the disc spectrum peaking at the UV for high accretion rates. We illustrate this in Figure 1.5, where we plot the peak disc energy, calculated using Wien's displacement law, as a function of BH mass and Eddington fraction, $\dot{m} = \dot{M}/\dot{M}_{\rm Edd}$. As we can see, for the range $M_{\rm BH} > 10^6 M_\odot$, the accretion disc emits most of its luminosity in the UV band, which we take to be $(4 - 60)$ eV.

Observations of AGN reveal that the accretion disc is not the only radiation emitting component of an AGN. In Figure 1.6, we show a schematic representation of the AGN SED, highlighting the hypothesised origin of each individual radiation component. At the lower energy range, we have infrared emission resulting from the dusty torus and radio emission that is typically less intense than the host galaxy level except for the most powerful radio loud AGN. At higher energies, two X-ray Compton components are needed to accurately model the observed spectrum. The origin and importance of such components is discussed in the next section.

1.3.3 The origin of the X-ray emission

The origin of the X-ray emission across the BH mass range is still under debate. Early observations of X-ray binaries (XRB) (Tananbaum et al., 1972) revealed that XRB can switch

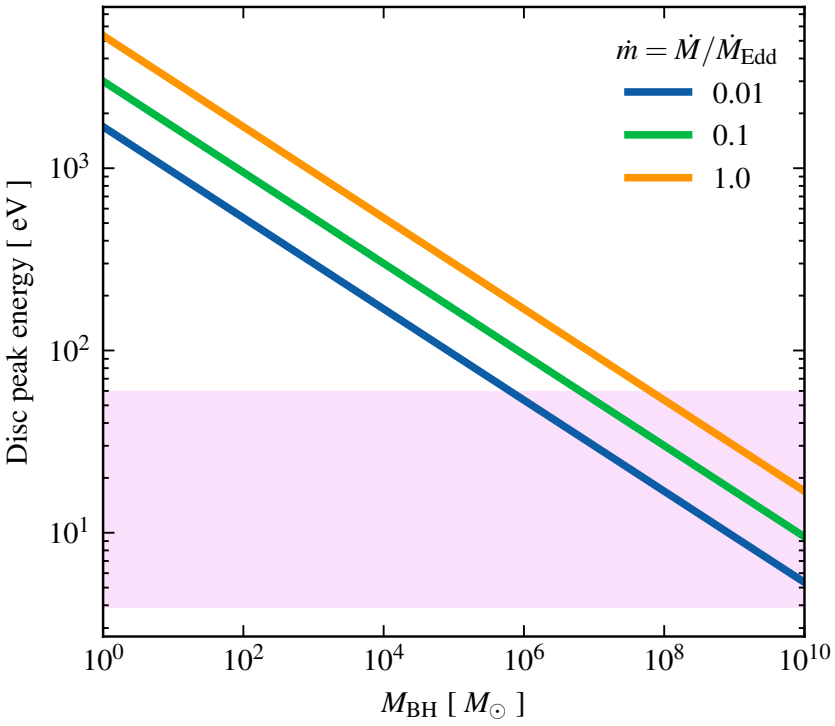

Figure 1.5: Peak energy of the accretion disc emission as a function of BH mass and accretion rate. The violet colour zone denotes the UV band $(4 - 60)$ eV.

to a hard spectral state which requires the accreting gas to be hot and optically thin, in contrast with the SS thin disk solution, which is optically thick. Similarly, low-luminosity AGN systems are observed to have a lack of UV emission compared to the expected amount given by the SS solution and a substantial hard X-ray and radio emission, which again suggests that the inner part of the accretion disc has been replaced by a hotter optically thick flow (Ho, 1999; Quataert et al., 1999; Nagar et al., 2000).

Two-temperature plasma solutions for accretion discs were first proposed by Shapiro et al. (1976), but were later shown to be thermally unstable (Pringle, 1976). A second attempt are advection-dominated accretion flows (ADAF) (Narayan & Yi, 1994, 1995; Abramowicz et al., 1995), which are also known as radiatively inefficient accretion flows (RIAF). These flows are shown to be thermally stable (Kato et al., 1997), and are thus a good candidate to model low-luminosity BH accretion.

The main difference between the thin disc and the ADAF solutions is the efficiency of radiative cooling. While in the SS solution we assume that viscous heating is balanced by radiative cooling (giving rise to the previously presented temperature profile), most of the viscous heat remains trapped in the gas in the ADAF case and the energy is advected inwards. The increased temperature makes the disc geometrically thick and optically thin, so the radiation

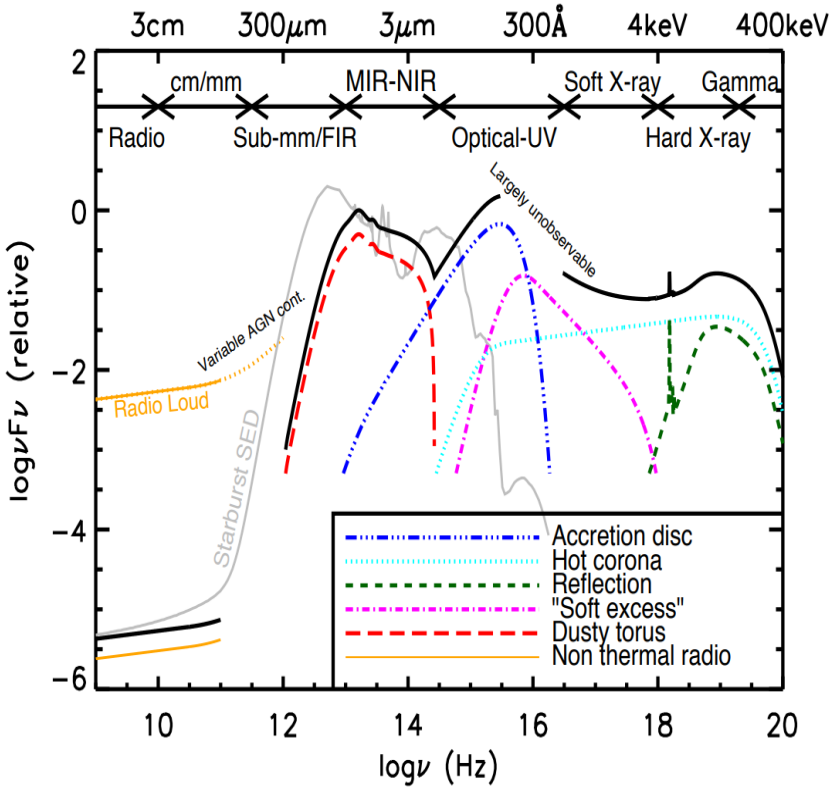

Figure 1.6: Schematic representation of a typical AGN SED taken from Harrison (2014). The different colours denote the different radiation emitting components of the AGN, while the black and grey line represent the total emission from the AGN and a starburst galaxy respectively.

from the hot electrons (at $T \sim 100$ keV) is produced primarily by thermal Comptonisation.

Combining the ADAF and the SS solution, it is possible to understand the various spectral states of XRBs (Narayan et al., 1996; Esin et al., 1997). For high accretion rates, the system is composed of a thin disk with a corona component composed of hot electrons. These electrons then scatter the soft X-ray photons from the accretion disc, generating hard X-rays by Compton scattering (Haardt & Maraschi, 1991; George & Fabian, 1991; Svensson & Zdziarski, 1994). Simultaneously, the high-energy photons produced in the corona are effective in heating up the disc (reprocessing). This modelling solution can then explain observations well (Haardt & Maraschi, 1993).

In the case of AGN, the situation is a bit more complicated since the emission cannot be explained by a thin disc and a corona alone. There is a soft X-ray excess component, which can be fit by a second Comptonisation region with very different parameters than the hard X-ray corona component (Magdziarz et al., 1998; Czerny et al., 2003; Done et al., 2012; Petrucci et al., 2018). Recent results have shown that this component cannot be the results of reflection (Mehdipour et al., 2011). The fact that such component is only needed in AGN, where the disc emission is peaking in the UV energy range, suggests that the warm Compton region may be related to UV physics taking place near the disc, such as UV line-driven winds (see chapter 2) or changes in the disc structure caused by enhanced radiative opacities (Hameury et al., 2009). Even though the origin of the X-ray emission is not completely understood, phenomenological models can reproduce the observed spectra through a wide range of BH parameters (Kubota & Done, 2018).

1.4 Accretion disc outflows

We can distinguish two kinds of outflows that have their origin on the process of BH accretion. On the one hand, we have relativistic jets which are highly collimated streams of relativistic particles usually travelling perpendicular to the accretion disc. On the other hand, we have outflows in the form of winds, that have high covering factors launching from a wide range of disc radii. They usually have a smaller velocity than jets but can transport a higher mass rate. In this section we focus on winds since they are the relevant topic for this thesis.

Winds are ubiquitously observed across a wide range of accreting BH systems with different BH masses. For small BH masses, we observe winds in XRB accreting at the soft state (Ponti et al., 2012) and in cataclysmic variables (Heap et al., 1978; Greenstein & Oke, 1982; Cordova

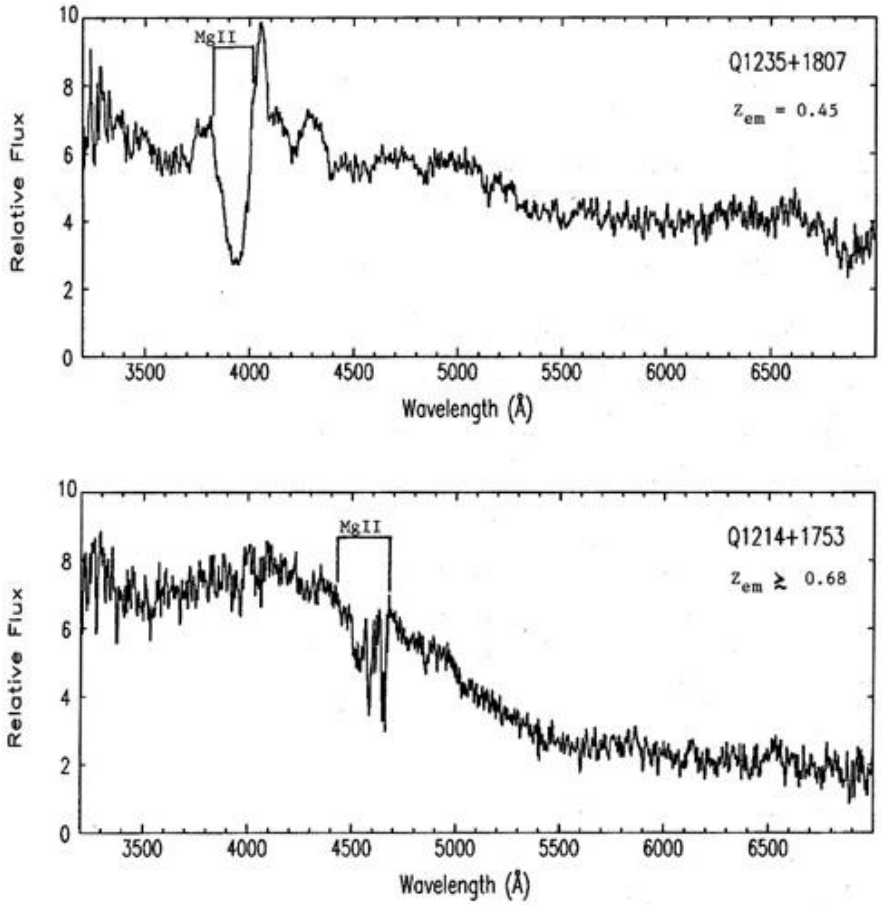

Figure 1.7: Spectra of two QSO exhibiting BAL features. Image taken from Blades et al. (1988) based on the data from the APM QSO survey (Foltz et al., 1987a).

& Mason, 1982). For larger BH masses, winds are observed in broad apsorption line (BAL) QSOs, that compose 10-20% of the QSO population (Weymann et al., 1991; Voit et al., 1993; Pounds et al., 2003b,a; Knigge et al., 2008; Reeves et al., 2009; Crenshaw & Kraemer, 2012; Tombesi et al., 2010). BAL QSOs are QSOs that exhibit broad absorption lines in their spectra. The absorption troughs are thought to be a signature of an outflow, which would also explain that we only observe BAL in a small fraction of QSO, since we only see it from angles that are consistent with the wind covering factor. An example of two BAL QSO is shown in Figure 1.7.

Winds in AGNs are also detected by the presence of X-ray absorption due to partially ionised gas (a feature known as warm absorbers) (Reynolds & Fabian, 1995). A particular class of winds is observed to have remarkably high velocities, $> 0.05c$, (Reeves et al., 2009; Pounds et al., 2003b) which makes them known as ultra-fast outflows (UFOs). UFOs are particularly important because their high velocity and column densities make them a good candidate for AGN feedback (Gofford et al., 2015; Hopkins & Elvis, 2010). Finally, winds are also observed

at larger scales in galaxies via molecular emission lines (Walter et al., 2002; Iono et al., 2007).

Depending on the physical mechanism that is responsible of driving the wind, we can distinguish different kinds of winds. It is useful to write the fluid momentum equation of magneto-hydrodynamics,

$$\rho \frac{D\mathbf{v}}{Dt} = -\nabla P + \frac{1}{4\pi}(\nabla \times \mathbf{B}) \times \mathbf{B} + \rho \left(\mathbf{a}_{\text{rad}} + \mathbf{a}_{\text{grav}}\right) \tag{1.4.1}$$

where bold letters denote vector quantities, D denotes the comoving derivative, ρ the gas density, P the gas pressure, B the magnetic field strength, and $\mathbf{a}_{\text{rad}}$ and $\mathbf{a}_{\text{grav}}$ are the radiation and gravitational force respectively. Looking at the right hand side of the equation, we can distinguish three possible forces that can drive an outflow: thermal pressure (∇P), magnetic ($(\nabla \times \mathbf{B}) \times \mathbf{B}$), and radiation forces ($\mathbf{a}_{\text{rad}}$).

1.4.1 Driving mechanisms

Radiation-driven winds

The Eddington limit derived in subsection 1.3.1 gives an approximation of the maximum luminosity a system can have before radiation pressure can drive material out of the gravitational pull of the BH. To successfully launch an outflow through radiation driving, we have two possibilities: either the mass accretion rate is high enough to overcome the Eddington limit, or the radiation opacity is significantly stronger than Thomson scattering (which we assumed to derive the Eddington limit).

In the first case, we have outflows known as super-Eddington winds (Eggum et al., 1988; Ohsuga et al., 2005), which play an important role in very luminous systems such as ultra-luminous X-ray sources (Mineshige et al., 2000). Nonetheless, many systems that exhibit outflows are below the Eddington limit, such as cataclysmic variables (CVs) (Warner, 2003), BAL QSOs (Gofford et al., 2015), and UFOs (Hagino et al., 2015).

As for the second case, we need to focus on how the radiation and matter couple depending on the chemical composition of the accreted material as well as the energy distribution of the emitted spectrum. AGN accretion discs peak at UV wavelengths (subsection 1.3.2), an energy range that is especially relevant given the high number of atomic transitions that take place in this band. Thus if the accretion flow is able to efficiently couple to the UV radiation, the radiation force is capable of driving a very powerful outflow. These winds are known as UV line-driven winds and are introduced in detail in chapter 2. Likewise, other energy bands

may couple very efficiently to the gas, as in the case of radiation pressure on dust (Rees et al., 1969; Fabian et al., 2006; Naddaf et al., 2021), which it can have a cross section up to 100 times larger than Thomson scattering. Dust-driven winds may play a crucial role on understanding the origin of the BLR (Czerny & Hryniewicz, 2011; Baskin & Laor, 2018).

Thermal winds

It is possible for an accretion disc in vertical hydrostatic equilibrium to lose mass through heating of the upper layers of the disc (Begelman et al., 1983). Thermal winds are especially relevant in X-ray binaries, since the X-ray irradiation by the inner parts of the disc of the outer parts can be very significant (Done et al., 2018; Tomaru et al., 2019). They are also relevant in the context of AGN, where they may play a role in explaining warm absorbers (Krolik & Kriss, 2001; Mizumoto et al., 2019), though additional forces from the pressure of dust may also be important here (Dorodnitsyn & Kallman, 2012; Dorodnitsyn et al., 2016).

Magnetic winds

Magnetic winds are winds powered by the energy and momentum removed from the accretion disc by a magnetic field (Blandford & Znajek, 1977; Fukumura et al., 2017). We already discussed in subsection 1.3.2 how magnetic fields can control the accretion process through the MRI, so it is possible that they are also responsible for powering outflows. Magnetic winds do not require radiation pressure and thus can be driven in low luminosity AGNs or in circumstances where the material is very ionised and other mechanisms such as line-driving would be inefficient (Konigl & Kartje, 1994). The coupling between the accretion disc and the wind could serve a two fold process: energy and momentum from the disc are transferred to the outflow so the outflow facilitates the transport of angular momentum so that mass can fall inwards (Cannizzo & Pudritz, 1988; Bogovalov & Tsinganos, 1999; Koide et al., 2002).

Chapter 2

UV line-driven winds

UV line-driven winds are outflows which are driven through radiation pressure on spectral lines. They were first studied in the context of hot stars (Castor et al. (1975), hereafter CAK), that emit most of their radiation in the UV energy range, where there is a high number of transition lines available in multiple elements such as Fe, N, C, O, etc. The Doppler shifting caused by the accelerating wind enables a big part of the radiation spectrum to be absorbed, preventing line self-shadowing and allowing the gas to absorb a big part of the radiation's momentum and energy.

In this chapter, we first introduce the concept of the force multiplier, which is a common approach to modelling the line force. We then discuss how this factor changes under the presence of ionising radiation, followed by a review of the current approaches to modelling UV line-driven winds in AGN. We conclude with some comments on observational constraints to line-driving.

2.1 The force multiplier

Consider a fully ionised plasma at a distance R from an object of mass M radiating with luminosity L. The force that a proton experiences in this plasma can be decomposed into a gravity component,

$$F_{\rm grav} = -\frac{GMm_p}{R^2}, \tag{2.1.1}$$

and a radiation pressure component (which is indirectly felt through pressure on the plasma electrons),

$$F_{\rm rad} = \frac{\sigma_{\rm T}}{4\pi R^2}\,\frac{L}{c}. \tag{2.1.2}$$

These forces balance when the luminosity is equal to the Eddington limit, as we described in subsection 1.3.1.

Let us consider now the case where the plasma is not fully ionised, so that bound-bound transitions become relevant. The line-centre cross section, neglecting stimulated emission, can be written as (Rybicki & Lightman, 1986)

$$\sigma_l = \frac{\pi e^2}{m_e\, c}\ f\ \frac{1}{\Delta\nu_D\sqrt{\pi}}, \tag{2.1.3}$$

where f is the oscillator strength, $\Delta\nu$ is the Doppler width defined by

$$\Delta\nu_D = \frac{\nu_0}{c}\sqrt{\frac{2kT}{m_p}}, \tag{2.1.4}$$

where ν_0 is the frequency of the line. Numerical substitution of the physical constants allows us to express the line opacity as

$$\sigma_l \simeq 2\times 10^{-13} f \left(\frac{E}{10\text{ eV}}\right)^{-1}\left(\frac{T}{10^4\text{ K}}\right)^{1/2}\ \text{cm}^2, \tag{2.1.5}$$

which is helpful since it is in terms of the values we would expect in AGN accretion discs and O-stars. Comparing it to just electron scattering, we find

$$\frac{\sigma_l}{\sigma_{\text{T}}} \simeq 3\times 10^{11} f \left(\frac{E}{10\text{ eV}}\right)^{-1}\left(\frac{T}{10^4\text{ K}}\right)^{1/2}, \tag{2.1.6}$$

showing that the line opacity is much higher than Thomson scattering (note that $f\sim 1$). It is worth noting, however, that this is the line opacity at the centre of an individual narrow line, so the overall opacity integrated overall all the energy range may not be as much higher than electron scattering.

Let us now consider the line absorption of photons in a moving gas, aligned with the radiation field for simplicity. A photon of frequency ν can be absorbed by the line transition if along its path it encounters ions with velocities such that the Doppler shift brings the photon frequency inside the line width (in the ion rest frame). The set of locations in the wind where this happens is called the line interaction region.

The geometrical width of the interaction region depends on the velocity gradient in the wind and the line profile. We define the Sobolev length l_{Sob} as the length over which the velocity of the wind changes by v_{th}, the thermal velocity of the gas,

$$l_{\text{Sob}} = v_{\text{th}}\left|\frac{\text{d}v}{\text{d}r}\right|^{-1}. \tag{2.1.7}$$

We thus expect that the line interaction region is of the order of the Sobolev length. We can

then define the Sobolev optical depth

$$\tau = n_l \, \sigma_l \, v_{\rm th} \left| \frac{{\rm d}v}{{\rm d}r} \right|^{-1}, \tag{2.1.8}$$

where n_l is the population density of ions at a state l. The Sobolev approximation (Sobolev, 1960) considers that the quantities n_l, $v_{\rm th}$, and ${\rm d}v/{\rm d}r$ are constant across the Sobolev length, which substantially facilitates computing the line force.

The radiative acceleration produced by a single line is then, approximately, (Lamers & Cassinelli, 1999)

$$\mathbf{a}_l \simeq \frac{F_\nu \, \Delta\nu}{c} \, \frac{1 - e^{-\tau}}{\tau} \, \frac{n_l \, \sigma_l}{\rho}, \tag{2.1.9}$$

where F_ν is the spectral flux and ρ is the density of the gas. For an optically thin line, $\tau \ll 1$, the expression reduces to

$$\mathbf{a}_l \simeq \frac{F_\nu \, \Delta\nu}{c} \, \frac{n_l \, \sigma_l}{\rho}, \tag{2.1.10}$$

and so the expression is independent of the velocity gradient. On the other hand, for an optically thick line, $\tau \gg 1$, we have

$$\mathbf{a}_l \simeq \frac{F_\nu \, \Delta\nu}{c} \, \frac{1}{\tau} \, \frac{n_l \, \sigma_l}{\rho} = \frac{F_\nu \, \Delta\nu}{c} \, \frac{1}{\rho v_{\rm th}} \left| \frac{{\rm d}v}{{\rm d}r} \right|, \tag{2.1.11}$$

which is independent of the number of absorbing particles as well as the line opacity and $v_{\rm th}$, since $\Delta\nu \propto v_{\rm th}$. This is expected as all the radiation is being absorbed, regardless of the number of available ions and the probability of interaction.

The total acceleration produced by an ensemble of lines is then $\mathbf{a}_{\rm rad} = \sum_l \mathbf{a}_l$. This calculation is usually complicated to perform, since it requires the computation of the degree of ionisation and excitation for a large number of energy levels of multiple different elements. Furthermore, for each possible transition from these levels one needs to calculate the Sobolev optical depth. Current estimates of the line force account for up to 4.5 million spectral lines (Abbott, 1982; Pauldrach et al., 1986; Shimada et al., 1994; Lattimer & Cranmer, 2021).

In order to be able to solve the gas equation of motion, Castor, Abbot and Klein (CAK) introduced a dimensionless optical depth parameter

$$t = \sigma_{\rm T} \, v_{\rm th} \, \rho \left| \frac{{\rm d}v}{{\rm d}r} \right|^{-1}, \tag{2.1.12}$$

where we note that it does not depend on the specific properties of the line but only on the wind hydrodynamic properties, as opposed to equation 2.1.8. This parametrisation allowed CAK to define the force multiplier

$$\mathcal{M} = k \, t^{-\alpha}, \tag{2.1.13}$$

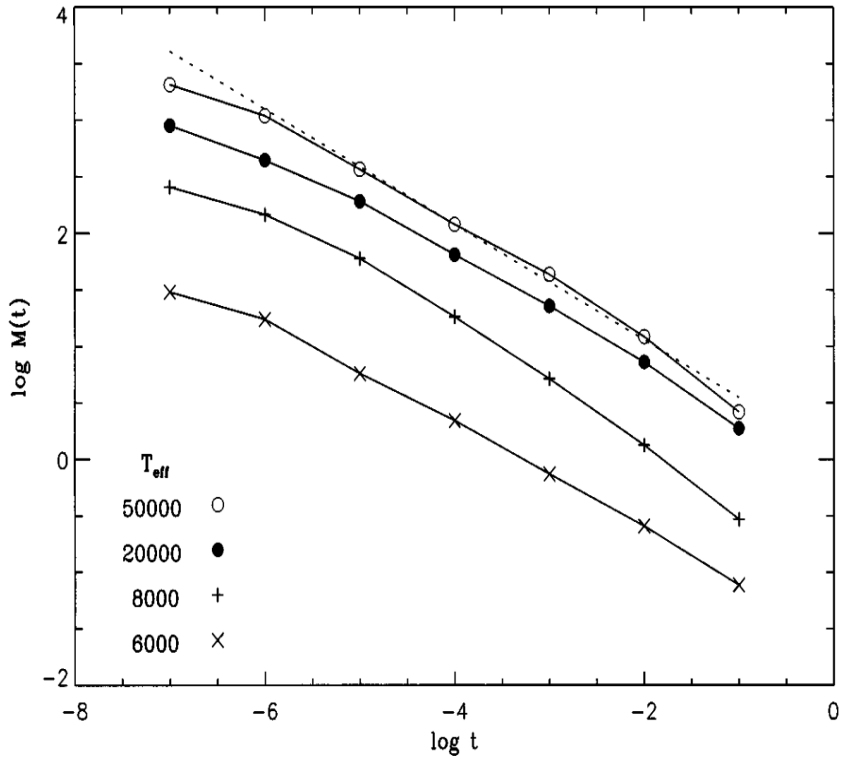

Figure 2.1: Force multiplier as a function of t for different gas temperatures, taken from Lamers & Cassinelli (1999), data from Abbott (1982) and Shimada et al. (1994) showing a power law fit.

where k and α are values that need to be fitted according to the line force calculation across all lines, such that

$$\mathbf{a}_l = \mathcal{M}\, \mathbf{a}_{\rm es}, \tag{2.1.14}$$

where $\mathbf{a}_{\rm es}$ is the radiation acceleration due to electron scattering only. In Figure 2.1 we show the fitted force multiplier for different O-star temperatures. The values of α are between 0.45 and 0.65, indicating that the radiative acceleration is due to a mixture of optically thick and optically thin lines. Equation 2.1.13 suggests that there is no upper limit for the force multiplier, as long as we can get $t \to 0$. This is unphysical and it can be shown that it indeed has an upper limit of the order of 10^3 (CAK). This maximum value puts a lower bound on the required luminosity of the system to drive a wind, indeed, if the luminosity of the system is $L < L_{\rm edd}/\mathcal{M}_{\rm max}$ where $\mathcal{M}_{\rm max}$ is the maximum value for the force multiplier, then the wind cannot escape the system by line-driving alone.

CAK are then able to solve the equations of motion for 1-dimensional line-driven wind in an O-star system, thus deriving its velocity profile and mass-loss rate. It is worth noting that the process of deriving the force multiplier and solving the wind momentum equations cannot

strictly be decoupled, since the radiation force depends on the wind's density. This means that a fully accurate simulation would require self-consistently solving the radiation transfer problem as well as integrating the hydrodynamic equations. Successful approaches have been made for the 1-dimensional solution (Noebauer & Sim, 2015), but for higher dimensions and more complicated geometries, the problem remains unsolved. Nonetheless, the CAK is able to reproduce observations well (Friend & Abbott, 1986; Pauldrach et al., 1986).

2.2 UV line-driven winds from accretion discs

Extending the CAK formalism to line-driven winds in accretion discs is not straightforward. In the spherical symmetry case, both the radiation and the gravitational force vary as $1/r^2$, while in a disc geometry, gravity $\propto z/r^3$ and the radiation field takes a complex form given the extended disc source (Icke, 1977). Furthermore, the presence of X-ray radiation in AGN imply that the material may be overionised, and the line transitions required to push the wind may not be available.

The extension of the theory of UV line-driven winds from hot stars to accretion discs was pioneered by Shlosman et al. (1985); Arav & Li (1994). Later on, the first radiation-hydrodynamic (RHD) simulations were done in the context of cataclysmic variables (CV) (Pereyra et al., 1997; Proga et al., 1998), with the subsequent calculations of resonance line profiles to compare with observations (Proga et al., 2002) which are consistent with the observed data albeit with a mass loss rate lower by a factor of 10 respect to observations.

To be able to accurately simulate AGN systems, we need to incorporate the effects of X-ray ionisation into the force multiplier calculation.

2.2.1 Force multiplier under X-ray radiation

The effect of X-ray ionisation on the force multiplier was studied in the context of XRB by Stevens & Kallman (1990) (hereafter SK90). They perform a similar procedure to parametrise the force multiplier as in equation 2.1.13, but with k now being a function of the ionisation parameter

$$\xi = \frac{L_{\mathrm{X}}}{nR^2}, \tag{2.2.1}$$

where L_{X} is the X-ray luminosity, n the number density of the gas, and R the distance to the X-ray source. In Figure 2.2 we show the dependence of the force multiplier on ξ for the UV and X-ray spectra of SK90. As expected, for high values of ξ the force multiplier is very

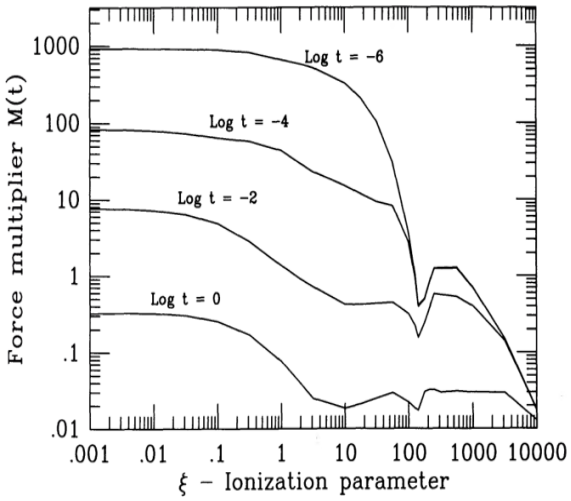

Figure 2.2: Force multiplier as a function of ξ for different values of t taken from SK90.

low, and would not be capable of driving a wind. For lower ionisation values, then the CAK is recovered. It is important to note, however, that the calculation of the force multiplier depends significantly on the SED of the source, and so the result obtained in SK90 are not generalisable to every system, and calculations are constantly done for different radiation sources (Ramirez-Velasquez et al., 2016; Dannen et al., 2019).

2.2.2 Simulations of AGN line-driven winds

Disc wind models for AGN were first discussed in depth in Murray et al. (1995). They present a dynamical model consisting of an AGN system with an outflow accelerated by UV line-driving. The innermost part of the wind acts as a shield against the central X-ray source, allowing the outer parts of the wind to be effectively accelerated with a high force multiplier. Other mechanisms have been proposed to keep the ionisation parameter value low, such as clumping (Hamann et al., 2013).

After the first RHD simulations of CVs, the method was extended to AGN, which involved including a central X-ray source that could ionise the wind (Proga et al., 2000; Proga & Kallman, 2004). The RHD simulations confirmed the scenario in which a UV line-driven wind can be successfully launched in the presence of X-rays due to the shielding by the inner wind. In Figure 2.4 we show a sample snapshot of such simulations, showing a wind flowing close to the equator. Further work studied the dependency of the wind properties on BH luminosity (Nomura et al., 2016; Nomura & Ohsuga, 2017), the effect of the disc mass loss to the wind on the radiation force (Dyda & Proga, 2018a; Nomura et al., 2020), and the dependence on metallicity (Nomura et al., 2021). Simultaneously, there has also been

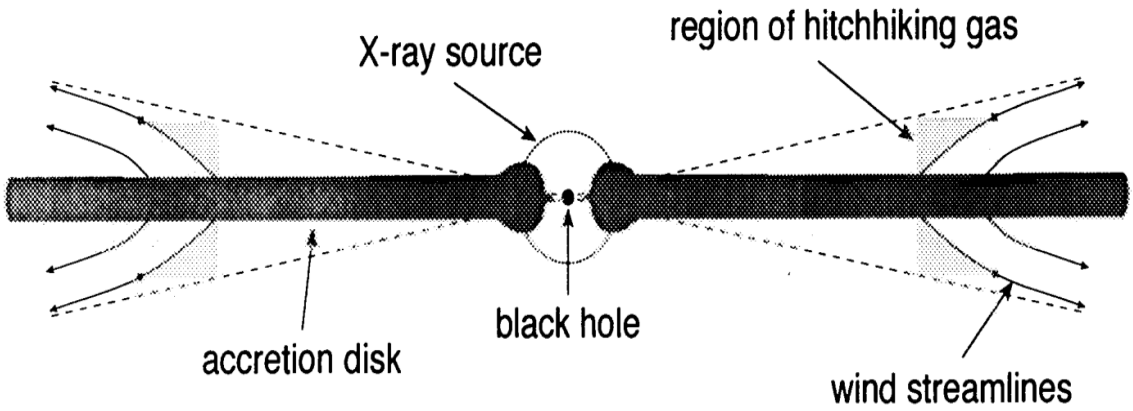

Figure 2.3: Schematic representation of an AGN disc wind taken from Murray et al. (1995).

research on the impact of the assumption of axisymmetry by performing three-dimensional simulations (Dyda & Proga, 2018b,c).

One of the limiting assumptions that is common in all RHD simulations of line-driven winds is the simplified treatment of the radiation transfer. More detailed analysis (Higginbottom et al., 2014) suggest that the shielding of the X-ray radiation may be inefficient and thus further work needs to be done in coupling hydrodynamic computer codes with two-dimensional radiation transfer models (e.g. Long & Knigge (2002); Odaka et al. (2011). In Figure 2.5, we show a comparison of the ionisation parameter obtained using the simplified radiation transfer model built in Proga & Kallman (2004) and the fully detailed radiation transfer code PYTHON (Long & Knigge, 2002). As we can see, the simplified model severely underestimates the ionisation at the outer parts of the wind, and thus overestimates the force multiplier in those regions. This is mostly caused by X-ray photons scattering through the wind, ionising gas that would be shielded in the absence of scattering. Even though the results presented in (Higginbottom et al., 2014) would suggest that UV line-driving may be more limited than previously thought, this is just a study on a particular snapshot of the RHD simulation, which was run with a simplified radiation model. An RHD simulation including a more accurate and realistic radiation transfer model would need to be run to estimate the real impact of X-ray scattering.

An alternative approach of simulating line-driven winds started with Risaliti & Elvis (2010), where gas particle trajectories are simulated ignoring the effects of hydrodynamics. Such approach is justified given that the motion of the wind is mostly determined by the radiation and centrifugal forces (Nomura et al., 2016) and that the wind velocities are mainly supersonic. The advantage of this method is that it is much more computationally efficient, thus allowing an easier exploration of the BH parameter space and understand under which

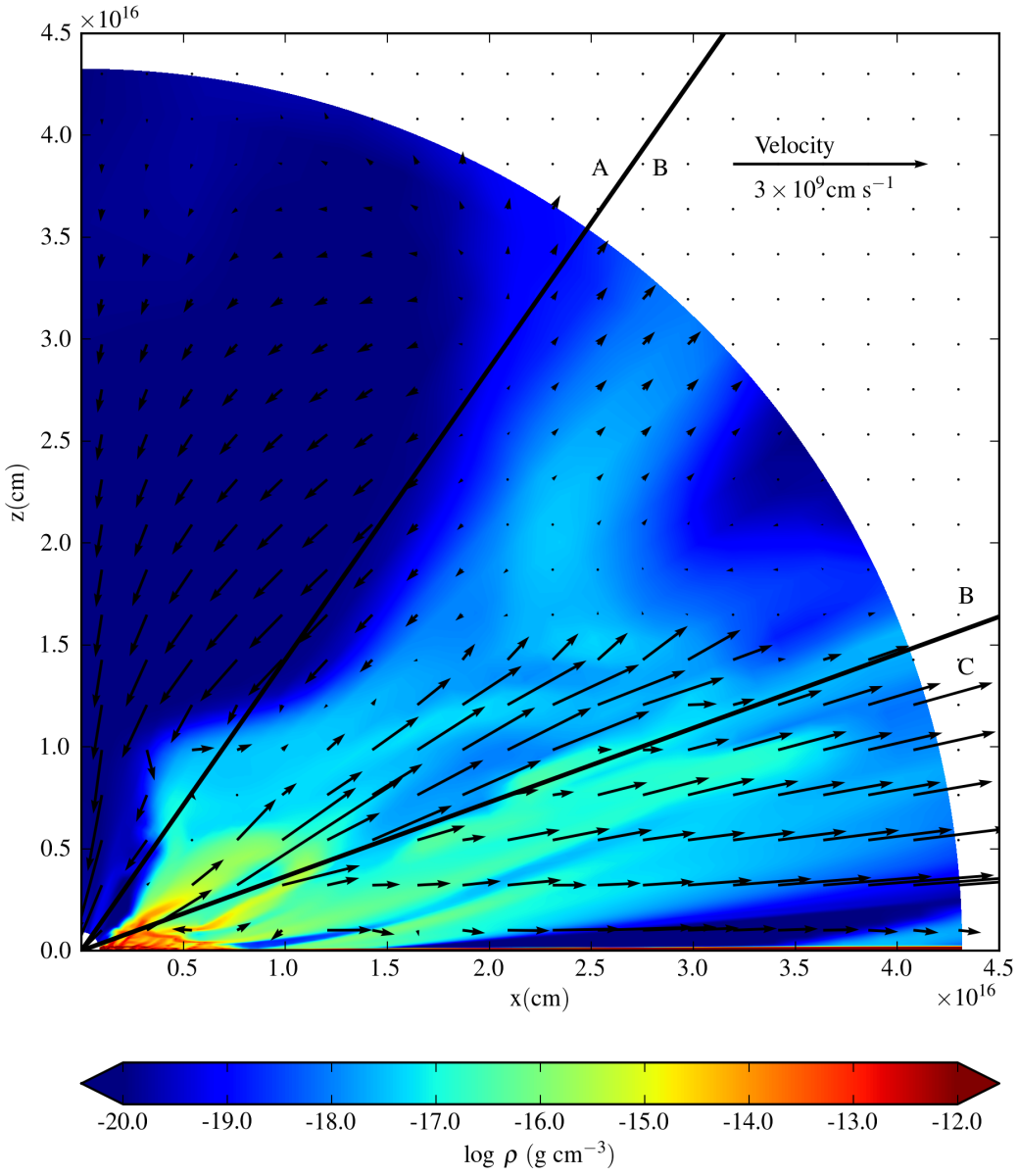

Figure 2.4: Snapshot of the UV line-driven wind simulated in (Proga & Kallman, 2004). Figure taken from Higginbottom et al. (2014).

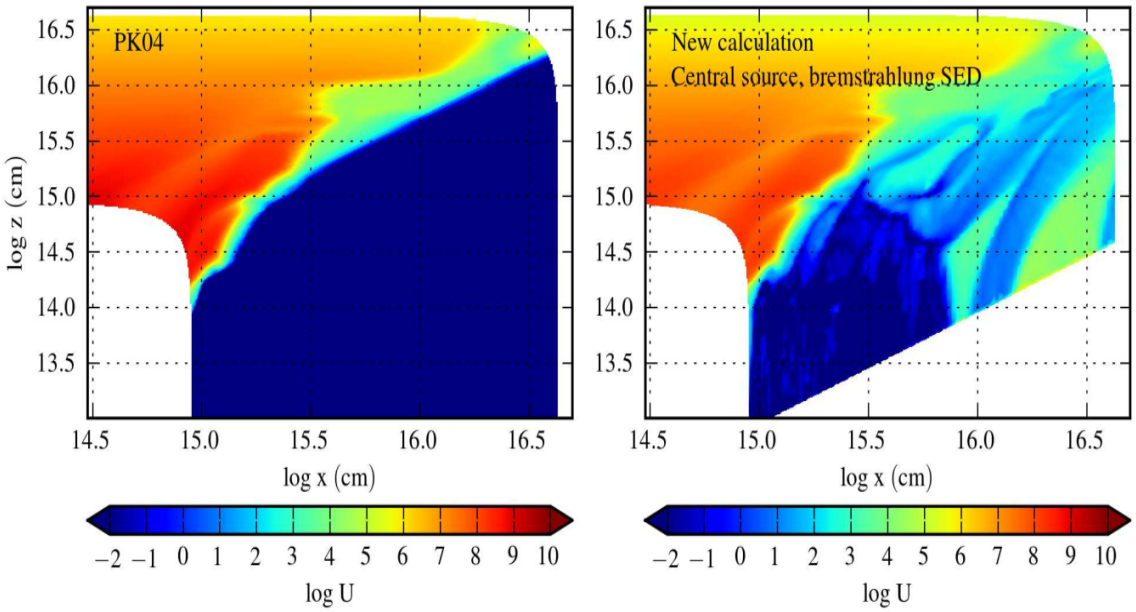

Figure 2.5: Ionisation parameter U related to our presented definition through $\log U = \log \xi - 1.75$ for a snapshot of the simulation Proga & Kallman (2004). The left panel corresponds to the calculation done in the RHD simulation, while the right panel is the result of a full radiation transfer calculation done with PYTHON (Long & Knigge, 2002). Figure taken from Higginbottom et al. (2014).

conditions line-driven winds can be launched from AGN accretion discs. This work builds on this approach. The method is explained in detail in chapter 3 and is further expanded with more realistic physics in chapter 4 such as relativistic corrections, self-consistent initial conditions for launching the wind from the surface of the accretion disc, and better radiation transfer. We finally use this new updated model to investigate which AGN systems should contain UV line-driven winds chapter 5.

2.2.3 Observational evidence for UV line-driving in AGN

Winds originating from accretion discs give a natural explanation to the distinction between BAL QSO and non-BAL QSO. Indeed, if the BAL features are explained through the presence of a wind, then observing it depends on the viewing angle and the coverage factor of the wind, as proposed by AGN unification models. We still lack, however, smoking gun observational evidence that allows us to distinguish between driving mechanisms for outflows.

One observational feature that would strongly support radiative driving is the presence of line-locking features in the spectra of BAL QSO. Consider two parcels of gas being accelerated by line-driving and that they are both aligned with respect to the radiation source. The radiation received by the outermost parcel is partly shielded by the innermost one. Under

certain circumstances, this shielding can cause both clouds to be locked together in velocity space (Foltz et al., 1987b; Braun & Milgrom, 1989). Unfortunately, observing this feature is not straightforward, since there are many other physical mechanisms that can contribute to a greater velocity dispersion such as turbulence or instabilities (Scargle, 1973), but current evidence suggests that many QSO systems with outflows contain line-locking features (Bowler et al., 2014).

The most well studied line-locking phenomenon is the so called Ly α ghost (Arav et al., 1995; Arav, 1996), which is a hump observed in the trough of the BAL. The profile of this feature reflects the profile of Ly α, thus giving it its name. In Figure 2.6, we show two QSO systems exhibiting this feature at the predicted velocity of -5900 km / s. This feature is also reproduced in numerical simulations (Chelouche & Netzer, 2003). Nonetheless, the number of observed QSO exhibiting this feature is small, with fewer than 50 observations to date (Arav, 1996; North et al., 2006; Cottis et al., 2010) and even within the sample, observations present many challenges to interpret (Cottis et al., 2010).

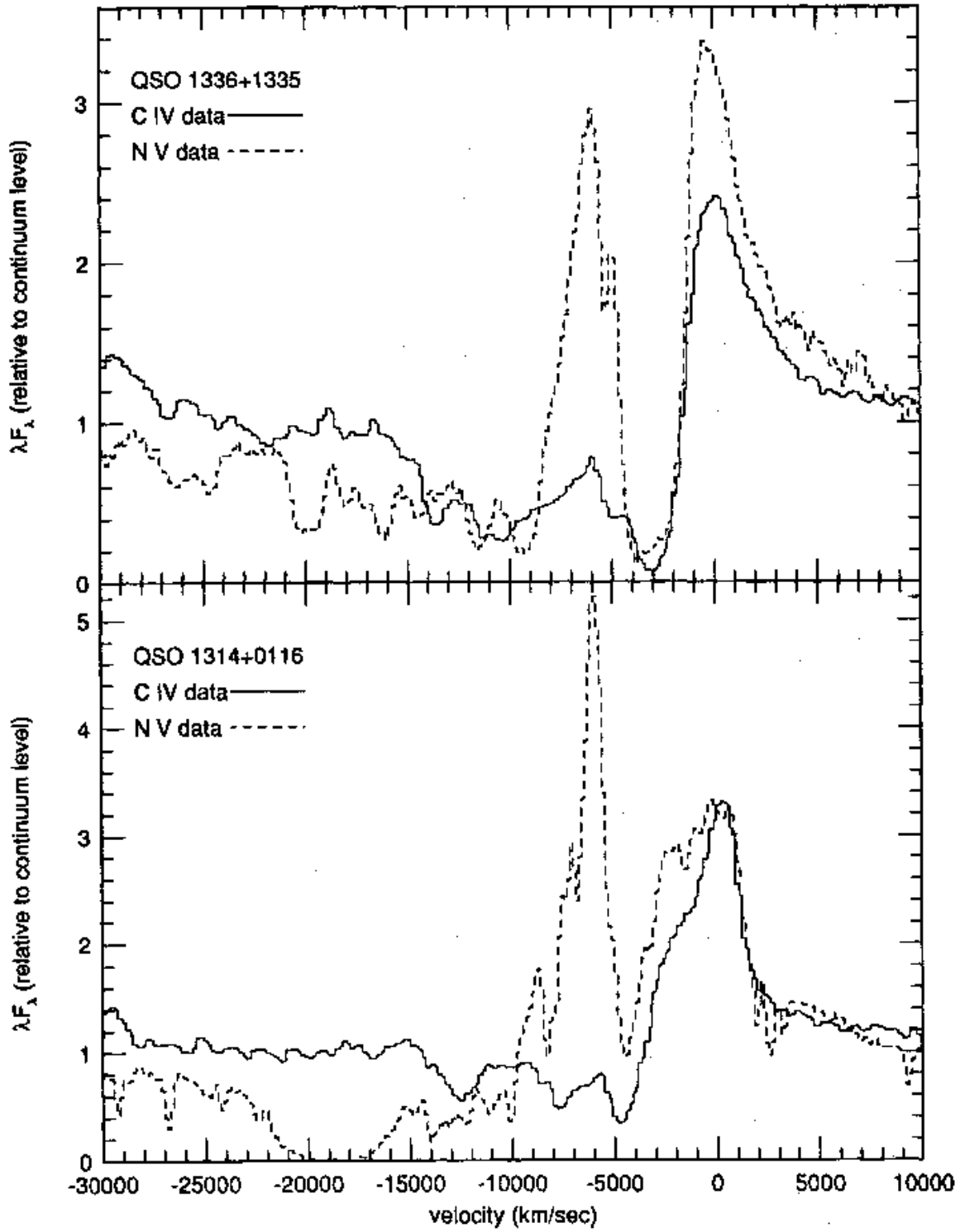

Figure 2.6: Two examples of the Lyα ghost phenomenon, taken from Arav (1996) . The spectral bump can be remarkably seen in both spectra at -5900 km / s.

Chapter 3

The Qwind model

3.1 Introduction

As we described in chapter 2, the physical principles of radiatively line-driven winds were extensively studied by CAK and Abbott (1982) in the context of O-type stars. Two decades later the same approach was extended to accretion discs around AGN (Murray et al., 1995), using the classical thin SS disc model. A few years later, the first results of hydrodynamical simulations of line-driven winds using the ZEUS2D code (Stone & Norman, 1992) were released (Proga et al., 2000; Proga & Kallman, 2004, hereafter P04), and continue to be extensively improved (Nomura et al., 2016, hereafter N16), and also Nomura & Ohsuga (2017); Nomura et al. (2020); Dyda & Proga (2018c,b).

However, full radiation hydrodynamic calculations are very computationally intensive. Another approach is to study only ballistic trajectories, i.e. neglect the gas pressure forces. This non-hydrodyamic approach was started by Risaliti & Elvis (2010), hereafter RE10, as the radiation force from efficient UV line driving can be much stronger than pressure forces. Their Qwind code calculated the ballistic trajectories of material from an accretion disc illuminated by both UV and X-ray flux. The neglect of hydrodynamics means that the code can be used to quickly explore the wind properties across a wide parameter space, showing where a wind can be successfully launched and accelerated to the escape velocity and beyond.

Here we revisit the Qwind code approach, porting it from C to Python, and improving it for better numerical stability and correcting some bugs. We show that this non-hydrodynamic approach does give similar results to a full hydrodynamic simulation. We illustrate how this can be used to build a predictive model of AGN wind feedback by showing the wind mass loss

rate and kinetic luminosity for a typical quasar. The new code, QWIND2, is now available as a public release on GitHub [1].

3.2 Methods

In this section we include for completeness the physical basis of the code and its approach to calculating trajectories of illuminated gas parcels (RE10). In subsection 3.2.1 we describe the geometrical setup of the system. The treatment of the X-ray and UV radiation field is explained in subsection 3.2.2, and we conclude by presenting the trajectory evolution algorithm in subsection 3.2.4.

3.2.1 Geometry setup

We use cylindrical coordinates (R, ϕ, z), with the BH and the X-ray emitting source considered as a point located at the centre of the grid, at $R = z = 0$. The disc is assumed to emit as a Novikov-Thorne (Novikov & Thorne, 1973) (hereafter NT) disc, but is assumed to be geometrically razor thin, placed in the plane $z = 0$, with its inner radius given by $R_{\rm isco}$ and outer radius at $R_{\rm out}$. We model the wind as a set of streamlines originating from the surface of the disc between radii $R_{\rm in} \geq R_{\rm isco}$ and $R_{\rm out}$, where the freedom to choose R_{in} allows wind production from the very inner disc to be suppressed by the unknown physical structure which gives rise to the X-ray emission.

The trajectory of a gas element belonging to a particular streamline is computed by solving its equation of motion given by $\mathbf{a} = \mathbf{a}_{\rm grav} + \mathbf{a}_{\rm rad}$, where $\mathbf{a}$ is the acceleration and $\mathbf{a}_{\rm grav}$ and $\mathbf{a}_{\rm rad}$ are the force per unit mass due to gravity and radiation pressure respectively, using a time-adaptive implicit differential equation system solver (subsection 3.2.4). The computation of the trajectory stops when the fluid element falls back to the disc or it reaches its terminal velocity, escaping the system. Since the disc is axisymmetric, it is enough to consider streamlines originating at the $\phi = 0$ disc slice.

3.2.2 Radiation field

The radiation field consists of two spectral components.

[1] https://www.github.com/arnauqb/qwind

The X-ray component

The central X-ray source is assumed to be point-like, isotropic, and is solely responsible for the ionisation structure of the disc's atmosphere. The X-ray luminosity, $L_{\rm X} = f_{\rm X}\, L_{\rm bol}$. The ionisation parameter is

$$\xi = \frac{4\pi F_{\rm X}}{n}, \tag{3.2.1}$$

where $F_{\rm X}$ is the ionising radiation flux, and n is the number density. The X-ray flux at the position (R, z) is computed as

$$F_{\rm X} = \frac{L_{\rm X}\ \exp\left(-\tau_{\rm X}\right)}{4\pi r^2}, \tag{3.2.2}$$

where $r = \sqrt{R^2 + z^2}$, and $\tau_{\rm X}$ is the X-ray optical depth, which is calculated from

$$\tau_{\rm X} = \int_{R_{\rm in}}^{r} n_0(r')\, \sigma_{\rm X}(\xi)\, {\rm d}r', \tag{3.2.3}$$

where $n_0(r)$ is the number density measured at the base of the wind, by projecting the distance r' to the disc (see subsection 3.2.3). This assumption overestimates both the UV and the X-ray optical depth far from the disc surface, but we present an improved algorithm in section 4.4. $\sigma_{\rm X}(\xi)$ is the cross-section to X-rays as a function of ionisation parameter, which we parametrise following the standard approximation from Proga et al. (2000),

$$\sigma_{\rm X}(\xi) = \begin{cases} 100\,\sigma_{\rm T} & \text{if } \xi < 10^5 \text{ erg cm s}^{-1}, \\ \sigma_{\rm T} & \text{if } \xi \geq 10^5 \text{ erg cm s}^{-1}, \end{cases} \tag{3.2.4}$$

where the step function increase in opacity below $\xi = 10^5$ erg cm s^{-1} very approximately accounts for the increase in opacity due to the bound electrons in the inner shells of metal ions, and $\sigma_{\rm T}$ is the Thomson cross section. This sharp transition in the opacity value can be interpreted as follows: lower ionisation levels imply a higher overall opacity, since bound-bound transitions become available, at the same time, the increase in opacity also brings an increase in the optical depth, further dropping the ionisation state of the gas. Hence, such a sharp transition may be physically motivated.

The ultraviolet component

The UV source is the accretion disc, emitting according to the NT model in an anisotropic way due to the disc geometry. The UV luminosity is $L_{\rm UV} = f_{\rm UV}\, L_{\rm bol}$. Currently the code makes the simplifying assumption that $f_{\rm UV}$ is constant as a function of radius. The emitted

UV radiated power per unit area by a disc patch located at $(R_d, \phi_d, 0)$ is

$$\mathcal{F} = f_{\rm UV} \frac{3GM\dot{M}}{8\pi R_d^3} f(R_d, R_{\rm isco}). \tag{3.2.5}$$

The SS equations as used by RE10 are non-relativistic, with $f(R_d, R_{\rm isco}) = [1-(R_{\rm isco}/R_d)^{1/2}]$ which leads to the standard Newtonian disc bolometric luminosity of $L_d = \frac{1}{12}\dot{M}c^2$ i.e. an efficiency of ≈ 0.08 for a Schwarzschild black hole, with $R_{\rm isco} = 6R_g$. We use instead the fully relativistic NT emissivity, where f is explicitly a function of black hole spin, a, and the efficiency is the correct value of $\eta(a=0) = 0.057$ for a Schwarzschild black hole. This is important, as the standard input parameter, $\dot{m} = L_{\rm bol}/L_{\rm Edd}$, is used to set $\dot{M}$ via $L_{\rm bol}/(\eta(a)c^2)$. The relativistic correction reduces the radiative power of the disc by up to 50% in the innermost disc annuli, compared to the Newtonian case.

Assuming that the radiative intensity (energy flux per solid angle) $I(R_d)$ is independent of the polar angle over the range $\theta \in [0, \pi/2]$, we can write

$$I(R_d) = \frac{\mathcal{F}}{\pi}, \tag{3.2.6}$$

thus the UV radiative flux from the disc patch as seen by a gas blob at a position $(R, 0, z)$ is

$$\mathrm{d}F = f_{\rm UV} \frac{I(R_d)}{\Delta^2} \cos\theta \; R_d \; \mathrm{d}R_d \mathrm{d}\phi_d, \tag{3.2.7}$$

where

$$\Delta = (R^2 + R_d^2 + z^2 - 2\,R\,R_d \cos\phi_d)^{1/2}. \tag{3.2.8}$$

(The flux received from an element of area $\mathrm{d}A = R_d \; \mathrm{d}R_d \mathrm{d}\phi_d$ at distance Δ seen at angle θ is $I\mathrm{d}\Omega$, where the solid angle subtended is $\mathrm{d}\Omega = (\mathrm{d}A\,\cos\theta)/\Delta^2$, and $\cos\theta = z/\Delta$.)

The average luminosity weighted distance is $\Delta \approx r$, so attenuation by electron scattering along all the UV lines of sight is approximately that along the line of sight to the centre i.e. analogously to equation 3.2.3, but only considering the electron scattering cross-section (see subsection 3.2.3). A more refined treatment that considers the full geometry of the disc is presented in section 4.4. The corresponding radiative acceleration due to electron scattering is then

$$\mathrm{d}\,\mathbf{a}_{\rm rad} = \frac{\sigma_{\rm T}}{c} \; \hat{\mathbf{n}} \; \mathrm{d}F \; \exp\left(-\tau_{\rm UV}\right), \tag{3.2.9}$$

with $\hat{\mathbf{n}}$ being the unit vector from the disc patch to the gas blob,

$$\hat{\mathbf{n}} = \frac{(R - R_d\cos\phi_d, -R_d\sin\phi_d, z)}{\Delta}. \tag{3.2.10}$$

Radiative line acceleration

The full cross-section for UV photons interacting with a moderately ionised gas is dominated by line absorption processes, implying potential boosts of up to 1000 times the radiation force caused solely by electron scattering. To compute this, we use the force multiplier M proposed by Stevens & Kallman (1990) hereafter SK90, which is a modified version of Castor et al. (1975) that includes the effects of X-ray ionisation. Ideally, one should recompute the force multiplier considering the full AGN spectral energy distribution (SED) (Dannen et al. (2019)), which is different than the B0 star spectrum considered in SK90, however this is out of the scope of this work. The full opacity is then $\sigma_{\rm total} = (1+M)\ \sigma_{\rm T}$, with the force multiplier M depending on the ionisation parameter, and on the effective optical depth parameter t (see section 2.1),

$$t = \sigma_{\rm T}\ n\ v_{\rm th}\ \left|\frac{{\rm d}v}{{\rm d}l}\right|^{-1}, \tag{3.2.11}$$

which takes into account the Doppler shifting resonant effects in the accelerating wind, and depends on the gas number density n, the gas thermal velocity $v_{\rm th}$ and the spatial velocity gradient along the light ray, ${\rm d}v/{\rm d}l$. In general, the spatial velocity gradient is a function of the velocity shear tensor and the direction of the incoming light ray at the current point. In this work we approximate the velocity gradient as the gradient along the gas element trajectory, allowing the force multiplier to be determined locally. A full velocity gradient treatment in the context of hydrodynamical simulations of line driven winds in CV systems has been studied in Dyda & Proga (2018c), who find that the inclusion of non-spherically symmetric terms results in the formation of clumps in the wind. Our non-hydrodynamical approach is insensitive to this kind of gas feature. It is convenient to rewrite the spatial velocity gradient as

$$\frac{{\rm d}v}{{\rm d}l} = \frac{{\rm d}v}{{\rm d}t}\ \frac{{\rm d}t}{{\rm d}l} = \frac{a_t}{v_t}, \tag{3.2.12}$$

where $a_t = \sqrt{a_R^2 + a_z^2}$, and $v_t = \sqrt{v_R^2 + v_z^2}$. This change of variables avoids numerical round-off errors as it avoids calculating small finite velocity differences. The force multiplier is parametrised as

$$M(t,\xi) = k(\xi)\, t^{-0.6} \left[\frac{(1 + t\ \eta_{\rm max}(\xi))^{0.4} - 1}{(t\ \eta_{\rm max}(\xi))^{0.4}}\right] \approx k(\xi)\, t^{-0.6}, \tag{3.2.13}$$

where the latter expression holds when $\eta_{\rm max}(\xi)\, t \gg 1$, which is the case for all cases of interest here. We extract the best fit values for k and $\eta_{\rm max}$ directly from Figure 5 of SK90, as opposed to using the usual analytic approximation given in equations 18 and 19 of SK90. The reason

we fit directly is because the analytical fitting underestimates the force multiplier in the range $10^2 \leq \xi \leq 10^4$, as we can see in Figure 3.1. In RE10 the analytical approximation was used, but we note that the step function change in X-ray opacity at $\xi = 10^5$ means that these intermediate ionisation states are not important in the current handling of radiation transfer, since the gas quickly shifts from being very ionised to being neutral, thus this change has negligible effect on the code results.

With all this in mind, the total differential radiative acceleration is

$$\mathrm{d}\,\mathbf{a}_{\mathrm{rad}} = \frac{\sigma_{\mathrm{T}}\,(1 + M(t,\xi))}{c}\,\hat{\mathbf{n}}\,\mathrm{d}F\,\exp\left(-\tau_{\mathrm{UV}}\right), \tag{3.2.14}$$

and the contribution from the whole disc to the radial and vertical radiation force is found by integrating,

$$\boldsymbol{a}^{\mathrm{es}}_{\mathrm{rad}}(R,z) = \mathcal{C}\,z \int\int \frac{f_{\mathrm{UV}} f_{\mathrm{NT}}}{R_{\mathrm{d}}^2\,\Delta^4} e^{-\tau_{\mathrm{UV}}} \begin{pmatrix} R - R_{\mathrm{d}}\cos\phi_{\mathrm{d}} \\ -R_{\mathrm{d}}\sin\phi_{\mathrm{d}} \\ z \end{pmatrix} \mathrm{d}R_{\mathrm{d}}\mathrm{d}\phi_{\mathrm{d}}. \tag{3.2.15}$$

The angular contribution is zero because of the cylindrical symmetry. Evaluating these integrals is not straightforward due to the presence of poles at $\Delta = 0$. The original QWIND code used a fixed grid spacing, but this is not very efficient, and led to inaccuracies with convergence of the integral (see section 3.6). Instead, we use the QUAD integration method implemented in the Scipy (Virtanen et al., 2020) Python package to compute them. section 3.4 shows that this converges correctly.

3.2.3 Optical depth calculation

The computation of the X-ray (and UV analogously) optical depth (equation 3.2.3) is not straightforward, as we need to take into account at which point the drop in the ionisation parameter boosts the X-ray opacity. Furthermore, the density is not constant along the light ray. Following the scheme illustrated in Figure 3.2, R_{X} denotes the radius at which the ionisation parameter drops below $10^5\,\mathrm{erg\,cm\,s^{-1}}$, R_{in} is the radius at which we start the first streamline, and thus the radius from which the shielding starts, and finally R_0 is the initial radius of the considered streamline. With this notation in mind, we approximate the optical depth by

$$\tau_{\mathrm{X}} = \sec\theta\,\sigma_{\mathrm{T}}\left[n_0\int_{R_{\mathrm{in}}}^{R_0}\kappa(R')\,\mathrm{d}R' + n(R)\int_{R_0}^{R}\kappa(R')\,\mathrm{d}R'\right], \tag{3.2.16}$$

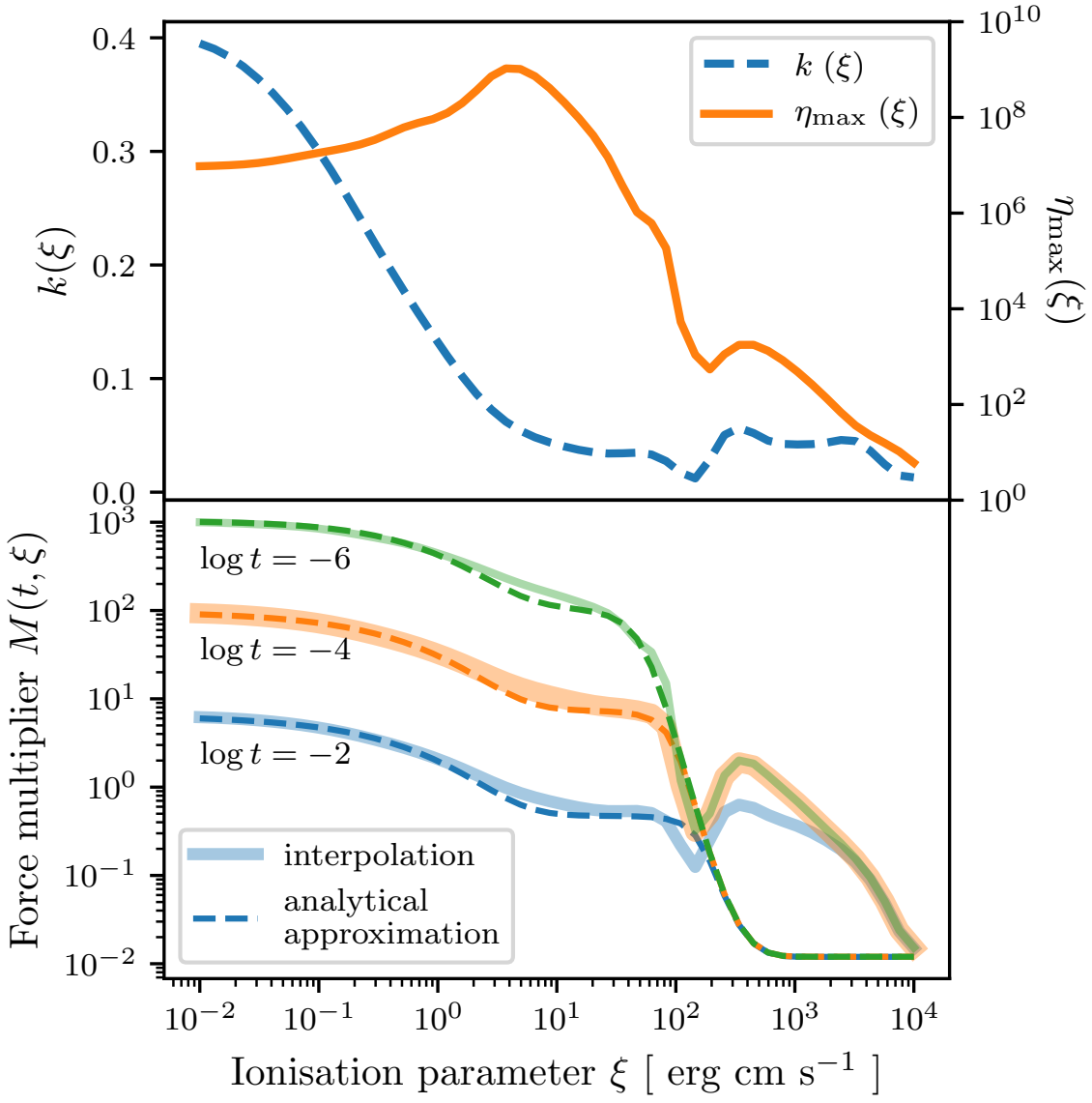

Figure 3.1: Top panel: Best fit values for the force multiplier parameters k and $\eta_{\max}$ as a function of ionisation parameter ξ, taken from SK90. Bottom panel: force multiplier as a function of the ionisation parameter and the effective optical depth, showing the discrepancy between the analytical approximation derived in SK90 and the direct interpolation at the range $10^2 \leq \xi \leq 10^4$. Note that, for the analytical approximation, M is independent of t for $\xi > 10^2$.

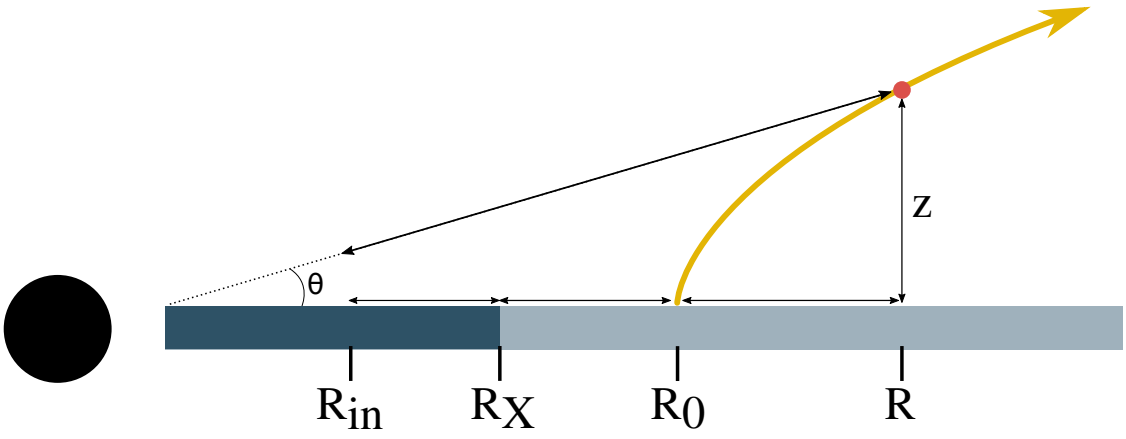

Figure 3.2: Schematic representation of the geometrical setup to compute the X-ray and UV optical depths. R_0 corresponds to the initial radius of the streamline being considered, and R_x is the radius at which $\xi = 10^5$ erg cm s^{-1}.

with

$$\kappa(R) = \begin{cases} 100 & \text{if } R > R_{\rm X}, \\ 1 & \text{if } R \leq R_{\rm X}. \end{cases} \tag{3.2.17}$$

The calculation for the UV optical depth is identical but setting the opacity boost factor to unity for all radii.

3.2.4 Trajectories of fluid elements

Gas trajectories are initialised at a height z_0, with launch velocity v_0. This can be different to the assumed thermal velocity as there could be additional mechanisms which help launch the wind from the disc, such as convection and/or magnetic fields, thus we keep this as a free parameter in the code so we can explore the effect of this. The equation of motion is $\mathbf{a}_{\rm tot} = \mathbf{a}_{\rm grav} + \mathbf{a}_{\rm rad}$, with

$$\mathbf{a}_{\rm grav}\,(R, z) = -\frac{GM_{\rm BH}}{r^2}\left(\frac{R}{r},\, 0,\, \frac{z}{r}\right). \tag{3.2.18}$$

In cylindrical coordinates, the system to solve is

$$\begin{aligned} \frac{\mathrm{d}R}{\mathrm{d}t} - v_R &= 0, \\ \frac{\mathrm{d}z}{\mathrm{d}t} - v_z &= 0, \\ \frac{\mathrm{d}v_R}{\mathrm{d}t} - a_R^{\mathrm{grav}} - a_R^{\mathrm{rad}} - \frac{\ell^2}{R^3} &= 0, \\ \frac{\mathrm{d}v_z}{\mathrm{d}t} - a_z^{\mathrm{grav}} - a_z^{\mathrm{rad}} &= 0, \end{aligned} \tag{3.2.19}$$

where ℓ is the specific angular momentum, which is conserved along a trajectory. The radiative acceleration depends on the total acceleration and the velocity at the evaluating point through the force multiplier (see equation 3.2.13 and equation 3.2.12), therefore, the system of differential equations cannot be written in a explicit form, and we need to solve the more general problem of having an implicit differential algebraic equation (DAE), $\mathbf{F}(t, \mathbf{x}, \dot{\mathbf{x}}) = 0$, where $\mathbf{F}$ is the LHS of equation 3.2.19, $\mathbf{x} = (R, z, v_R, v_z)$, and $\dot{\mathbf{x}} = (v_R, v_z, a_R, a_z)$. We use the IDA solver (Hindmarsh et al., 2005) implemented in the ASSIMULO simulation software package (Andersson et al., 2015), which includes the backward differentiation formula (BDF) and an adaptive step size to numerically integrate the DAE system. We choose a BDF of order 3, with a relative tolerance of 10^{-4}. In RE10, a second order Euler method was used without an adaptive time step. We do not find significant differences in the solutions found by both solvers, as RE10 used a very small step size, keeping the algorithm accurate. Nonetheless, the time step adaptiveness of our new approach reduces the required number of time steps by up to 4 orders of magnitude, making the algorithm substantially faster. For an assessment on the solver's convergence refer to section 3.4.

The gas density is calculated using the mass continuity equation, $\dot{M}_{\mathrm{line}}(t) = \dot{M}_{\mathrm{line}}(0)$. If the considered streamline has an initial width ΔL_0, assuming that the width changes proportionally to the distance from the origin, $\Delta L \propto r$, we can write

$$\dot{M}_0 = \rho_0\, v_0\, A_0 = \rho_0\, v_0\, 2\,\pi\, r_0\, \Delta L_0 = \rho\, v\, 2\,\pi\, r\, \Delta L = \dot{M}, \tag{3.2.20}$$

where $\rho_i = n(r_i)\, m_p$ with m_p being the proton mass. From here, it easily follows, using $\Delta L / \Delta L_0 = r / r_0$, that

$$n(r_i)\; v_i\; r_i^2 = n(r_0)\; v_0\; r_0^2, \tag{3.2.21}$$

which we use to update the density at each time step. The simulation stops either when the fluid element falls back to the disc, or when it leaves the grid ($r = 10^5\ R_g$).

3.3 The Qwind2 code

Algorithm 1: Fluid element trajectory initialisation and evolution

input: R_0, z_0, n_0, v_0
Read initial parameters;
Set initial angular velocity to Keplerian;
Initialise IDA solver;
while *(material not out of grid) or (material not fallen to the disc)* **do**
  IDA solver iteration. At each step, take current value of $\mathbf{x}$, and $\dot{\mathbf{x}}$, and do:
    Compute local velocity gradient $\frac{\mathrm{d}v}{\mathrm{d}l}$ using equation 3.2.12;
    Compute gas density using equation 3.2.21;
    Compute X-ray and UV optical depth see subsection 3.2.3;
    Compute ionisation parameter using equation 3.2.1 and equation 3.2.2;
    Compute force multiplier using equation 3.2.13;
    Compute radiative acceleration using the computed force multiplier and integrating equation 3.2.15;
    Compute gravitational acceleration using equation 3.2.18;
    Update fluid element position, velocity, and acceleration;
    Estimate solver error and update time step;
end
if *gas escaped* **then**
  Compute mass loss using mass flux conservation equation 3.6.2;
  Compute kinetic luminosity using equation 3.6.3;

In the code, we organise the different physical phenomena into three Python classes: *wind*, *radiation*, and *streamline*. The *wind* class is the main class of the code and it handles all the global properties of the accretion disc and launch region, such as accretion rate, atmospheric temperature/velocity/density etc. The *radiation* class implements all the radiative physics, such as the calculation of optical depths and the radiation force. Finally, the *streamline* class represents a single fluid element, and it contains the Assimulo's IDA solver that solves the fluid element equation of motion, evolving it until it falls back to the disc or it exceeds a distance of $r = 10^5\ R_g$. It takes about 10 seconds on average on a single CPU to calculate one fluid element trajectory, thus we are able to simulate an entire wind in a few minutes, depending on the number of streamlines wanted.

The system is initialised with the input parameters (see Table 3.1), and a set of fluid elements are launched and evolved between $R_{\rm in}$ and $R_{\rm out}$ following algorithm 1. As an illustrative example, we define our baseline model with the parameter values described in Table 3.1. These parameter values are the same as used in RE10, except for the black hole mass that we take to be $M = 10^8\ \mathrm{M}_\odot$, rather than $2 \times 10^8\ \mathrm{M}_\odot$, to be able to compare with the hydrodynamic simulations of P04 and N16. We also launch the wind from closer to the disc, at $z_0 = 1R_g$ rather than the default $z_0 = 5R_s = 10R_g$ of RE10. We do this to highlight the

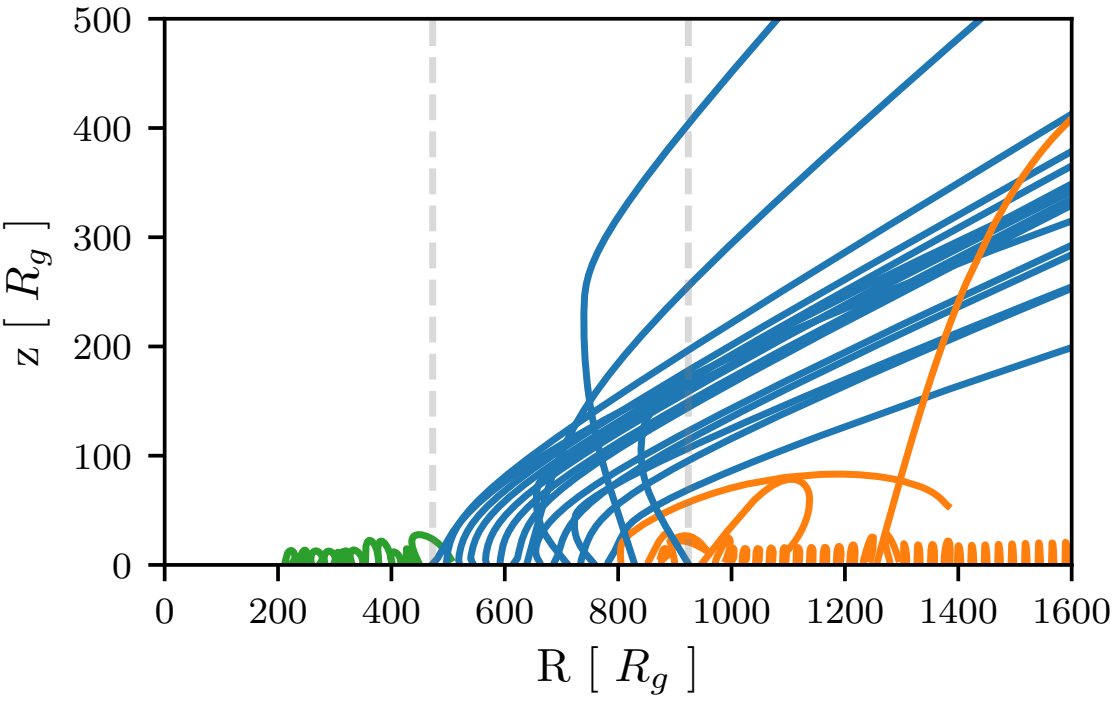

Figure 3.3: Results of a wind simulation, using the original QWIND code with the Newtonian disc flux equations from SS and a radiative efficiency of $\eta = 0.0313$. The wind temperature is set to $T = 2 \times 10^6$ K. The other parameters are set to the baseline parameter values (Table 3.1). The inner failed wind, escaping wind, and outer failed wind regions are coloured in green, blue, and orange respectively, and delimited by the grey dashed vertical lines.

Table 3.1: Qwind baseline parameters.

Parameter	Value
$R_{\rm in}$	200 R_g
$R_{\rm out}$	1600 R_g
$M_{\rm BH}$	10^8 $M_\odot$
$\dot{m}$	0.5
a	0
v_0	$10^7 {\rm cms}^{-1}$
n_0	2×10^8 cm^{-3}
z_0	1 R_g
T	2.5×10^4 K
$f_{\rm UV}$	0.85
$f_{\rm X}$	0.15

effect of the new integration routine.

To determine the number of streamlines N to simulate, we notice that the mass flow along a streamline with initial radius R_0 is

$$\dot{M}_{\rm wind} = 2\pi\ R_0\ \rho_0\ v_0\ \Delta L_0, \tag{3.3.1}$$

where $\Delta L_0 = (R_{\rm out} - R_{\rm in})/N$. The streamline with the highest mass flow is, thus, the one with the highest initial radius. We expect that the outermost escaping streamline will satisfy, at its base, $\tau \simeq R_0\ n_0\ \sigma_T \simeq 1$. We set N such that this streamline carries, at most, the 0.05% of the mass accretion rate. This implies that the chosen number of streamlines is independent of the initial density,

$$N = \frac{2\pi\ m_{\rm p}\ v_0\ (R_{\rm out} - R_{\rm in})}{5 \times 10^{-4}\ \dot{M}\ \sigma_T}. \tag{3.3.2}$$

For the parameter values of the baseline model (Table 3.1), we have $N \simeq 53$.

3.4 Integral and solver convergence

3.4.1 Integral convergence

Numerically solving the integration in equation 3.2.15 can be tricky because the points $\Delta = 0$ are singular. We use the QUAD integration method implemented in the SCIPY (Virtanen et al., 2020) Python package to compute them. We fix the absolute tolerance to 0, and the relative tolerance to 10^{-4}, which means the integral computation stops once it has reached a relative error of 10^{-4}. We have checked that the integrals converge correctly by evaluating the integration error over the whole grid, as can be seen in Figure 3.4. The relative errors

stays below 10^{-3}, which is 10 times more the requested tolerance but still a good enough relative error. We thus set a tolerance of 10^{-4} as the code's default.

3.4.2 Solver convergence

To assess the convergence of the IDA solver, we calculate the same gas trajectory multiple times changing the input relative tolerance of the solver, from 10^{-15} to 10^{-1}. We take the result with the lowest tolerance as the true value, and compute the errors of the computed quantities, R, z, v_R, v_z relative to our defined true values. As we can see in Figure 3.5, the relative error is well behaved and generally accomplishes the desired tolerance. After this assessment we fix the relative tolerance to 10^{-4} as the code's default.

3.5 The improvements of Qwind2

We first run the original QWIND code using the SS disc model with an efficiency $\eta = 0.0313$, and a wind temperature of $T = 2 \times 10^6 K$. The rest of the parameters are fixed to the default values shown in Table 3.1. We plot the resulting streamlines in Figure 3.3. The structure of the wind can be divided into three distinct regions: an inner failed wind (green), an escaping wind (blue), and an outer failed wind (orange), also delimited by the separating vertical dashed lines. The inner failed region corresponds to streamlines which have copious UV irradiation but where the material is too highly ionised for the radiation force to counter gravity. On the other hand, the outer failed wind comprises trajectories where the material has low enough ionisation for a large force multiplier, but the UV flux is not sufficient to provide enough radiative acceleration for the material to escape. Finally, the escaping wind region consists of streamlines where the material can escape as it is shielded from the full ionising flux by the failed wind in the inner region.

Effect of integration routine

Two of the blue escaping wind streamlines in Figure 3.3 (those originating from $\sim 900 R_g$) cross all the other escaping trajectories. We find that these crossing flowlines result from the old integration routine. The original code solved the integral in equation 3.2.15 using a non-adaptive method, which led to numerical errors in the radiative force at low heights. The first panel of Figure 3.6 shows the results using the same parameters and code with the new integration routine. The behaviour is now much smoother, not just in the escaping wind

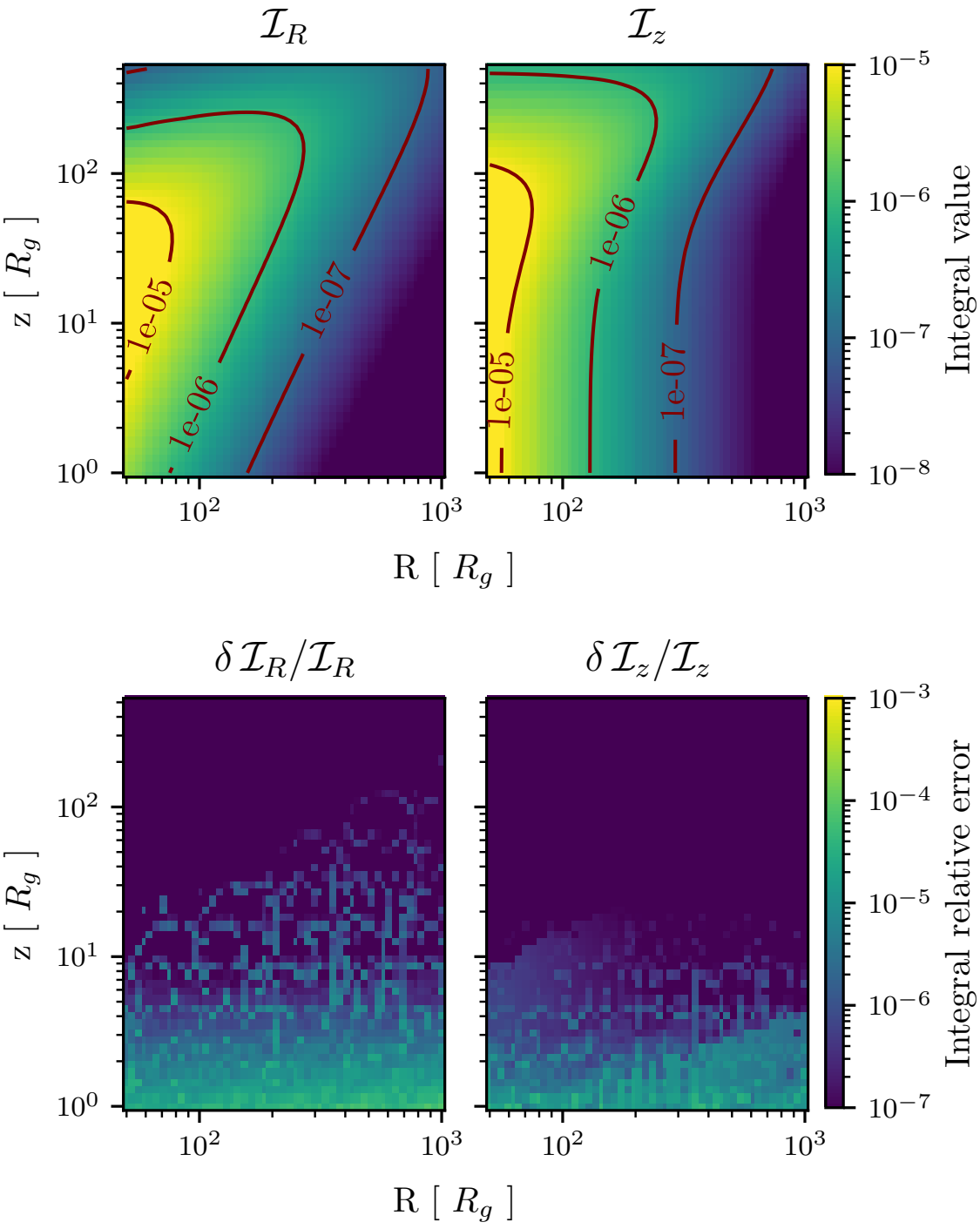

Figure 3.4: Top panels: Values for the radial and height integrals across the $R - z$ grid. Bottom panels: Relative error of the integrals. Note that the relative error stays well below 10^{-3} for the whole variable range, the low height points being the most difficult to compute.

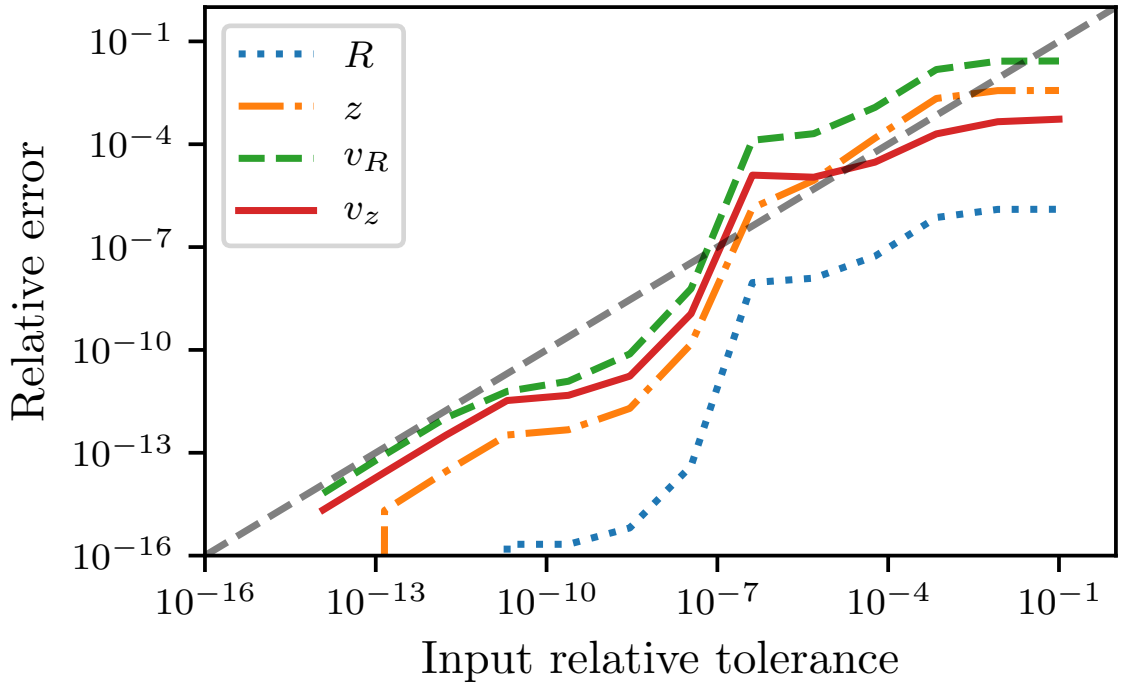

Figure 3.5: Measured relative error as a function of the input relative tolerance for the Assimulo IDA solver. The black dashed line represents equality.

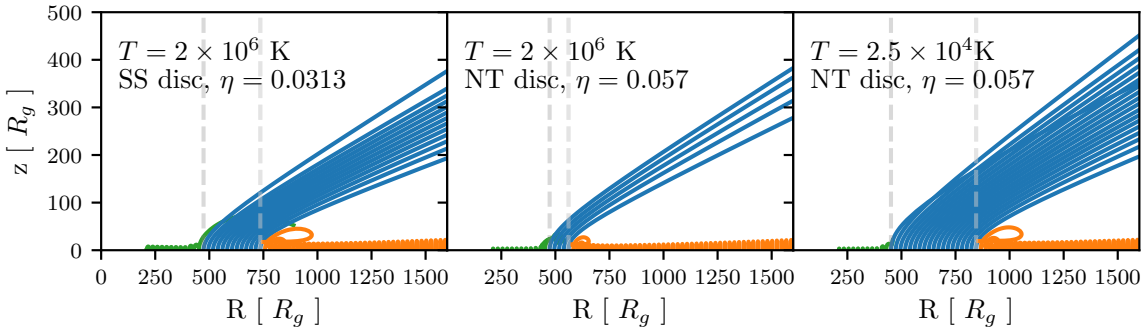

Figure 3.6: Three wind simulations performed with the updated Qwind code but different physical assumptions. All the non specified parameters are fixed to the baseline model (Table 3.1). The leftmost panel shows a simulation run assuming a non-relativistic Newtonian disc with an efficiency of $\eta = 0.0313$, and a temperature of $T = 2 \times 10^6 K$, while the middle one corresponds to the relativistic NT disc model with the correct efficiency $\eta = 0.057$. Finally, for the rightmost panel we use the relativistic disc model with the correct efficiency, and a temperature of $T = 2.5 \times 10^4$ K, consistent with the force multiplier derivation in SK90.

section but across all of the surface of the disc. The new Python integrator is much more robust, and has much better defined convergence (see section 3.4).

Efficiency and disc emissivity

The original code used the Newtonian disc flux equations from SS, but then converted from $\dot{m} = L_{\rm bol}/L_{\rm Edd}$ to $\dot{M}$ using an assumed efficiency, with default of $\eta = 0.0313$. This is low compared to that expected for the Newtonian SS disc accretion, where $\eta = 0.08$, and low even compared to a fully relativistic non-spinning black hole which has $\eta = 0.057$. For a fixed dimensionless mass accretion rate $\dot{m}$, the inferred $\dot{M} \propto 1/\eta$ as a larger mass accretion rate is required to make the same bolometric luminosity if the efficiency is smaller. Since $\dot{M}$ sets the local flux, this means that the local flux is a factor of ~ 2 smaller in the new QWIND2 code for a given $L_{\rm bol}$. The comparison between the first and second panels of Figure 3.6 shows that this reduction in the local UV flux means that fewer wind streamlines escape.

Wind thermal velocity

In the absence of an X-ray ionising source, the force multiplier is independent of the thermal velocity (see Abbott (1982) for a detailed discussion), this, however, does not mean one can freely choose a thermal velocity value at which to evaluate the effective optical depth t, since the values of the fit parameters in the analytical fit for $M(t)$ depend on the thermal velocity as well (see Table 2 in Abbott (1982)). If one includes an X-ray source as in SK90, then we expect the temperature of the gas to change depending on how much radiation a gas element is receiving from the X-ray source as well as from the UV source. At low values of the ionisation parameter, the results from Abbott (1982) hold, and thus it is justified to evaluate the force multiplier using an effective temperature of $T = 2.5 \times 10^4\ K$, corresponding to the temperature of the UV source used in SK90. Since the evaluation of the force multiplier is most important in regions of the flow where the gas is shielded from the X-ray radiation, we use this temperature value to compute the force multiplier throughout the code. In the N16 and P04 hydrodynamic simulations, the wind kinetic temperature is calculated by solving the energy equation that takes into account radiative cooling and heating, however, for the purpose of evaluating the force multiplier, a constant temperature of $T = 2.5 \times 10^4\ K$ is also assumed. In RE10, the force multiplier is evaluated setting $T = 2 \times 10^6$ K for the kinetic temperature. A higher thermal velocity increases the effective optical depth t, which in turn decreases the force multiplier given the same spatial velocity gradient and assuming

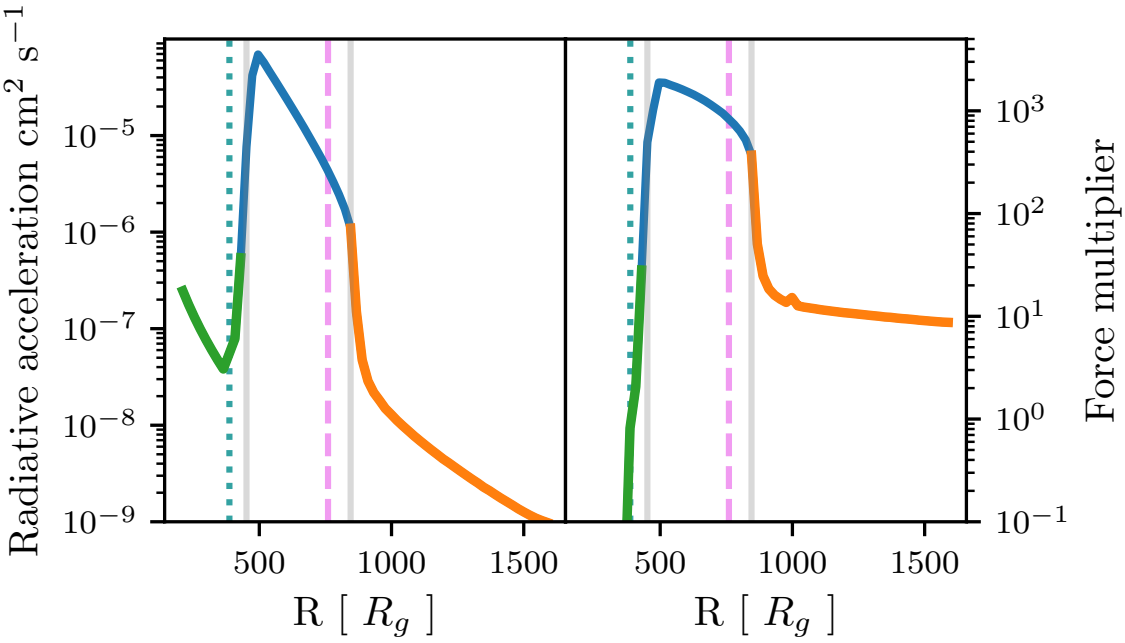

Figure 3.7: Maximum radiative force and force multiplier as a function of the initial radius of each streamline. Note that escaping lines, plotted in blue and delimited by the two vertical grey lines, require a balance between a sufficiently high force multiplier (thus low ionisation parameter), and high radiative force. Gas trajectories originating at the green coloured radii (left region delimited by the first vertical grey line) are too ionised, while the orange ones (rightmost region delimited by the second grey line) intercept too few UV photons. The radius at which the gas on the base of the wind becomes optically thick ($\tau = 1$) to X-Rays and UV is denoted by the dotted blue and the dashed purple lines respectively.

the same parametrisation for $k(\xi)$ and $\eta_{\max}(\xi)$, thus resulting on a narrower range of escaping streamlines. We can visualise the impact of this change by comparing the second and third panels of Figure 3.6. However, this apparent dependence of the force multiplier on thermal velocity is artificial, as explained above.

We define our baseline model as the one with the parameters shown in Table 3.1.

3.6 Baseline model in Qwind2

The new code is publicly available online in the author's GitHub account [2]. It is written purely in Python, making use of the Numba (Lam et al., 2015) JIT compiler to speed up the expensive integration calculations.

We now show more results from our new implementation of the Qwind code. The third

[2] https://github.com/arnauqb/qwind

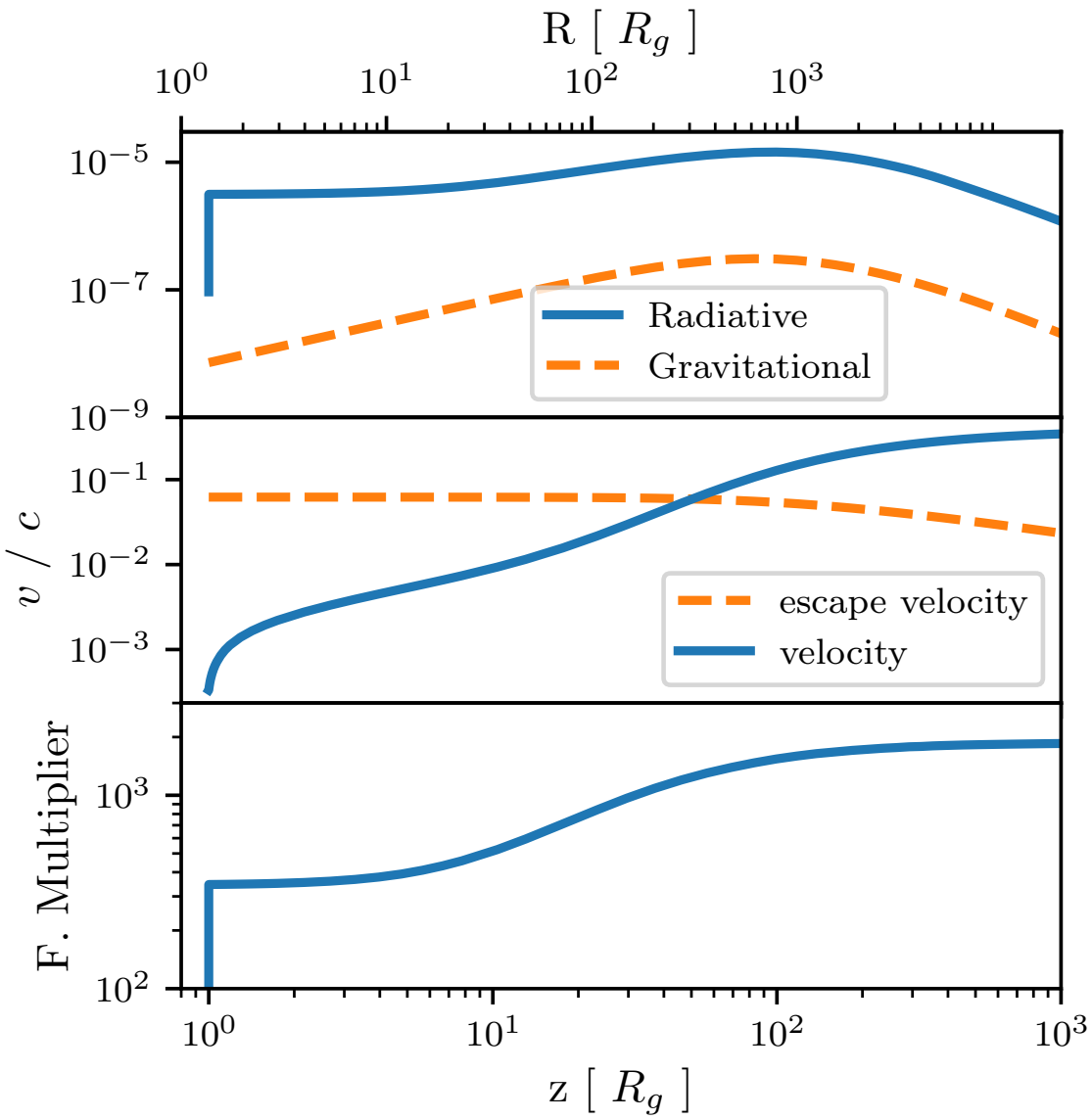

Figure 3.8: Streamline properties for an escaping gas trajectory. Top panel: Vertical radiative and gravitational acceleration as a function of height and radius. Middle panel: Streamline velocity as a function of radius and height. Bottom panel: Force multiplier as a function of radius and height.

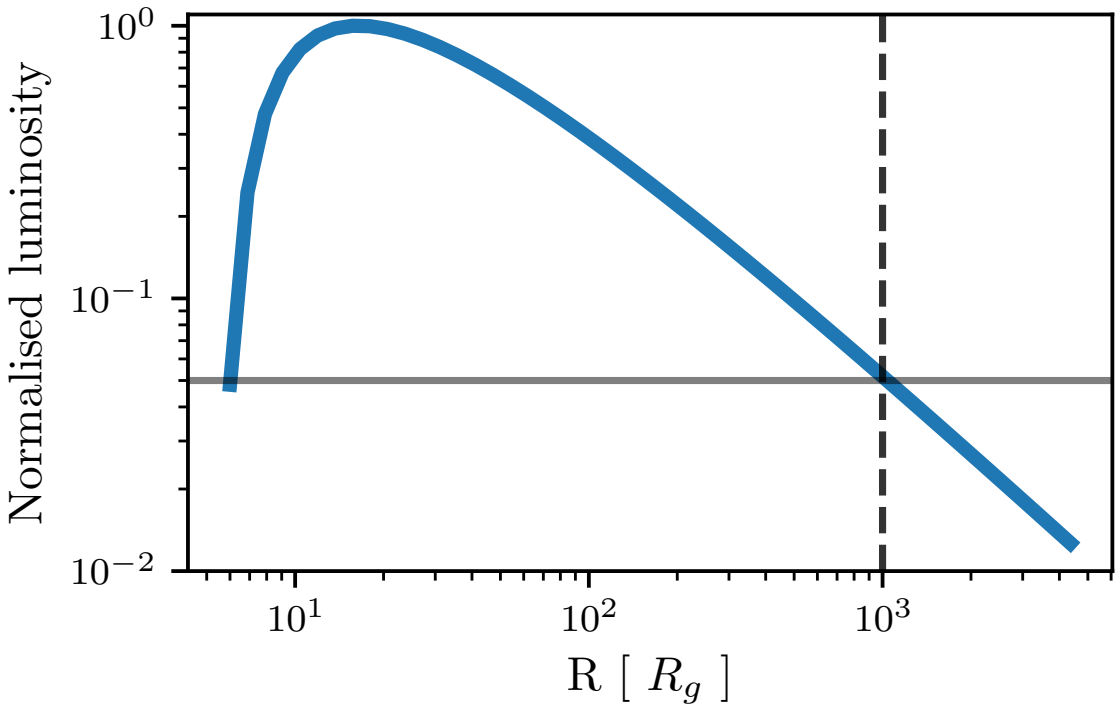

Figure 3.9: Disc annulus luminosity as a function of annulus radius, normalised to the luminosity of the brightest annulus. We have divided the radius range into 50 logarithmically spaced bins. The dashed black line corresponds to $R \simeq 1000\ R_g$, from where the outer annuli contribute less than 5% to the total luminosity compared to the brightest annulus at $R \simeq 16 R_g$. The sudden drop at $R \lesssim 16 R_g$ is due to the relativistic NT corrections to the SS disc.

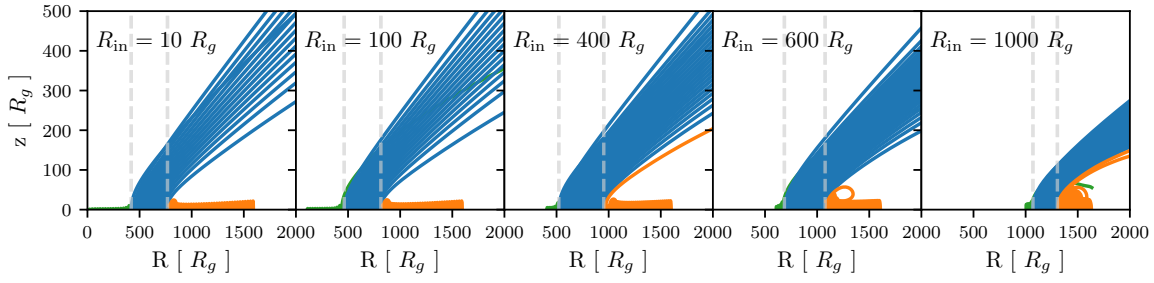

Figure 3.10: Different runs of the baseline model changing $R_{\rm in}$. The number of escaping streamlines is higher for larger values of $R_{\rm in}$, as the UV optical depth is lower while the shielding is still effective. Furthermore, outer escaping streamlines contribute more to the overall mass loss rate than the inner ones, since they represent larger disc annuli. The wind diminishes at $R_{\rm in} \gtrsim 1000\ R_g$, where the disc annuli do not emit enough UV radiation.

panel of Figure 3.6 shows that the radius range from which escaping lines can be originated is relatively narrow. This can be explained by looking at the radiative acceleration and the force multiplier for each streamline. We plot the maximum radiative acceleration and force multiplier for each of the streamlines as a function of their initial radius in the left panel of Figure 3.7. To effectively accelerate the wind, we need both a high UV flux, and a high force multiplier, which requires that the X-ray flux is sufficiently attenuated. Therefore, computing the UV and X-ray optical depths from the centre at the base of the wind can give us an estimate of the escaping region. Indeed, the cyan dotted line shows the radius at which the optical depth along the disc becomes unity for X-ray flux, while the purple dashed line shows the same for the UV flux. Clearly this defines the radii of the escaping streamlines, i.e. successful wind launching requires that the X-rays are attenuated but the UV is not.

We focus now on the physical properties of an individual escaping streamline. In Figure 3.8, we plot the vertical radiative acceleration, the velocity, and the force multiplier of the streamline as a function of its height and radius. We observe that most of the acceleration is achieved very rapidly and very close to the disc, consequently, the wind becomes supersonic shortly after leaving the disc, thus justifying our non-hydrodynamical approach. The sub-sonic part of the wind is encapsulated in the wind initial conditions, and the subsequent evolution is little affected by the gas internal forces. As we are focusing on a escaping streamline, the ionisation parameter is low, thus $\eta_{\max}$ will be very high (see top panel of Figure 3.1), enabling us to write $M(t) \propto t^{-0.6}$ (by taking the corresponding limit in equation 3.2.13). Additionally, since the motion of the gas element is mostly vertical at the beginning of the streamline, we have from the continuity equation (equation 3.2.21) $n \propto v_t^{-1}$, which combined with equation 3.2.12 gives

$$M(t) \propto t^{-0.6} \propto \left(\frac{a_t}{n v_t}\right)^{0.6} \simeq a_t^{0.6}. \tag{3.6.1}$$

Therefore, as the gas accelerates, the force multiplier increases as well, creating a resonant process that allows the force multiplier to reach values of a few hundred, accelerating the wind to velocities of $v \sim (0.1 - 0.2)\ c$. At around $z = 50\ R_g$, the gas element reaches the escape velocity at the corresponding radius, and it will then escape regardless of its future ionisation state.

We use mass conservation to calculate the total wind mass loss rate by summing the initial

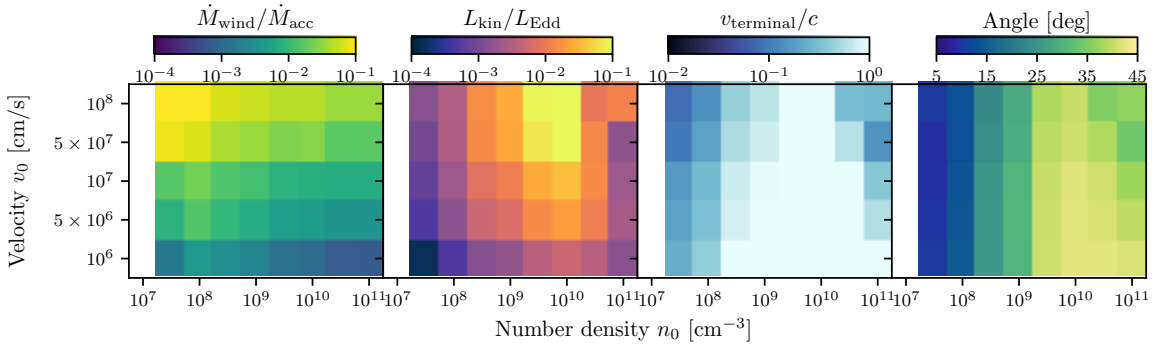

Figure 3.11: Results of different wind simulations varying the initial density n_0, and the initial velocity v_0. The rest of the parameters are fixed to the baseline model values (Table 3.1), except for $R_{\rm in} = 60\ R_g$, and $f_x = 0.1$. The first panel shows the mass loss rate normalised to the mass accretion rate, and the second panel shows the wind kinetic luminosity normalised to the Eddington luminosity. Finally the third and fourth panels show the terminal velocity and angle of the fastest streamline in the wind.

mass flux of the escaping trajectories,

$$\begin{aligned} \dot{M}_{\rm wind} &= \sum_{i \in \left\{ \substack{\text{escaping} \\ \text{trajectories}} \right\}} \dot{M}^{(i)}_{\rm wind} \\ &= \sum_{i \in \left\{ \substack{\text{escaping} \\ \text{trajectories}} \right\}} \rho_{i,0}\ v_{\rm i,0}\ 2\ \pi\ R_{i,0}\ \delta R_i, \end{aligned} \tag{3.6.2}$$

where $\delta\, R_{i,0} = R_{i+1,0} - R_i$. For the baseline model we obtain $\dot{M}_{\rm wind} = 3.01 \times 10^{24}$ g s^{-1} $= 0.05\, {\rm M}_\odot$ yr^{-1}, which equates to 2.5% of the black hole mass accretion rate. We can also compute the kinetic luminosity of the wind,

$$L_{\rm kin} = \frac{1}{2}\ \dot{M}_{\rm wind}\ v^2_{\rm wind}\,, \tag{3.6.3}$$

where $v_{\rm wind}$ is the wind terminal velocity, which we take as the velocity at the border of our grid, making sure that it has converged to the final value. The wind reaches a kinetic luminosity of $L_{\rm kin} = 7.83 \times 10^{43}$ erg/s, which equates to 0.62% of the Eddington luminosity of the system. Both these results depend on the choice of the initial conditions for the wind. In the next section, we scan the parameter range to understand under which parameter values a wind successfully escapes the disc, and how powerful it can be.

3.6.1 Dependence on launch parameters: $R_{\rm in}$, n_0, v_0

We consider variations around the baseline model (Table 3.1). We fix the black hole mass and accretion rate to their default values, and vary the initial launching radius $R_{\rm in}$, the initial

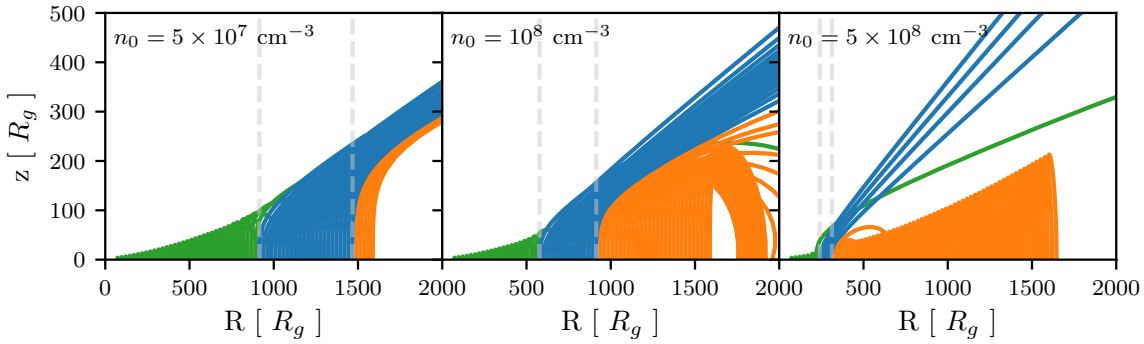

Figure 3.12: Three wind simulations from the parameter range scan shown in Figure 3.11. The initial velocity is fixed to $v_0 = 10^8$ cm/s, while the initial density is varied in the range $n_0 \in (5 \times 10^7,\ 10^8,\ 5 \times 10^8)$ cm^{-3}. Higher density values shift the escaping region to smaller radii, thus reducing the effective disc surface that produces an escaping wind. Furthermore, the increase in UV shielding narrows the range of escaping streamlines. Note that a high number of streamlines was used to produce Figure 3.11, according to the rule in equation 3.3.2, but we plot only a fraction of them for clarity.

density n_0, and the initial velocity v_0. We can make some physical arguments to guide our exploration of the parameter space:

1. The initial radius $R_{\rm in}$ at which we start launching gas elements can be constrained by considering the physical scale of the UV emitting region of the disc. In Figure 3.9, we plot the luminosity of each disc annulus normalised to the luminosity of the brightest annulus, using 50 logarithmically spaced radial bins. We observe that radii larger than $\gtrsim 1000\ R_g$ contribute less than 5% of the luminosity of the brightest annulus. On the other hand, the effective temperature of the disc drops very quickly below $R \simeq 16\ R_g$ due to the NT relativistic corrections.We thus consider that the initial launching radius can vary from 10 R_g to 1000 R_g.

   In Figure 3.10, we plot the results of changing $R_{\rm in}$ in the baseline model. Increasing the radius at which we start launching gas elements shifts the location of the wind towards higher radii, thus increasing the overall mass loss rate since outer streamlines represent a bigger disc surface (see equation 3.6.2). For very large initial radii, $R_{\rm in} \geq 1000\ R_g$, the wind severely diminishes as the UV flux is too low.

   To explore the remaining parameters, we fix $R_{\rm in} = 60\ R_g$, and $f_x = 0.1$. The reason for this is that we want to compare our results with the hydrodynamic simulations of P04 and N16, which used these parameter values.

2. The initial density n_0 of the gas elements needs to be high enough to shield the outer gas from the X-Ray radiation, so we need $\tau_{\rm X} > 1$ at most a few hundred R_g away from

the centre (further away the UV flux would be too weak to push the wind). Therefore as a lower limit,

$$\tau_{\rm X} = \int_{R_{\rm in}}^{100\ R_g} \sigma_x\, n_0\, {\rm d}r' < \int_0^{100\ R_g} 100\, \sigma_{\rm T}\, n_0\, {\rm d}r' \simeq 10^{-7} \left(\frac{n_0}{\rm cm^{-3}}\right), \tag{3.6.4}$$

which implies a minimum shielding density of $n_0 \simeq 10^7$ cm^{-3}. On the other hand, if the density is too high the gas is also shielded from the UV flux coming from the disc. Even though our treatment of the UV optical depth assumes that the UV source is a central point source (see subsection 3.2.3), let us consider now, as an optimistic case for the wind that the optical depth is computed from the disc patch located just below the wind. In that case, we need $\tau_{\rm UV} < 1$ at a minimum distance of $r \simeq 1\ R_g$,

$$\tau_{\rm UV} = \int_0^{1R_g} \sigma_T\, n_0\, {\rm d}r' \simeq 10^{-11} \left(\frac{n_0}{\rm cm^{-3}}\right), \tag{3.6.5}$$

so that the maximum allowed value is $n_0 \simeq 10^{11}$ cm^{-3}. Thus, we vary the initial density from 10^7 cm^{-3} to 10^{11} cm^{-3}.

3. Finally, we estimate the parameter range of the initial velocity v_0 by considering the isothermal sound speed at the surface of the disc. The disc's effective temperature at a distance of a few hundred R_g from the centre computed with the NT disc model is $\simeq 10^6$ cm/s, so we vary the initial velocity from 10^6 cm/s to 10^8 cm/s to account for plausible boosts in velocity due to the launching mechanism. The total number of streamlines is adjusted to ensure enough resolution (see equation 3.3.2).

Figure 3.11 show the resulting scan over the $n_0 - v_0$ parameter space. These results confirm the physical intuition we described at the beginning of this section; initial density values lower than $\simeq 5 \times 10^7$ cm^{-3} do not provide enough shielding against the X-ray radiation, while values higher than $\simeq 10^{10}$ cm^{-3} shield the UV radiation as well, and produce a slower wind. Furthermore, lower initial velocities result into higher final velocities, as the gas parcels spend more time in the acceleration region, and are thus also launched at a higher angle with respect to the disc. The parameter combination that yields the highest wind mass loss rate is $n_0 = 5 \times 10^7$ cm^{-3} and $v_0 = 10^8$ cm/s, which predicts a mass loss rate of 0.3 M$_\odot$/yr, equal to $\simeq 17\%$ of the mass accretion rate. The reason why lower initial densities lead generally to higher mass loss rates can be visualised in Figure 3.12. Higher initial densities shift the wind launching region to the inner parts of the accretion disc, since they are able to shield the X-Ray more efficiently but the gas also becomes optically thick to UV radiation rapidly. On the other hand, for low values of the initial density, the gas becomes optically thick to X-Rays

on the outer parts of the disc and the low UV attenuation implies that the range of escaping streamlines is wider. Additionally, outer radii represent annuli with bigger areas so the mass loss rate is significantly larger (see equation 3.6.2). The parameter combination $n_0 = 10^{10}$ cm^{-3} and $v_0 = 10^8$ cm/s yields the highest kinetic luminosity value, however, a few of the escaping streamlines have non-physical superluminal velocities. The parameter combination that generates the physical wind with the highest kinetic luminosity is $n_0 = 5 \times 10^9$ cm^{-3} and $v_0 = 10^8$ cm/s with $L_{\rm kin} \simeq 9\% L_{\rm Edd}$. Following Hopkins & Elvis (2010), this kinetic energy would be powerful enough to provide an efficient mechanism of AGN feedback, as it is larger than 0.5% of the bolometric luminosity. It is also worth noting that the angle that the wind forms with respect to the disc is proportional to the initial density. This can be easily understood, since, as we discussed before, higher initial densities shift the radii of the escaping streamlines inwards, from where most of the UV radiation flux originates. The wind originating from the inner regions of the disc has therefore a higher vertical acceleration, making the escaping angle higher compared to the wind in the outer regions.

3.7 Comparison with hydrodynamic simulations

A proper comparison with the hydrodynamic simulations of N16 and P04 is not straightforward to do, as there is not a direct correspondence of our free parameters with their boundary conditions, and some of the underlying physical assumptions are different (for instance, the treatment of the UV continuum opacity). Nonetheless, with P04 as reference, we have fixed so far $R_{\rm in} = 60\, R_g$ to match their starting grid radius, and $f_x = 0.1$, as they assume.

Another physical assumption we need to change to compare with P04 is the treatment of the radiative transfer. In P04, the UV radiation field is not attenuated throughout the wind, although line self-shielding is taken into account by the effective optical depth parameter t. Furthermore, the X-ray radiation is considered to only be attenuated by electron scattering processes, without the opacity boost at $\xi \leq 10^5$ erg cm s^{-1}. We thus set $\tau_{\rm UV} = 0$, and $\sigma_x = \sigma_{\rm T}$. Finally, we assume that the initial velocity is $v_0 = 2 \times 10^6$ cm /s which is just supersonic at $T = 2.5 \times 10^4$ K, and we fix $n_0 = 2.5 \times 10^9$ cm^{-3}, which gives $\tau_X = 1$ at $r = 100\, R_g$. The result of this simulation is shown on the top panel Figure 3.13. We notice that not attenuating the UV continuum has a dramatic effect on the wind, allowing much more gas to escape as one would expect. Indeed, the bottom panel of Figure 3.13 shows the same simulation but with the standard UV and X-ray continuum opacities used in QWIND. Running the simulation with the normal UV opacity but just electron scattering for the X-ray

cross section results in no wind being produced. For the unobscured simulation that mimics P04, we obtain a wind mass loss rate of $0.3\,\mathrm{M}_\odot\,/\,\mathrm{yr}$, which is in good agreement with the results quoted in P04 ($\dot{M}_{\mathrm{wind}} \sim (0.16 - 0.3)\,\mathrm{M}_\odot\,/\,\mathrm{yr}$). The wind has a kinematic luminosity of $L_{\mathrm{kin}} = 0.7\%$ at the grid boundary, and a terminal velocity ranging $(0.016 - 0.18)$ c, again comparable to the range $(0.006 - 0.06)$ c found in P04. Finally, the wind in P04 escapes the disc approximately at an angle between (4-21)°, while in our case it flows at an angle in the range (3 - 14)°.

3.8 Limitations of Qwind2

We have presented an updated version of the Qwind code (Qwind2), aimed at modelling the acceleration phase of UV line-driven winds in AGNs. The consistency of our approach with other more sophisticated simulations shows that the non-hydrodynamical treatment is well justified, and that our model has the potential to mimic the results of more expensive hydrodynamical simulations.

The main free parameters of the model are the initial density and velocity of each streamline, and the inner disc radius from which the fluid elements are first launched. Nomura et al. (2013) calibrate the initial wind mass loss using the relation from CAK that links the wind mass loss from O-stars to their gravity and Eddington ratio. However, it is not clear whether this relation holds for accretion discs, where the geometry and the radiation field and sources are quite different (Laor & Davis, 2014). In the next chapter, we present a consistent physical model that allows us to self-consistently compute the initial conditions of the wind.

Another point that needs to be improved is the treatment of the radiation field. The presented method to calculate the optical depth (subsection 3.2.3) is too simplistic, since it is not consistent with the density structure of the wind. Furthermore, we have not considered the relativistic correction to the radiation field seen by wind, which is particularly important given that we have shown that the wind can easily achieve high velocities. Both these points are also addressed in the following chapter.

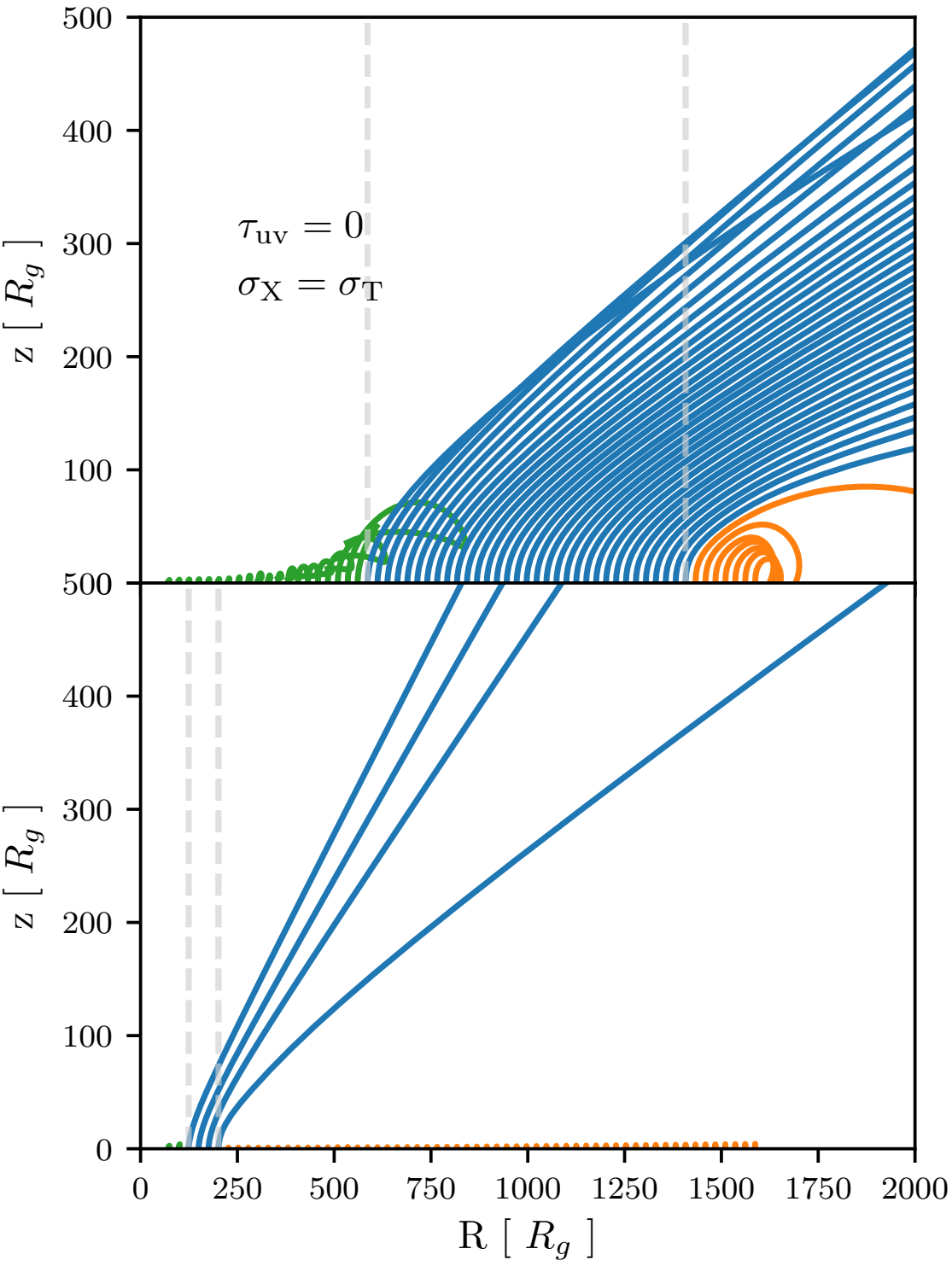

Figure 3.13: Top panel: Wind simulation with parameter values set to match P04: $f_x = 0.1$, $R_{\rm in} = 60\ R_g$, $v_0 = 2 \times 10^6$ cm/s, $T = 2.5 \times 10^4\ K$, and $n_0 = 2.5 \times 10^9$ cm^{-3}. We also set $\tau_{\rm UV} = 0$, and $\sigma_{\rm X} = \sigma_{\rm T}$ as it is done in P04. Bottom panel: Wind simulation with same parameters as the top panel, but using the standard $\tau_{\rm UV}$ and $\tau_{\rm X}$ of QWIND

Chapter 4

Improvements to the Qwind model

4.1 Introduction

As presented in chapter 3 (which is hereafter refered by its publication reference Quera-Bofarull et al. (2020) (Q20)), the QWIND code is a useful tool to efficiently explore the physics of line-driven winds without the computational burden of more expensive hydrodynamical codes. Nonetheless, the original model of RE10 presented some physical limitations on the treatment of the wind, particularly its strong dependence on the initial conditions of the wind that were completely undetermined (see section 3.8). In this chapter we present series of important improvements to the QWIND2 code. The resulting updated model is refered as QWIND3.

Firstly we calculate the fraction of power for each disc annuli in the UV band, f_{UV}, from the disc spectrum rather than have this as a free parameter (section 4.2). Secondly, we derive the initial conditions of the wind in section 4.3, based on the methodology introduced in CAK, and further developed in Abbott (1982); Pereyra et al. (2004); Pereyra (2005); Pereyra et al. (2006). This removes the wind's initial velocity and density as degrees of freedom of the system. Thirdly, we vastly enhance the treatment of the radiative transfer in the code, reconstructing the wind density and velocity field from the calculated gas trajectories. This allows us to individually trace the light rays coming from the accretion disc and the central X-ray source, correctly accounting for their attenuation. This is explained in detail in section 4.4. Lastly, we include the relativistic corrections from Luminari et al. (2020) in the calculation of the radiation force, solving the issue of superluminal winds, and we later compare our findings to Luminari et al. (2021).

The improvement in the modelling of the physical processes comes at the expense of added computational cost. We have ported the QWIND code to the Julia programming language (Bezanson et al., 2017), which is an excellent framework for scientific computing given its state of the art performance, and ease of use. The new code is made available to the community under the GPLv3 license on GitHub[1].

4.2 Radial dependence of $f_{\rm UV}$

We first address the validity of assuming a constant emitted UV fraction with radius. We can calculate its radial dependence using

$$f_{\rm UV}(R_{\rm d}) = \frac{\int_{E_1}^{E_2} B(E, T(R_{\rm d}))\,{\rm d}E}{\int_0^{\infty} B(E, T(R_{\rm d}))\,{\rm d}E}, \tag{4.2.1}$$

where $B(E,T)$ is the blackbody spectral radiance, $E_1 = 0.0038$ keV and $E_2 = 0.06$ keV (the standard definition of the UV transition band: (3200-200) Å), and $T^4(R_{\rm d}) = \mathcal{F}/\sigma_{\rm SB}$ (where $\mathcal{F}$ is defined in equation 3.2.5). In Figure 4.1, we plot the UV fraction as a function of radius for different $M_{\rm BH}$ and $\dot{m}$. The disc temperature is related to the total flux (given by setting $f_{\rm UV} = 1$ in equation 3.2.5) so $T^4 \propto (M\dot{M} f_{\rm NT}/R^3) \propto \dot{m}/M(R/R_{\rm g})^3$. Thus the disc temperature increases with decreasing $R/R_{\rm g}$, and for the fiducial case of $M_{\rm BH} = 10^8 {\rm M}_\odot$ this leads to the majority of the disc emission in the UV coming from $R/R_{\rm g} \leq 100$ (left panel of Figure 4.1: orange line). However, the increase in disc temperature at a given $R/R_{\rm g}$ for decreasing mass means that the same $\dot{m}$ for $M_{\rm BH} = 10^6 {\rm M}_\odot$ gives a UV flux which peaks at $R/R_{\rm g} > 100$, as the inner regions are too hot to emit within the defined UV bandpass (left panel of Figure 4.1: blue line). Conversely, for the highest BH masses of $M_{\rm BH} = 10^{10} {\rm M}_\odot$ the disc is so cool that it emits UV only very close to the innermost stable circular orbit (left panel of Figure 4.1: purple line). The universal upturn at $R = 10R_{\rm g}$ is caused by the the temperature sharply decreasing at the inner edge of the accretion disc due to the viscuous torque dropping to zero there.

Similarly, the right panel of Figure 4.1 shows the impact of changing $\dot{m}$ for the fiducial mass of $10^8 {\rm M}_\odot$. The dashed orange line shows the case $\dot{m} = 0.5$, as before, and the disc temperature decreases with decreasing $\dot{m}$ to 0.1 (dashed green line) and 0.05 (dashed blue line), reducing the radial extent of the UV-emitting zone.

[1] https://github.com/arnauqb/Qwind.jl

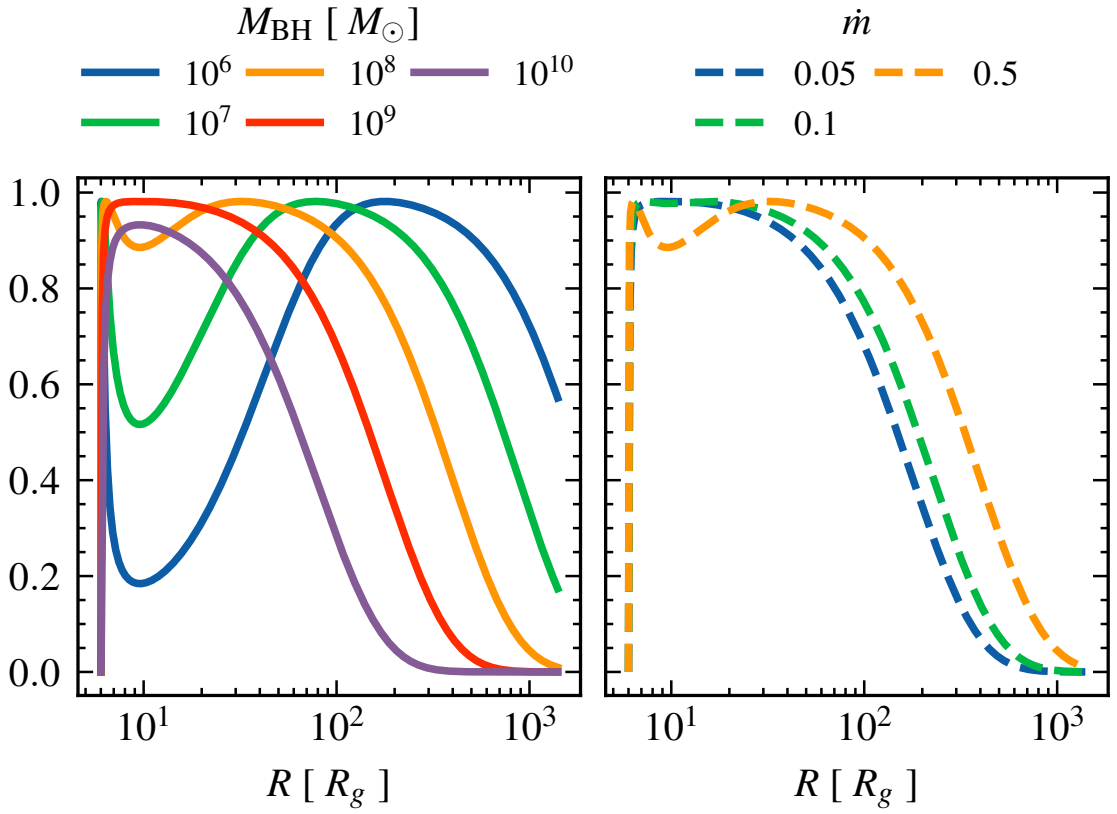

Figure 4.1: UV fraction as a function of disc radius. Left panel: dependence on $M_{\rm BH}$ for fixed $\dot{m} = 0.5$. Right panel: dependence on $\dot{m}$ for fixed $M_{\rm BH} = 10^8 {\rm M}_\odot$.

We note that the assumption used in Q20 (and many other UV line driven disc wind codes) of $f_{\rm UV}$ being a constant value is poor overall, highlighting the importance of including the radial dependence of the UV flux.

4.3 Initial conditions

As initial conditions, we determine the density and velocity at the base of the wind following the CAK formalism. Let us consider a wind originating from the top of an accretion disc. At low heights, a gas blob is mostly irradiated by the local region of the disc that is just below it. Since this local disc area can be considered to be at a uniform temperature, the direction of the radiation force is mostly upwards, and thus the wind flows initially vertically and can be considered a 1D wind. The corresponding equation describing the vertical motion is

$$\rho \frac{{\rm d}v_z}{{\rm d}t} = \rho \left(a^z_{\rm grav} + a^z_{\rm rad} \right) - \frac{\partial P}{\partial z}, \tag{4.3.1}$$

Even though the QWIND model does not include hydrodynamic forces when solving the 2D trajectories of gas parcels, we do include the force term due to gas pressure here, since it is necessary for deriving critical point like solutions (see subsection 4.3.1).

The study of 1D line-driven winds was pioneered by CAK, who defined a framework to find steady state solutions of the 1D wind equation. Their methodology can be extended to any particular geometry of the gravitational and radiation fields, in particular, Pereyra et al. (2006) (hereafter PE06) apply the CAK formalism to the study of cataclysmic variables (CVs). We here aim to further extend this approach to our case, by using the CAK formalism to calculate the properties of the 1D wind solutions from an accretion disc as initial conditions for the global 2D wind solution.

The core result of the CAK approach is that if a steady state solution of the 1D wind equation satisfies the following conditions:

- the velocity increases monotonically with height,
- the wind starts subsonic,
- the wind extends towards arbitrarily large heights,
- the wind becomes supersonic at some height,
- the velocity gradient is a continuous function of position,

then the wind must pass through a special point called the critical point z_c, which can be derived without solving the wind differential equation, and thus the global properties of the wind such as its mass loss rate can be determined without resolving the full wind trajectory.

The previously specified conditions for the existence of a critical point solution may not be satisfied for all of the wind trajectories that we aim to simulate. For instance, a wind trajectory that starts in an upward direction and falls back to the disc because it failed to achieve the escape velocity does not have a velocity that increases monotonically with height. Furthermore, eventually the wind trajectory is no longer vertical, and the 1D approach breaks down. Having considered these possibilities, and only for the purpose of deriving the initial conditions of the wind, we assume that these conditions hold, so that we can derive the wind mass loss rate at the critical point, which we in turn use to determine the initial conditions of the wind. The full 2D solution of the wind may then not satisfy these conditions.

4.3.1 Critical point derivation

Here, we aim to give a detailed and self-contained derivation of the initial conditions for launching the wind from the surface of the accretion disc. Let us write again the 1D wind equation,

$$\rho \frac{\mathrm{d}v_z}{\mathrm{d}t} = \rho(a^z_{\mathrm{rad}} - a^z_{\mathrm{grav}}) - \frac{\partial P}{\partial z}. \tag{4.3.2}$$

The left-hand side of the equation can be expanded to

$$\rho \frac{\mathrm{d}v_z}{\mathrm{d}t} = \rho \frac{\partial v_z}{\partial t} + \rho v_z \frac{\partial v_z}{\partial z}, \tag{4.3.3}$$

where we note that $\partial v_z/\partial t = 0$, since we are only interested in steady solutions that do not depend explicitly on time. For simplicity, we drop the partial derivative notation going forward, since only derivatives along the z direction are involved. We assume that the wind is isothermal, with an equation of state given by

$$P = c_s^2 \rho \tag{4.3.4}$$

where c_s is the isothermal sound speed, which is assumed constant throughout the wind. Using the mass conservation equation (equation 3.2.20), $\dot{M} = A\,\rho\,v_z$, where $A = 2\pi r \Delta r$, we can write

$$\frac{\mathrm{d}P}{\mathrm{d}z} = c_s^2 \frac{\mathrm{d}\rho}{\mathrm{d}z} = -\rho c_s^2 \left(\frac{\mathrm{d}A/\mathrm{d}z}{A} + \frac{\mathrm{d}v_z/\mathrm{d}z}{v_z} \right), \tag{4.3.5}$$

so we can rewrite equation 4.3.2 as

$$v_z \frac{\mathrm{d}v_z}{\mathrm{d}z} \left(1 - \frac{c_s^2}{v_z^2} \right) = a^z_{\mathrm{rad}} - a^z_{\mathrm{grav}} + c_s^2 \frac{\mathrm{d}A/\mathrm{d}z}{A}. \tag{4.3.6}$$

We now focus on the radiation force term, which is the sum of the electron scattering and line-driving components,

$$a^z_{\mathrm{rad}} = a^{\mathrm{es},z}_{\mathrm{rad}} + \mathcal{M}\, a^{\mathrm{es},z}_{\mathrm{rad}}. \tag{4.3.7}$$

When the wind is rapidly accelerating, as it is the case at low heights, the force multiplier is well approximated by its simpler form (see section 3.2.2),

$$\mathcal{M}(t) = k\, t^{-\alpha}, \tag{4.3.8}$$

where α is fixed to 0.6, k depends on the ionisation level of the gas (in the SK90 parameterisation), and $t = \kappa_{\mathrm{e}}\, \rho\, v_{\mathrm{th}}\, |\mathrm{d}v/\mathrm{d}z|^{-1}$. As discussed in section 3.5, the thermal velocity, v_{th} (equation 4.3.37), is computed at a fixed temperature of $T = 2.5 \times 10^4$ K. Once again making

use of the mass conservation equation we can write

$$\mathcal{M} = k\, t^{-\alpha} = \frac{k}{(\kappa_{\rm e}\, v_{\rm th}\, \rho)^{\alpha}} \left|\frac{dv}{dz}\right|^{\alpha} = \frac{k}{(\kappa_{\rm e} v_{\rm th}\,)^{\alpha}} \left(\frac{A}{\dot{M}} v_z \left|\frac{dv_z}{dz}\right|\right)^{\alpha} \tag{4.3.9}$$

and so the full equation to solve with all derivatives explicit is

$$\begin{aligned} v_z \frac{\mathrm{d}v_z}{\mathrm{d}z}\left(1 - \frac{c_s^2}{v_z^2}\right) = {} & a_{\rm rad}^{{\rm es},z}(z) - a_{\rm grav}^{z}(z) \\ & + a_{\rm rad}^{{\rm es},z}(z) \frac{k}{(\kappa_{\rm e} v_{\rm th}\,)^{\alpha}} \left(\frac{A(z)}{\dot{M}} v_z \left|\frac{dv_z}{dz}\right|\right)^{\alpha} \\ & + c_s^2 \frac{\mathrm{d}A(z)/\mathrm{d}z}{A(z)}. \end{aligned} \tag{4.3.10}$$

We assume that $\mathrm{d}v_z/\mathrm{d}z > 0$ always, so the absolute value can be dropped. It is convenient to introduce new variables to simplify this last equation. The first change we introduce is $W = v_z^2/2$, so that $v_z\, \mathrm{d}v_z/\mathrm{d}z = \mathrm{d}W/\mathrm{d}z$. Next, we aim to make the equation dimensionless, so we consider R as the characteristic length, $B_0 = GM_{\rm BH}/R^2$ as the characteristic gravitational acceleration value, $W_0 = GM_{\rm BH}/R = B_0 R$ as the characteristic W value, $A_0 = 2\pi R \Delta R$ as the characteristic A value, and finally we take the characteristic radiation force value to be

$$\gamma_0 = \frac{k}{(\kappa_{\rm e} v_{\rm th})^{\alpha}}\, a_{\rm rad,0}^{{\rm es},z}, \tag{4.3.11}$$

where $a_{\rm rad,0}^{{\rm es},z}$ is the low height approximation of the radiation force. Indeed, close to the disc's surface the radiation force is well approximated by considering the radiation force produced by an infinite plane at a temperature equal to the local disc temperature,

$$\boldsymbol{a}_{\rm rad,0}^{\rm es}(R) = \frac{3GM_{\rm BH}\dot{M}\kappa_{\rm e}}{8\pi^2 R^3 c} f_{\rm UV} f_{\rm NT}\ \hat{\boldsymbol{z}}, \tag{4.3.12}$$

where we also have ignored attenuation. The radiation force is then vertical and almost constant at small heights ($z \lesssim 0.1 R_{\rm g}$).

With all this taken into account, we can write

$$\begin{aligned} B_0 \frac{dw}{dx}\left(1 - \frac{s}{w}\right) = {} & -a_{\rm grav}^{z} + a_{\rm rad}^{{\rm es},z}\left(1 + \frac{k}{(\kappa_{\rm e} v_{\rm th})^{\alpha}} \left(\frac{A}{\dot{M}} B_0 \frac{dw}{dx}\right)^{\alpha}\right) \\ & + c_s^2 \frac{\mathrm{d}A/\mathrm{d}z}{A}, \end{aligned} \tag{4.3.13}$$

where we have defined $x = z/R$, $w = W/W_0$, and $s = c_s^2/(2W_0)$. We also define $a = A/A_0$, and $\varepsilon = \dot{M}/\dot{M}_0$ with

$$\dot{M}_0 = \alpha(1-\alpha)^{(1-\alpha)/\alpha} \frac{(\gamma_0 A_0)^{1/\alpha}}{(B_0 A_0)^{(1-\alpha)/\alpha}}. \tag{4.3.14}$$

This last definition may seem a bit arbitrary, but it is taken such that $\varepsilon = 1$ corresponds to

the classical CAK $\dot{M}$ value for O-stars. equation 4.3.13 then becomes

$$\frac{\mathrm{d}w}{\mathrm{d}x}\left(1-\frac{s}{w}\right)=\frac{(-a^z_{\mathrm{grav}}+a^{\mathrm{es},z}_{\mathrm{rad}})}{B_0}+\frac{1}{\alpha^\alpha(1-\alpha)^{1-\alpha}}\frac{a^{\mathrm{es},z}_{\mathrm{rad}}}{a^{\mathrm{es},z}_{\mathrm{rad},0}}\left(\frac{a}{\varepsilon}\frac{\mathrm{d}w}{\mathrm{d}x}\right)^\alpha + \frac{4sx}{a}, \tag{4.3.15}$$

where we have used

$$a=\frac{A}{A_0}=\frac{2\pi r\Delta r}{2\pi r_0\Delta r_0}=\frac{r^2}{r_0^2}, \tag{4.3.16}$$

so that

$$\frac{c_s^2}{B_0}\frac{\mathrm{d}A/\mathrm{d}z}{A}=\frac{4sx}{a}. \tag{4.3.17}$$

We note that we have assumed that the area A changes with z like the 2D solution, despite the fact that we are considering here a 1D wind. This small correction guarantees that we find critical-point like solutions for all initial radii, since it guarantees that the CAK conditions for the existence of a critical point are satisfied. Finally, we define

$$f=\frac{1}{\alpha^\alpha(1-\alpha)^{1-\alpha}}\frac{a^{\mathrm{es},z}_{\mathrm{rad}}}{a^{\mathrm{es},z}_{\mathrm{rad},0}}, \tag{4.3.18}$$

and

$$h=\frac{(a^z_{\mathrm{grav}}-a^{\mathrm{es},z}_{\mathrm{rad}})}{B_0}-4sxa, \tag{4.3.19}$$

so that

$$\frac{\mathrm{d}w}{\mathrm{d}x}\left(1-\frac{s}{w}\right)=-h(x)+f(x)\left(\frac{a}{\varepsilon}\frac{\mathrm{d}w}{\mathrm{d}x}\right)^\alpha, \tag{4.3.20}$$

which is the dimensionless wind equation. The choice of sign in $h(x)$ is to make the further steps clearer. It is useful to interpret this equation as an algebraic equation for $w'=\mathrm{d}w/\mathrm{d}x$,

$$F(x,w,w')=w'\left(1-\frac{s}{w}\right)+h(x)-f(x)\left(\frac{a}{\varepsilon}w'\right)^\alpha=0. \tag{4.3.21}$$

This has the same general form as Equation 26 in CAK, which applies to a spherical wind from a star, but the functions $h(x)$ and $f(x)$ are different. We note that $f(x)>0$ and $0<\alpha<1$, but $h(x)$ can have either sign. (Also note that we have chosen the opposite sign for $h(x)$ to CAK, for later convenience). Given values of x and ε, we can distinguish 5 different regions of solutions for w' (we follow the original enumeration of regions by CAK):

- Subsonic stage ($w<s$): We distinguish two cases
  - Region V: If $h(x)<0$, then all the terms in Equation 4.3.21 are negative and there is no solution for w'.
  - Region I: If $h(x)>0$, $F(w'=0)$ is positive and as w' increases, F goes to negative

values crossing $F = 0$ once, so there is one solution for w'.

- Supersonic stage ($w > s$): We have three regions
  - Region III: If $h(x) < 0$, $F(w' = 0)$ is negative and as w' increases, F goes to positive values crossing $F = 0$ once, so there is one solution for w'.
  - If $h(x) > 0$, $F(w' = 0)$ is positive, then F initially decreases until its minimum, $w'_{\rm min}$, and then increases again. If $F(w'_{\rm min}) > 0$, we have no solution for w' and if $F(w'_{\rm min}) \leq 0$ we have two solutions, which are the same if $F(w'_{\rm min}) = 0$. The minimum can be found by solving

$$\frac{\partial F}{\partial w'} = 0, \tag{4.3.22}$$

    which gives

$$w'_{\rm min} = \left(\frac{1 - s/w}{\alpha f (a/\varepsilon)^\alpha} \right)^{\frac{1}{\alpha - 1}}, \tag{4.3.23}$$

    so we have
    - Region IV: If $F(w'_{\rm min}) > 0$, there is no solution.
    - Region II: If $F(w'_{\rm min}) \leq 0$, there are two solutions, one with $w' < w'_{\rm min}$ and the other with $w' > w'_{\rm min}$

We assume that the wind starts subsonic ($w < s$), so it has to start in Region I, since that is the only subsonic region with a solution. We note that $h(x \to \infty) < 0$, since for large x both the gravitational and radiation force are small. Assuming that the wind ends as supersonic (w>s) and extends to $x \to \infty$, this means that the wind must end at Region III. However, because $h(x) > 0$ in Region I and $h(x) < 0$ in Region III, these two regions must be connected by Region II in between. At the boundary between Regions I and II, $w = s$ and $h(x) > 0$, while at the boundary between Regions II and III, $w > s$ and $h(x) = 0$.

Considering first the boundary between Regions I and II, setting $w = s$ in equation 4.3.21 gives

$$h - f \left(\frac{a}{\varepsilon} w' \right)^\alpha = 0, \tag{4.3.24}$$

with $h > 0$. Considering equation 4.3.23 for $w'_{\rm min}$ as $w \to s^+$, we find that the wind solution at this boundary must lie on the branch with $w' < w'_{\rm min}$.

Considering next the boundary between Regions II and III, setting $h = 0$ in equation 4.3.21 (neglecting the $w' = 0$ solution) gives

$$1 - \frac{s}{w} - f \left(\frac{a}{\varepsilon} \right)^\alpha w'^{\alpha - 1} = 0, \tag{4.3.25}$$

Again using equation 4.3.23 and $w > s$, we find that the wind solution at this boundary must lie on the branch with $w' > w'_{\min}$.

However, we assume that w' must be continuous throughout the wind, which would not be the case if the two branches of region II were not connected. Therefore, both branches of region II must coincide at some point, so the condition

$$F(w'_{\min}) = 0 \tag{4.3.26}$$

must hold at that point, with $w' = w'_{\min}$ for both branches. This point is in fact the critical point of the solution, and $\partial F/\partial w' = 0$ there. Upon substitution of $w'_{\min}$, this condition is equivalent to

$$\varepsilon \left(1 - \frac{s}{w}\right) = \alpha(1-\alpha)^{\frac{1-\alpha}{\alpha}} \frac{f^{1/\alpha} a}{h^{\frac{1-\alpha}{\alpha}}}. \tag{4.3.27}$$

The right-hand side of the equation is usually referred to as the Nozzle function $\mathcal{N}$,

$$\mathcal{N}(x) = \alpha(1-\alpha)^{\frac{1-\alpha}{\alpha}} \frac{f^{1/\alpha} a}{h^{\frac{1-\alpha}{\alpha}}}. \tag{4.3.28}$$

We define $x = x_c$ to be the position of the critical point. We now assume that at the critical point the wind is highly supersonic ($w \gg s$). We verify this assumption in subsection 5.1.1. Then $1 - s/w \approx 1$, and so the normalised mass loss rate is given by

$$\varepsilon = \mathcal{N}(x_c). \tag{4.3.29}$$

We now show that the location of the critical point x_c is at the minimum of $\mathcal{N}(x)$. Let us consider the total derivative of F with respect to x taken along a wind solution. Since $F = 0$ at all points along the solution,

$$\frac{\mathrm{d}F}{\mathrm{d}x} = \frac{\partial F}{\partial x} + \frac{\partial F}{\partial w} w' + \frac{\partial F}{\partial w'} \frac{\mathrm{d}w'}{\mathrm{d}x} = 0. \tag{4.3.30}$$

Because of our assumption $w \gg s$, we have $\frac{\partial F}{\partial w} = 0$, and, at the critical point, $\frac{\partial F}{\partial w'} = 0$, so that

$$\left.\frac{\mathrm{d}F}{\mathrm{d}x}\right|_{w'_{\min}, x_c} = \left.\frac{\partial F}{\partial x}\right|_{w'_{\min}, x_c} = 0, \tag{4.3.31}$$

which gives (a prime denotes $\mathrm{d}/\mathrm{d}x$)

$$h' - \left(\frac{w'_{\min}}{\varepsilon}\right)^{\alpha} \frac{\mathrm{d}}{\mathrm{d}x}\left(f a^{\alpha}\right) = 0. \tag{4.3.32}$$

Now using equation 4.3.23 for $w'_{\min}$ along with equation 4.3.29 and equation 4.3.28, we obtain $w'_{\min} = \frac{\alpha}{(1-\alpha)} h$. Substituting in equation 4.3.32 and using equation 4.3.29 and equation 4.3.28

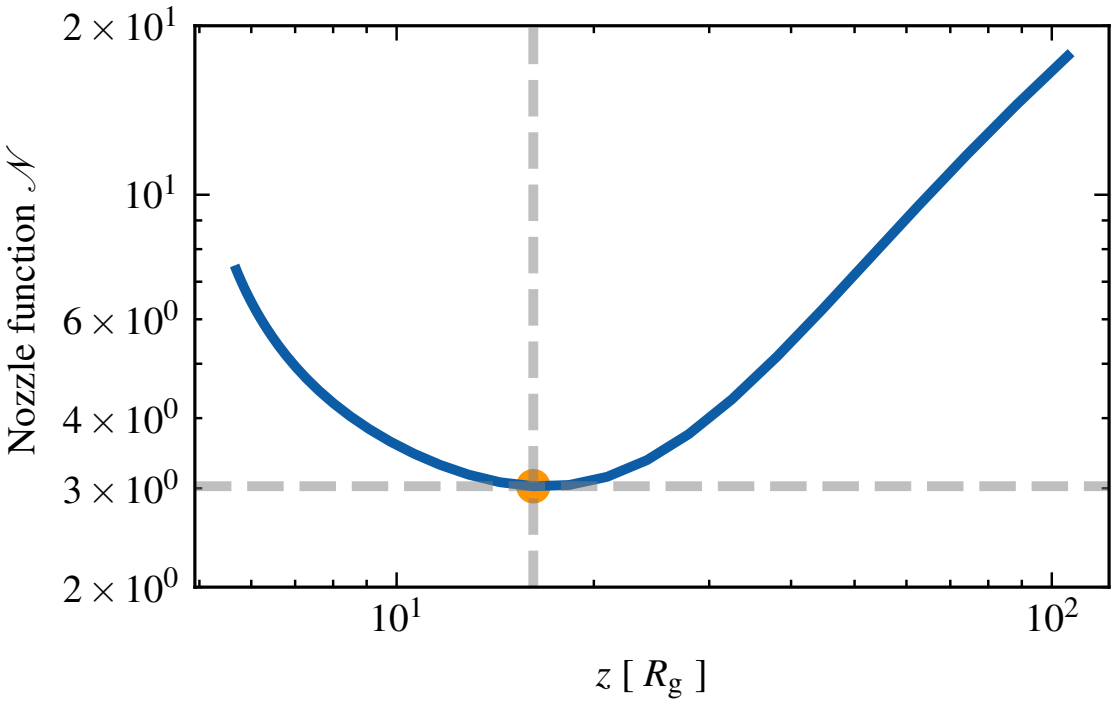

Figure 4.2: Nozzle function for $M_{\rm BH} = 10^8 {\rm M}_\odot$, $\dot{m} = 0.5$, $k = 0.03$, and $R = 20 R_{\rm g}$

again, we obtain

$$(1-\alpha)\frac{h'}{h} - \frac{1}{fa^\alpha}\frac{\mathrm{d}}{\mathrm{d}x}\left(fa^\alpha\right) = 0. \tag{4.3.33}$$

Comparing to equation 4.3.28, we see that this is equivalent to the condition $\mathrm{d}\mathcal{N}/\mathrm{d}x = 0$. Therefore the critical point happens at an extremum of $\mathcal{N}(x)$, but since the nozzle function is not upper bounded, the extremum has to be a minimum. We have therefore shown that the critical point x_c corresponds to the minimum of the nozzle function $\mathcal{N}(x)$.

In Figure 4.2, we plot the nozzle function for $M_{\rm BH} = 10^8 {\rm M}_\odot$, $\dot{m} = 0.5$, $k = 0.03$, and $R = 20 R_{\rm g}$ and we highlight the position of the critical point. The value of the nozzle function at the critical point determines the mass-loss rate along the streamline, through $\dot{M} = \varepsilon \dot{M}_0$, so that the surface mass loss rate is given by

$$\dot{\Sigma} = \frac{\dot{M}}{A}. \tag{4.3.34}$$

It is interesting to point out that the position of the critical point and the value of ϵ do not depend on the chosen value of k in the force multiplier parametrisation (equation 4.3.8), however, the mass loss rate does depend on k through the value of $\dot{M}_0$. In the SK90 parametrisation, k is a function of the ionisation state of the gas, $k = k(\xi)$, so the mass loss rate directly depends on the ionisation conditions at the critical point location. Since this would make

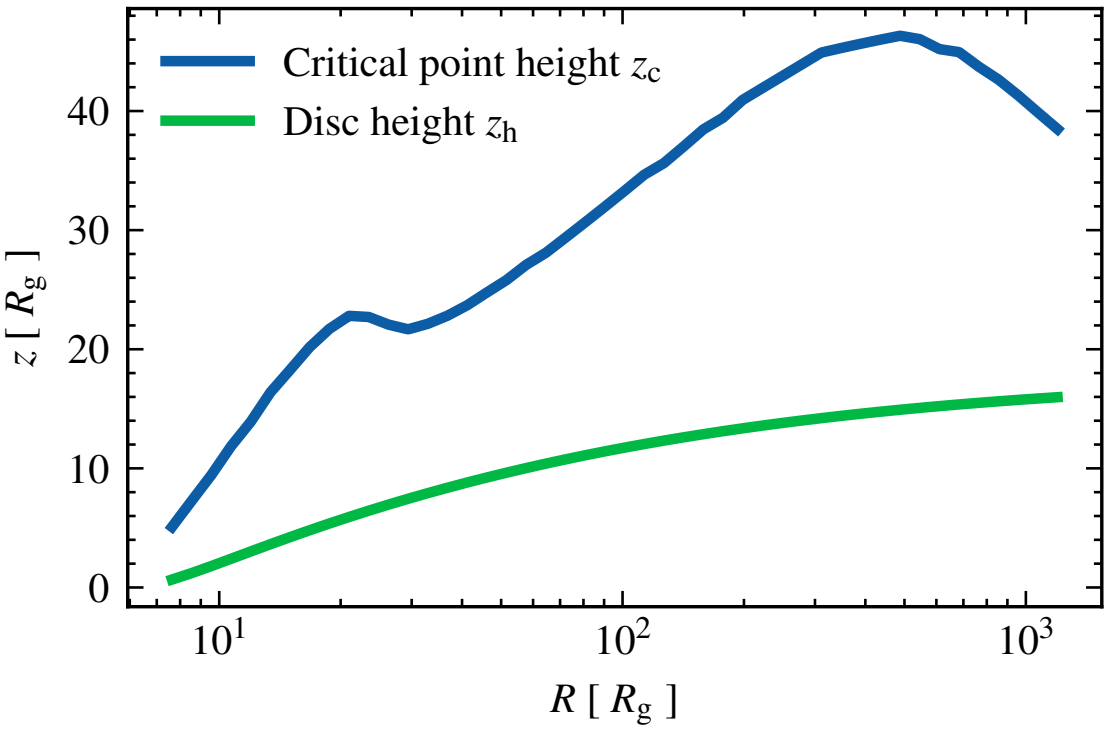

Figure 4.3: Position of the critical point z_c as a function of radius, for $M_{\rm BH} = 10^8 {\rm M}_\odot$ and $\dot{m} = 0.5$.

our results dependent on the modelling of the vertical structure of the disc, which is out of scope for the purpose of this work, we assume that the gas is always ionised when it reaches the critical point, so we take $k = 0.03$, corresponding to the minimum value of k in SK90. Similarly, we set the initial height of the wind to $z = 0$ to avoid dependencies on the disc vertical structure.

The location of the critical point as a function of radius is plotted in Figure 4.3, where we also plot the height of the disc,

$$z_{\rm h}(R) = \frac{\kappa_e \mu_e \mathcal{F}(R) R^3}{G M_{\rm BH} c}, \tag{4.3.35}$$

defined as the point of equality between the vertical gravitational and radiation force. Overall, we notice that the critical point height increases slowly with radius, except for a bump at $R \sim 20 R_{\rm g}$ which is caused by the UV fraction dependence with radius (see Figure 4.1). For radii $R \lesssim 50\, R_{\rm g}$ the critical point height is comparable to the disc radius, so our approximation that streamlines are vertical at that point may not be applicable. We assess the validity of this assumption in subsection 5.1.1.

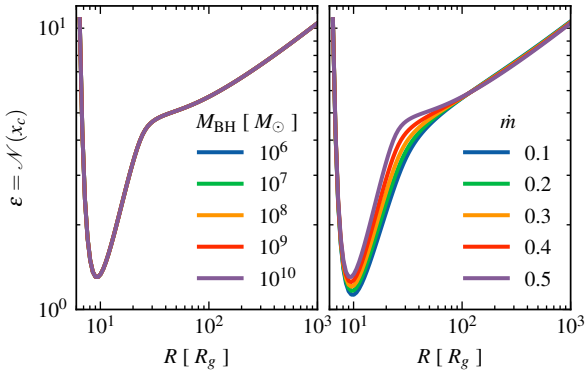

Figure 4.4: Value of the nozzle function at the critical point ($\varepsilon = \mathcal{N}(x_c)$) as a function of radius for varying $M_{\rm BH}$ (left panel) with $\dot{m} = 0.5$ and varying $\dot{m}$ (right panel) with $M_{\rm BH} = 10^8 {\rm M}_\odot$

4.3.2 Scaling of the initial conditions with BH properties

To explore the dependence of the wind properties on the BH parameter space, it is useful to assess how the initial number density and velocity of the wind scale with $M_{\rm BH}$ and $\dot{m}$. To this end, we need to determine how the values of ε and $\dot{\Sigma}_0$ change with $M_{\rm BH}$ and $\dot{m}$. For this analysis, we ignore the dependence of $f_{\rm UV}(R)$ on M and $\dot{m}$. We also have $v_{\rm th}(R) \propto T^{1/2} \propto (M_{\rm BH}\dot{M}/R^3)^{1/8}$ (using equation 3.2.5). Accounting for the fact that the disc size scales as $R \propto R_{\rm g} \propto M_{\rm BH}$, this gives $v_0 = v_{\rm th} \propto (\dot{m}/M_{\rm BH})^{1/8}$, where v_0 is the initial velocity. This is a weak dependence, so we ignore it here. Looking at equation 4.3.11, and using equation 4.3.12, we get $\gamma_0 \propto M_{\rm BH}\dot{M}/R^3 \propto \dot{m}/M_{\rm BH}$. Similarly, $B_0 \propto M_{\rm BH}/R^2 \propto 1/M_{\rm BH}$. Using equation 4.3.14, we then have $\dot{\Sigma}_0 \propto \dot{M}_0/A_0 \propto \gamma_0^{1/\alpha}/B_0^{(1-\alpha)/\alpha} \propto \dot{m}^{1/\alpha}/M_{\rm BH}$.

The scaling of $\varepsilon = \mathcal{N}(x_c)$ is a bit more complicated, since it depends on the exact position of the critical point for each value of $M_{\rm BH}$, $\dot{m}$, and R. In Figure 4.4, we plot the values of ε as a function of radius for varying $M_{\rm BH}$ (left panel) and $\dot{m}$ (right panel), ignoring the dependence of $f_{\rm UV}$ with $M_{\rm BH}$ and $\dot{m}$ (we set $f_{\rm UV} = 1$). We note that ε does not scale with $M_{\rm BH}$, and changes very little with $\dot{m}$. Including the dependence of $f_{\rm UV}$ with $M_{\rm BH}$ and $\dot{m}$, effectively reduces the value of ε at the radii where $f_{\rm UV}$ is small, but it does not change substantially in the radii that we would expect to launch an escaping wind. We can then conclude that ε has a very weak scaling with $M_{\rm BH}$ and $\dot{m}$ so that

$$\dot{\Sigma} \propto \dot{\Sigma}_0 \propto \frac{\dot{m}^{\frac{1}{\alpha}}}{M_{\rm BH}}, \tag{4.3.36}$$

which is the same result that Pereyra et al. (2006) found in applying the CAK formalism to cataclysmic variables.

4.3.3 Wind initial conditions

We assume that the wind originates from the disc surface with an initial velocity v_0 equal to the thermal velocity (or isothermal sound speed) at the local disc temperature,

$$v_{\rm th}(R) = \sqrt{\frac{k_{\rm B}T(R)}{\mu\, m_p}}. \tag{4.3.37}$$

Given that the critical point is close to the disc surface, and that the wind is supersonic at the critical point, this is a good starting point. Since mass conservation holds, the initial number density of the wind can then be calculated as

$$n_0(R) = \frac{\dot{\Sigma}(R)}{v_{\rm th}(T(R))\,\mu\, m_{\rm p}}, \tag{4.3.38}$$

where $\dot{\Sigma}(R)$ is the mass loss rate per unit area at the critical point. In Figure 4.5, we plot the initial number density and velocity for $M_{\rm BH} = 10^8\,{\rm M}_\odot$, $\dot{m} = 0.5$. We note that the initial velocity stays relatively constant, only varying by a factor of ~ 3 across the radius range. However, the initial number density varies by more than 5 orders of magnitude, showing that the assumption of a constant density at the base of the wind used in the previous versions of the model was poor.

Comparison to other models

As a partial test of this new section of the code, we can compare our findings with Nomura et al. (2013) (hereafter N13), in which the authors also use the sonic velocity as the initial velocity of the wind, and derive the initial density profile by assuming the same functional form for the mass loss rate as in CAK, but using the AGN $M_{\rm BH}$ and $\dot{m}$ instead. We note that the use of the CAK formula directly for accretion discs may not be appropriate because the geometry of the system is very different from stellar winds. Additionally, in N13 the dependence of $f_{\rm UV}$ on the disc radius is not considered. Hence we first hardwire $f_{\rm UV}$ for the comparison. This comparison is shown in the upper panels of Figure 4.6 for different $M_{\rm BH}$ (left, all at $\dot{m} = 0.5$), and (right) for $M_{\rm BH}$ fixed at $10^8\,{\rm M}_\odot$ with different $\dot{m}$. It is clear that the initial density now derived in Qwind3 (dashed lines) has a steeper decrease with radius than in N13. This is probably due to their use of the direct CAK formula, which assumes a spherical geometry rather than an accretion disc. However, the inferred densities are within an order of magnitude of each other, and both approaches give a linear scaling of the initial number density profile with $M_{\rm BH}$, but Qwind3 gives an almost quadratic scaling with $\dot{m}$, compared to a linear one for N13 (see subsection 4.3.2).

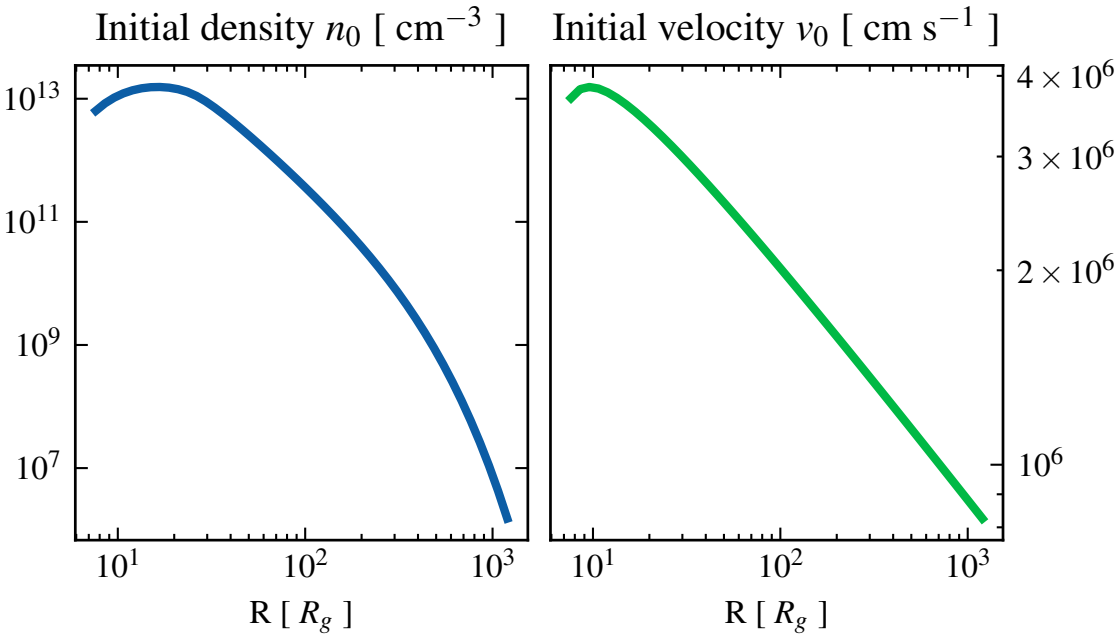

Figure 4.5: Initial conditions at the base of the wind as a function of radius. The original QWIND code assumed constant initial density and velocity across the disc, and these were free parameters. We now calculate these from first principles. The left panel shows that the initial density changes by a factor of 10^6, very different to the original assumption, while the right panel (note change in y axis scale) shows that the initial velocity changes by less than a factor 10.

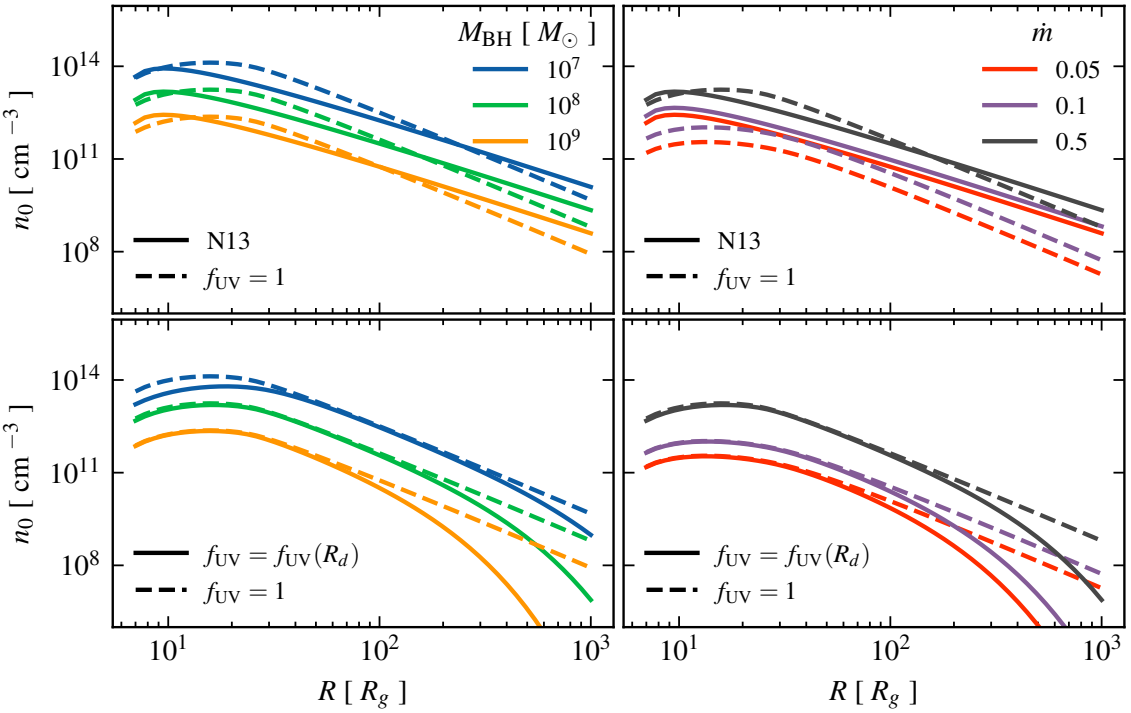

Figure 4.6: Initial density as a function of radius. In the top panels we compare with the results of N13 (solid lines), the only other disc wind code which used UV line driving to calculate the initial density. That code assumes constant f_{UV}, so we fix $f_{\rm UV} = 1$ in QWIND to compare results (dashed lines). In the bottom panels we compare the QWIND results with $f_{\rm UV} = 1$ (dashed lines) with the full QWIND results for $f_{\rm UV}(R_{\rm d})$. Left and right panels show results for fixed $\dot{m} = 0.5$, and vary $M_{\rm BH} \in (10^7, 10^8, 10^9)\,{\rm M}_\odot$. Right panels: We fix $M_{\rm BH} = 10^8\,{\rm M}_\odot$ and vary $\dot{m} \in (0.05, 0.1, 0.5)$.

The lower panels of Figure 4.6 show instead the comparison of the QWIND models using the self consistent $f_{\rm UV}$ with its radial dependence (solid lines) instead of assuming $f_{\rm UV} = 1$ (dashed lines). There is a very strong drop in the initial density at radii where $f_{\rm UV}$ drops (see Figure 4.1). This shows the importance of including the self-consistent calculation of $f_{\rm UV}$ in QWIND3.

4.4 Qwind radiation transfer

In Q20, the radiation transfer is treated in a very simple way. The disc atmosphere (i.e. the wind) is assumed to have constant density, and so the line of sight absorption does not take into consideration the full geometry and density structure of the wind (see section 2 of Q20). Furthermore, the UV optical depth is measured from the centre of the disc, and assumed to be the same for radiation from all disc patches, regardless of the position and angle relative to the gas parcel. In this section, we improve QWIND's radiative transfer model,

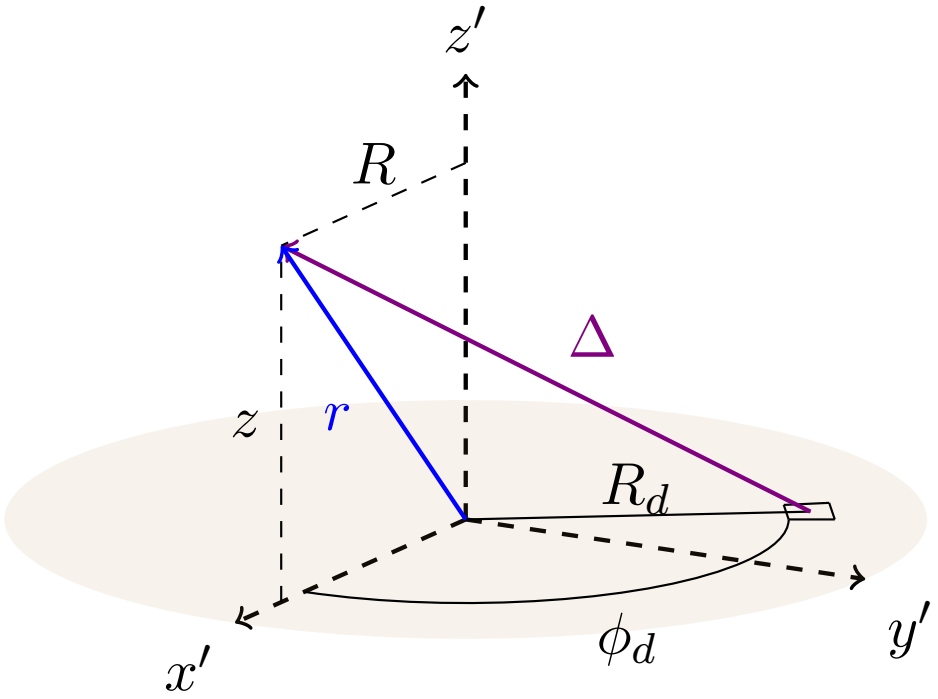

Figure 4.7: Diagram of the disc-wind geometry. The blue line corresponds to the light path an X-ray photon takes, while the violet line corresponds to an example of a UV light ray from the accretion disc.

by reconstructing the wind density from the gas blob trajectories, thus accounting fully for the wind geometry. The disc is assumed to be flat and thin, with constant height $\bar{z}_{\rm h} = 0$, thus we do not model the effect of the disc itself on the radiation transfer. To illustrate the improvements, we consider our fiducial model with $M_{\rm BH} = 10^8 {\rm M}_\odot$, and $\dot{m} = 0.5$, and present the ray tracing engine of the code in an arbitrary wind solution. We discuss particular physical implications and results in chapter 5.

4.4.1 Constructing the density interpolation grid

Given a collection of trajectories, we aim to obtain the wind density field at every point in space. The first step is to delimit where the wind is spatially located by computing the concave hull that contains all the points of all wind trajectories. We use the algorithm described in Moreira & Santos (2007) and implemented in Stagner (2021). The resulting concave set is illustrated in Figure 4.8. Outside the concave hull, the density is set to the vacuum density which is defined to be $n_{\rm vac} = 10^2$ cm^{-3}. Since the density varies by orders of magnitude within the wind, we compute the density at a point by linearly interpolating $\log_{10} n$ in logarithmic space ($\log R$ - $\log z$) from the simulated wind trajectories. We use the interpolation algorithm LinearNDInterpolator from SciPy (Virtanen et al., 2020). The

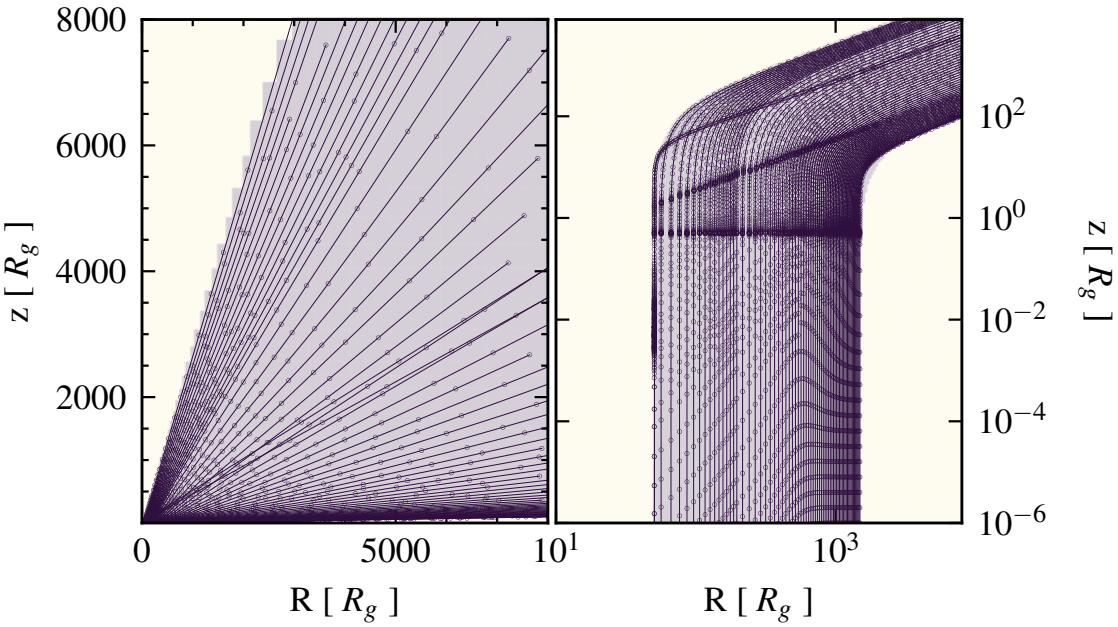

Figure 4.8: Gas parcel trajectories encapsulated by the concave hull containing the points. Left panel on linear scale and right panel on logarithmic scale. Note that the non-convexity of the wind prevents us from using a simpler convex hull envelope.

resulting density map is shown in Figure 4.9. We note that using a concave hull envelope is important, since the interpolation algorithm we use restricts the interpolation space to the convex hull of the input points, which, due to non-convexity of the wind geometry, would otherwise lead us to overestimate the obscuration in certain regions.

Once we have built the interpolator, we construct a rectilinear grid with the interpolated values. This allows us to implement an efficient ray tracing algorithm to compute the UV and X-ray optical depths. The vertical coordinates of the grid nodes are logarithmically spaced from 10^{-6} R_g to the wind's maximum height. The horizontal coordinates are taken at the initial positions of the wind's trajectories, plus an additional range logarithmically spaced from the initial position of the last streamline to the highest simulated R coordinate value.

4.4.2 Ray tracing

To compute the optical depth along different lines of sight, we need to calculate an integral along a straight path starting at a disc point $(R_\mathrm{d}, \phi_\mathrm{d}, 0)$ to a point (R, ϕ, z). Due to the axisymmetry of the system, the radiation acceleration is independent of ϕ so we can set $\phi = 0$. We can parametrise the curve in the Cartesian coordinate system with a single

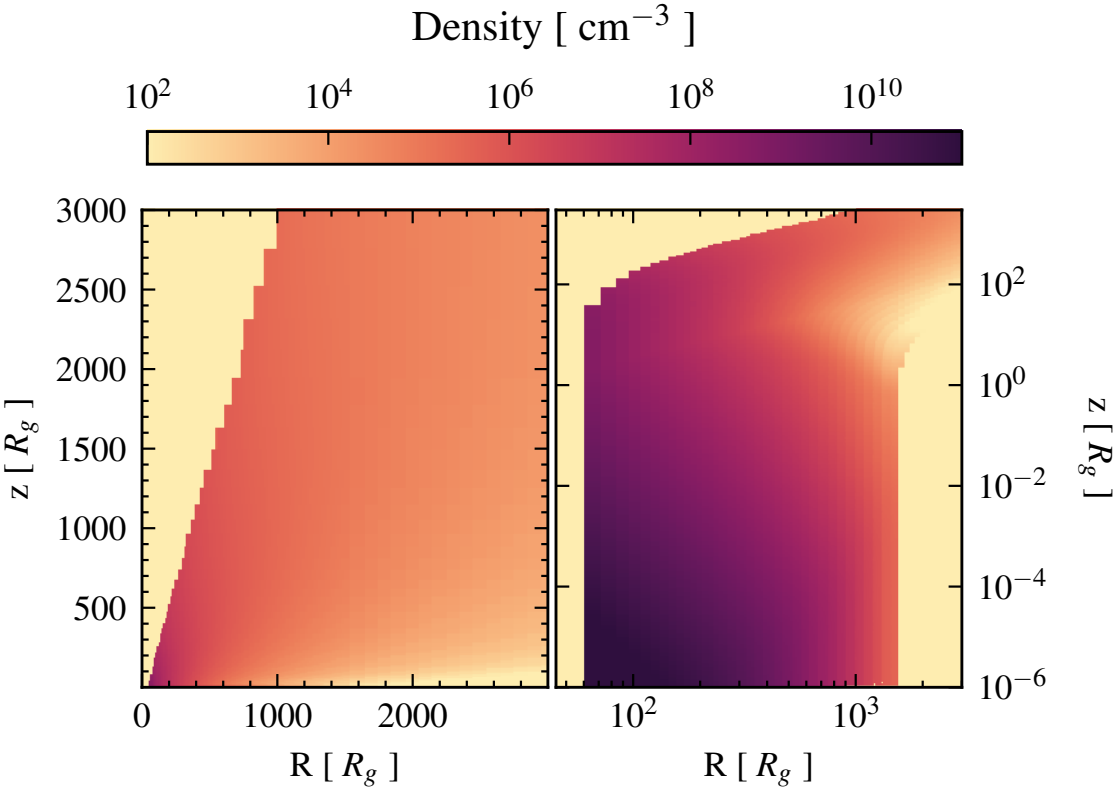

Figure 4.9: Interpolated density grid from the simulated wind positions and densities. Left panel: position in linear scale. Right panel: position in logarithmic scale.

parameter $t \in [0,1]$, (see Figure 4.7),

$$\begin{aligned} x(t) &= R_{\rm d} \cos\phi_{\rm d}\,(1-t) + t\,R, \\ y(t) &= R_{\rm d} \sin\phi_{\rm d}\,(1-t), \\ z(t) &= t\,z \end{aligned} \tag{4.4.1}$$

so that the cylindrical radius varies along the path as

$$R_t^2(t) = R_{\rm d}^2(1-t)^2 + t^2R^2 + 2R_{\rm d}R\cos\phi_{\rm d}\,t(1-t), \tag{4.4.2}$$

and $\phi(t) = \arctan\,(y(t)/x(t))$. In this parametrisation, $t = 0$ points to the disc plane point, and $t = 1$ to the illuminated wind element. The integral to compute is thus

$$\tau = \Delta \int_0^1 \sigma(t)\; n(t)\,{\rm d}t, \tag{4.4.3}$$

where Δ is the total path length defined earlier. Given a rectilinear density grid in the R-z plane, we compute the intersections of the light ray with the grid lines, $\{R_i, z_i\}$, such that we can discretise the integral as,

$$\tau \approx \sum_i \sigma(R_i, z_i)\; n(R_i, z_i)\Delta d_i, \tag{4.4.4}$$

where Δd_i is the 3D distance between the i-th intersection point and the $(i-1)$-th,

$$\Delta d_i = \sqrt{R_i^2 + R_{i-1}^2 + (z_i - z_{i-1})^2 - 2R_iR_{i-1}\cos(\phi_i - \phi_{i-1})}, \tag{4.4.5}$$

To find the intersections, we need to calculate whether the light ray crosses an R_i grid line or a z_i grid line. We start at the initial point $(R_{\rm d}, \phi_{\rm d}, 0)$, and compute the path parameter t_R to hit the next R grid line R_i by solving the second degree equation $R(t_R) = R_i$, and similarly for the next z_i line, $t_z = z_i/z$. The next intersection is thus given by the values of $R(t_m)$ and $z(t_m)$ where $t_m = \min(t_R, t_z)$. Geometrically, the projection of the straight path onto the $(R-z)$ grid is in general a parabola as we can see in Figure 4.10.

4.4.3 X-ray optical depth

The X-ray opacity depends on the ionisation level of the gas and is assumed to have the same functional form as Q20,

$$\sigma_{\rm X}(\xi) = \begin{cases} \sigma_{\rm T} & \text{if } \xi > 10^5 \text{erg cm s}^{-1} \\ 100\sigma_{\rm T} & \text{if } \xi \leq 10^5 \text{erg cm s}^{-1} \end{cases}, \tag{4.4.6}$$

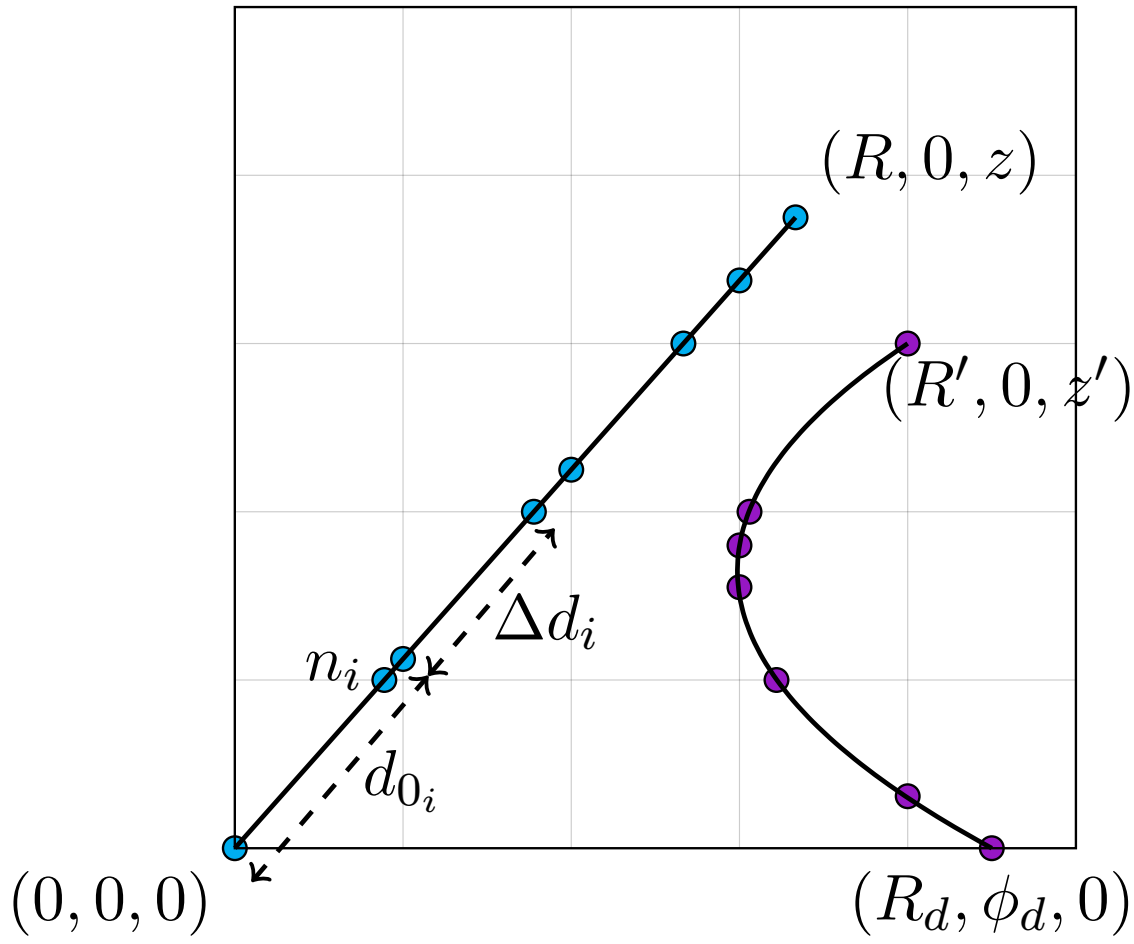

Figure 4.10: Projections of two typical light rays onto the $R - z$ interpolation grid. The X-ray radiation (path with blue dots) is assumed to come from the centre of the grid $(0, 0)$, so the projection of the light curve onto the $R - z$ grid is always a straight line. However, for the UV case (purple dots), the light ray can originate from any $\phi_{\rm d}$, so the path on the interpolation grid is, in general, a parabola.

where $\sigma_{\rm T}$ is the Thomson scattering cross section, ξ is the ionisation parameter,

$$\xi = \frac{4\pi F_{\rm X}}{n}, \tag{4.4.7}$$

and $F_{\rm X}$ is the X-ray radiation flux, $F_{\rm X} = L_{\rm X}\exp(-\tau_{\rm X})/(4\pi r^2)$. We notice that to compute the value of $\tau_{\rm X}$ we need to solve an implicit equation, since the optical depth depends on the ionisation state of the gas which in turn depends on the optical depth. One thus needs to compute the distance $d_{\rm X}$ at which the ionisation parameter drops below $\xi_0 = 10^5$ erg cm s^{-1},

$$\xi_0 - \frac{L_{\rm X}}{n d_{\rm X}^2}\exp\left(-\tau_{\rm X}\right) = 0. \tag{4.4.8}$$

This equation needs to be tested for each grid cell along the line of sight as it depends on the local density value n. Therefore for a cell at a distance d_{0_i} from the centre, density n_i, and intersection length Δd_i with the light ray (see Figure 4.10), the contribution $\Delta\tau_{\rm X}$ to the optical depth is

$$\Delta\tau_{\rm X} = \sigma_{\rm T}\, n_i \cdot \left[\max(0, d_{\rm X} - d_{0_i}) + 100 \cdot \max(0, \Delta d_i - (d_{\rm X} - d_{0_i}))\right], \tag{4.4.9}$$

where $d_{\rm X}$ is calculated from

$$\xi_0 - \frac{L_{\rm X}}{n_i d_{\rm X}^2}\exp\left(-\tau_{0_i} - \sigma_{\rm T}\cdot n_i \cdot (d_{\rm X} - d_{0_i})\right) = 0, \tag{4.4.10}$$

where τ_{0_i} is the accumulated optical depth from the centre to the current position. We solve the equation numerically using the bisection method. In Figure 4.11 we plot the X-ray optical depth grid for our example wind. We observe that there is a region where $\tau_{\rm X} \gg 1$ at very low heights. This shadow is caused by the shielding from the inner wind, which makes the ionisation parameter drop below ξ_0, substantially increasing the X-ray opacity. As we will later discuss in the results section, the shadow defines the acceleration region of the wind, where the force multiplier is very high.

4.4.4 UV optical depth

The UV opacity calculation is significantly simpler than that for the X-rays, since we assume that the line shift due to the Doppler effect in an accelerating wind is sufficient to always reveal fresh, unabsorbed continuum, so that the opacity is constant at the Thomson (electron scattering) value, $\sigma(R_i, z_i) = \sigma_{\rm T}$. In Figure 4.12, we plot the UV optical depth as a function of R and z for light rays originating at the disc position $R_{\rm d} = 500$, $\phi_{\rm d} = 0$. Nevertheless, there are many more sight-lines to consider as the UV emission is distributed over the disc,

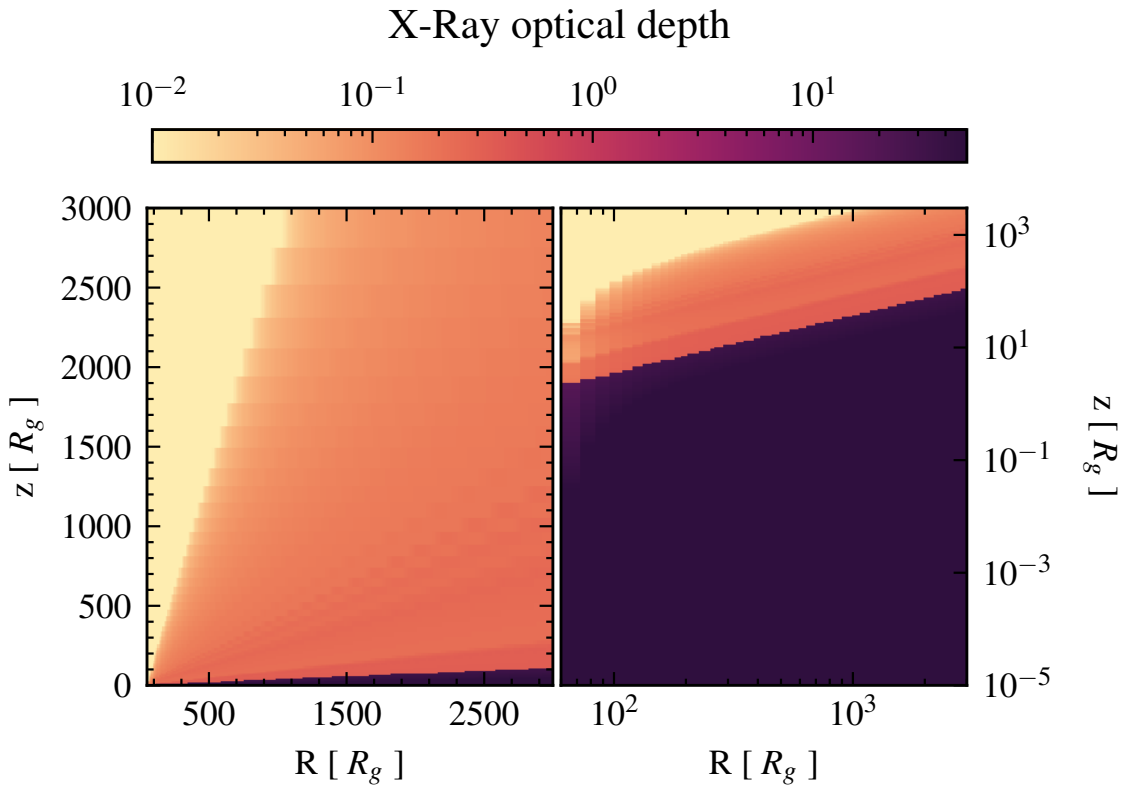

Figure 4.11: X-ray optical depth as a function of position, measured from $R = 0$ and $z = 0$. Left panel: position in linear scale. Right panel: position in logarithmic scale.

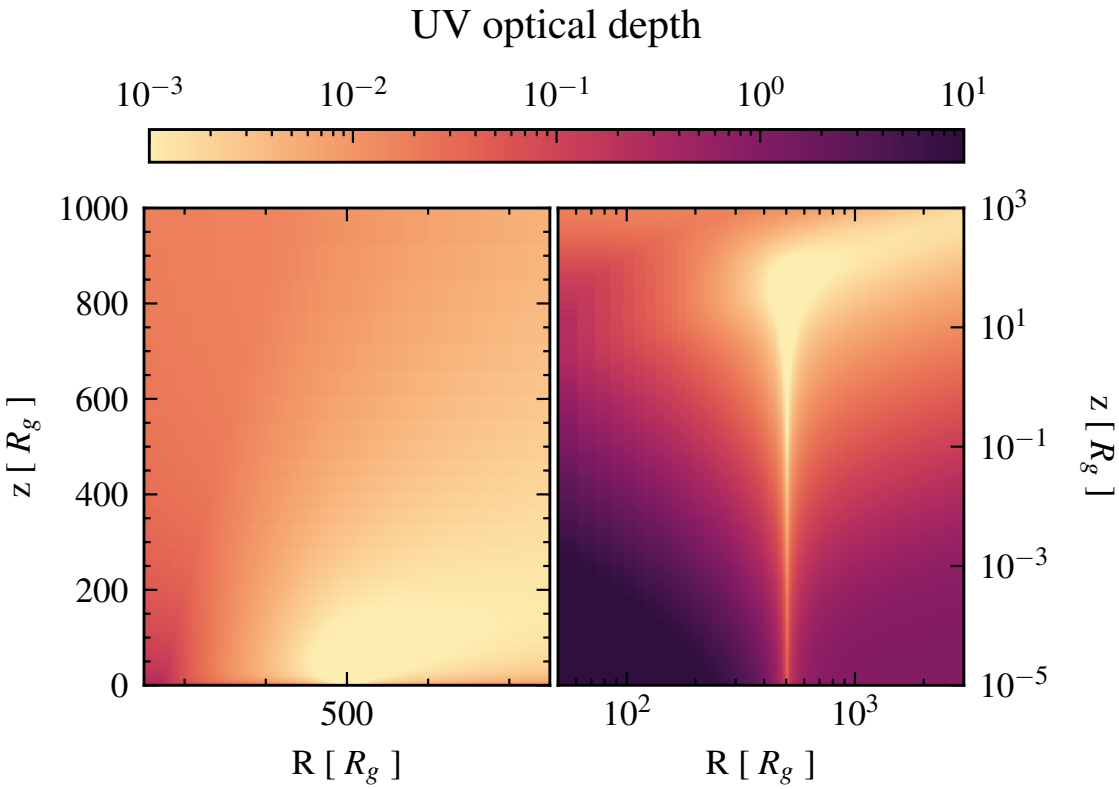

Figure 4.12: UV optical depth as a function of position, measured from $R = 500R_g$ and $z = 0$. Left panel: position in linear scale. Right panel: position in logarithmic scale.

making this ray tracing calculation the highest contributor to the computational cost of the model. The total UV flux and its resultant direction at any given position in the wind have to be calculated as the sum over each disc element (see equation 3.2.5) where now $\tau_{\rm UV} = \tau_{\rm UV}(R_d, \phi_d, R, z)$.

As already noted in Q20, the integral in equation 3.2.15 is challenging to calculate numerically, and in this case the computational cost is further increased by the refined UV ray tracing. In spite of that, by using the adaptive integration scheme presented in Berntsen et al. (1991) and implemented in Johnson (2021), the integration typically converges after $\mathcal{O}(10^4)$ integrand evaluations, which results in a computation time of a few milliseconds, keeping the simulation tractable. At low heights, $z \sim 0$, the trajectory solver requires several evaluations of the radiation force to correctly compute the adaptive time-step, which makes the computation particularly slow. Fortunately, the approximation in equation 4.3.12 comes in very handy at reducing the overall computational cost at low heights.

4.5 Special relativity effects

When the gas trajectory approaches the speed of light, one should consider special relativistic effects such as relativistic beaming and Doppler shifting (see eg Rybicki & Lightman, 1986, chapter 4). The importance of taking these effects into account is highlighted in Luminari et al. (2020). We include a correction to the radiation flux seen by the gas (equation 3.2.5),

$$\mathrm{d}F_{\mathrm{relativistic}} = \Psi(R_d, \phi_d, R, z, v_R, v_z)\ \mathrm{d}F, \tag{4.5.1}$$

where v_R and v_z are the radial and vertical velocity components of the gas at the position $(R, 0, z)$. We ignore the contribution from the angular velocity component, v_ϕ for simplicity, as its inclusion would break our assumption that angular momentum is conserved along a gas blob trajectory. The correction Ψ is given by (Luminari et al., 2021),

$$\Psi = \frac{1}{\gamma^4(1+\beta\cos\theta)^4}, \tag{4.5.2}$$

where γ is the Lorentz factor, $\beta = \sqrt{v_R^2 + v_z^2}/c$, and θ is the angle between the incoming light ray and the gas trajectory,

$$\cos\theta = \frac{(R - R_d\cos\phi_d)v_R + zv_z}{\beta\Delta}. \tag{4.5.3}$$

Intuitively, when the incoming light ray is parallel to the gas trajectory, $\cos\theta = 1$, so the correction reduces to $\Psi = \left(\frac{1-\beta}{1+\beta}\right)^2$, which is 0 when $\beta = 1$ and 1 when $\beta = 0$, as expected.

It is worth noting that this is a local correction which needs to be integrated along all the UV sight-lines (see equation 3.2.15). Nonetheless, the computational cost of calculating the radiation force is heavily dominated by ray tracing and the corresponding UV optical depth calculation, so this relativistic correction does not significantly increase the computation time.

The X-ray flux, which determines the ionisation state of the gas, is also likewise corrected for these special relativistic effects, but there is only one such sight-line to integrate along for any position in the wind, as the X-ray source is assumed to be point-like.

4.6 Calculating the gas trajectories

4.6.1 Initial radii of gas trajectories

The first thing to consider when calculating the gas trajectories is the initial location of the gas blobs. Here we describe an improved method on how to sample the initial trajectori radii

compared to Q20, which also takes into account the change in optical depth at the wind base. The innermost initial position of the trajectories is taken as a free parameter $R_{\rm in}$, and the outermost initial position, $R_{\rm out}$, is assumed to be the self-gravity radius of the disc, where the disc is expected to end (Laor & Netzer, 1989), which for our reference BH corresponds to 1580 R_g. We initialise the first trajectory at $R_{\rm in}$, the next trajectory starts at $R = R_{\rm in} + \Delta R$, where ΔR is the distance between adjacent trajectories. We determine ΔR by considering two quantities: (i) the change in optical depth between two adjacent trajectories along the base of the wind and (ii) the mass loss rate along a trajectory starting at R and at a distance ΔR to the next one. Regarding (i), the change in optical depth $\Delta\tau$ between two trajectories initially separated by ΔR is given by

$$\Delta\tau = \int_{R}^{R+\Delta R_1} n(R')\,\sigma_{\rm T}\,{\rm d}R'. \tag{4.6.1}$$

We consider

$$\Delta\tau = \begin{cases} 0.05 & \text{if } \tau(R) < 5, \\ 0.5 & \text{if } \tau(R) < 10, \\ 5 & \text{if } \tau(R) < 100, \\ 20 & \text{if } \tau(R) > 100, \end{cases} \tag{4.6.2}$$

where $\tau(R) = \sum_i \Delta\tau_i$. This guarantees that the spacing between trajectories resolves the transition from optically thin to optically thick for both the UV and X-ray radiation. The quantity (ii) is given by

$$\Delta\dot{M}_{\rm wind} = \int_{R}^{R+\Delta R_2} 2\pi R'\rho(R')v(R'){\rm d}R', \tag{4.6.3}$$

where we consider $\Delta\dot{M}_{\rm wind} = 0.01\dot{M}$, so that no streamline represents more than 1% of the accreted mass rate. The ΔR step is thus given by

$$\Delta R = \min(\Delta R_1, \Delta R_2) \tag{4.6.4}$$

and we repeat this process until $R = R_{\rm out}$

4.6.2 Solving the equation of motion

The equation of motion of the wind trajectories is the same as in Q20, and we solve it analogously by using the Sundials IDA integrator (Hindmarsh et al., 2005). The wind trajectories are calculated until they either exceed a distance from the centre of $10^4 R_g$, fall back to the disc, or self intersect. To detect when a trajectory self intersects we use the algorithm detailed

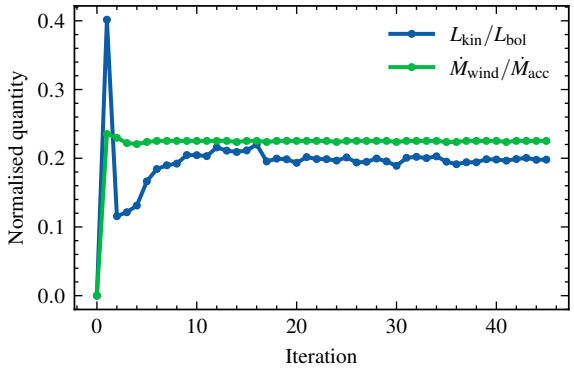

Figure 4.13: Normalised mass loss rate and kinetic luminosity for each iteration for our fiducial case.

in Appendix 4.6.3.

By considering the full wind structure for the radiation ray tracing, we run into an added difficulty: the interdependence of the equation of motion with the density field of the wind. To circumvent this, we adopt an iterative procedure in which the density field of the previous iteration is used to compute the optical depth factors for the current iteration. We first start assuming that the disc's atmosphere is void, with a vacuum density of $n_{\rm vac} = 10^2$ cm^{-3}. Under no shielding of the X-ray radiation, all the trajectories fall back to the disc in a parabolic motion. After this first iteration, we calculate the density field of the resulting failed wind and use it to calculate the wind trajectories again, only that this time the disc atmosphere is not void. We keep iterating until the mass loss rate and kinetic luminosity do not significantly change between iterations. It is convenient to average the density field in logarithmic space between iterations, that is, the density field considered for iteration k, n_k, is given by

$$\log_{10}(n_k(R,z)) = \frac{1}{2}\left(\log_{10}(n_{k-1}(R,z)) + \log_{10}(n_{k-2}(R,z))\right). \tag{4.6.5}$$

We do not take the average for the first two iterations. The number of iterations required depends on the initial radius of the wind, but we typically find convergence after $\sim$ 20 iterations, although we run several more to ensure that the standard deviation of the density field between iterations is small. The normalised mass loss rate and kinetic luminosity for our fiducial model at each iteration are shown in Figure 4.13.

For a given iteration, solving the equation of motion for the different gas trajectories is an embarrassingly parallel problem, and so our code's performance scales very well upon using multiple CPUs, allowing us to quickly run multiple iterations, and scan the relevant parameter spaces. The computational cost of running one iteration is $\sim$ 5 CPU hours, so one is able to

obtain a fully defined wind simulation after ~ 100 CPU hours. The total cost is reduced to ~ 1 CPU hour when the calculation of $\tau_{\rm UV}$ is switched off (so assuming $\tau_{\rm UV} = 0$), or when the calculation of $\tau_{\rm UV}$ is done from the centre of the grid as in the previous versions of QWIND.

4.6.3 Intersection of trajectories

Once we have solved the equations of motion of the different gas blobs, it is common for the resulting trajectories to cross each other. Trajectories of gas elements computed using our ballistic model should not be confused with the streamlines of the actual wind fluid, since the latter cannot cross each other as it would imply the presence of singular points where the density and the velocity fields are not well defined.

Nonetheless, if we aim to construct a density and velocity field of the wind, we need to define the density and velocity at the crossing points. To circumvent this, once two trajectories intersect, we terminate the one that has the lowest momentum density at the intersection point.

To determine at which, if any, point two trajectories cross, we consider a trajectory as a collection of line segments $\{s_i\}$. Two trajectories $\{s_i\}$, and $\{t_j\}$ cross each other if it exists i, j such that $s_i \cap t_j \neq 0$.

Suppose the line segment s_i is bounded by the points $\boldsymbol{p_1}$ and $\boldsymbol{p_2}$ such that $\boldsymbol{p_2} = \boldsymbol{p_1} + \alpha'(\boldsymbol{p_2} - \boldsymbol{p_1})$ with $\alpha' \in [0, 1]$. Similarly, t_j is limited by $\boldsymbol{q_1}$ and $\boldsymbol{q_2}$ such that $\boldsymbol{q_2} = \beta'(\boldsymbol{q_2} - \boldsymbol{q_1})$ with $\beta' \in [0, 1]$. The condition that s_i intersects t_j is equivalent to finding α, $\beta \in [0, 1] \times [0, 1]$ such that

$$\boldsymbol{p_1} + \alpha'(\boldsymbol{p_2} - \boldsymbol{p_1}) = \boldsymbol{q_1} + \beta'(\boldsymbol{q_2} - \boldsymbol{q_1}), \tag{4.6.6}$$

which corresponds to the linear system $\boldsymbol{A}\boldsymbol{x} = \boldsymbol{b}$ with

$$\boldsymbol{A} = (\boldsymbol{p_2} - \boldsymbol{p_1}, \boldsymbol{q_1} - \boldsymbol{q_2}), \tag{4.6.7}$$

$\boldsymbol{x} = (\alpha', \beta')^\intercal$, and $\boldsymbol{b} = \boldsymbol{q_1} - \boldsymbol{p_1}$. The segments intersect if this linear system is determined with solution inside the unit square.

Terminating the gas blob trajectories effectively means that mass conservation is not satisfied in the wind. This may be an issue if we are terminating gas trajectories that would otherwise escape, since we would be then underestimating the outflow power. Nonetheless, we have checked that for the systems examined in this work, the unaccounted mass rate is less than 5% of the total wind mass rate, so it does not significantly impact our results. Nonetheless,

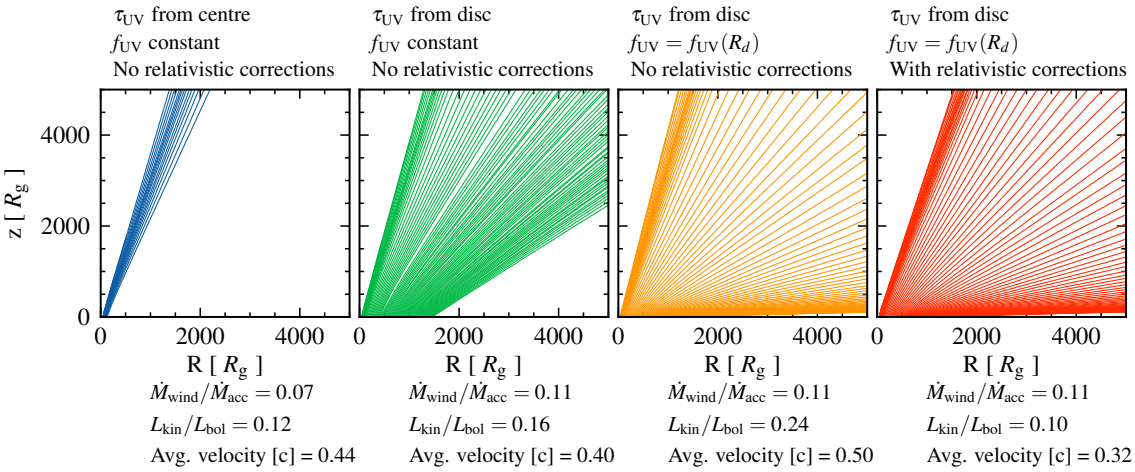

Figure 4.14: Effects of our improvements to the treatment of the radiation field on the trajectories of gas blobs. All simulations have been done with $M_{\rm BH} = 10^8 {\rm M}_\odot$, $\dot{m} = 0.5$, and $R_{\rm in} = 50 R_{\rm g}$.

a possible workaround would be to allow trajectories to merge when they intersect as it is done in Ogata et al. (2021).

4.7 Effects of the code improvements on the wind

In this section, we evaluate the effect on the wind of the three improvements that we presented to the treatment of the radiation field: (i) radial dependence of $f_{\rm UV}$, (ii) improved radiation transport, and (iii) relativistic corrections. The impact of each improvement is shown in Figure 4.14. In the first panel (blue), we calculate the optical depth $\tau_{\rm UV}$ from the centre, rather than attenuating each individual light ray coming from the disc. We also take a constant $f_{\rm UV} = 0.85$ and we do not include relativistic corrections. Calculating $\tau_{\rm UV}$ from the centre overestimates the attenuation of the UV radiation field in the outer parts of the wind, since it assumes that the radiation is crossing all the inner gas. This produces a failed wind in the outer regions of the disc (which is on too small a scale to be seen in Figure 4.14), since the inner gas is optically thick to the UV radiation. In the next panel (green), we calculate $\tau_{\rm UV}$ by attenuating each individual light ray as explained in section 4.4, consequently, most of the wind escapes from the disc since the UV attenuation is less strong, with the average wind velocity being slightly lower because we are now averaging over the slower trajectories in the outer part of the wind. The next improvement we evaluate is the inclusion of the radial dependence of $f_{\rm UV}$ (third panel, orange). The change in wind geometry can be explained by considering the distribution of the UV emissivity, which is skewed towards the centre of

the disc thus pushing the outer wind along the equator. This also leads to a more powerful wind, due to the increase in UV luminosity at small radii, where the fastest and most massive streamlines originate. Lastly, the effect of including relativistic corrections is shown in the 4th panel (red). As expected, the velocity of the wind is considerably lower, and hence also its kinetic luminosity. Furthermore, the wind flows at a slightly higher polar angle, as the vertical component of the radiation force gets weaker where the wind has a high vertical velocity.

4.8 Comparison to hydrodynamical simulations

The QWIND framework is based on the idea that in the context of a line-driven wind, the gas pressure forces can be ignored, except in the launching phase, which is calculated separately by integrating the 1D hydro equations including both gas pressure and radiation pressure (see section 4.3). This is verified in the Appendix of Nomura et al. (2016), where the authors determine that the radiation and centrifugal forces are the main drivers of the wind velocity field away from the disk surface from where the wind is launched. Therefore, we expect the QWIND approach to produce comparable results to the more expensive radiation-hydrodynamic (RHD) simulations.

We compare our results with P04, who assume no UV attenuation ($\tau_{\rm UV} = 0$), and X-ray attenuation only by electron scattering ($\sigma_{\rm X} = \sigma_{\rm T}$), which allows for a simpler comparison. Following the simulation setup described in P04, we run a QWIND simulation with the parameters described in Table 4.1. We note that with the presented derivation of the initial conditions of the wind in section 4.3, the QWIND model has the same number of free parameters as the RHD simulation of P04 and no extra parameters are used to adjust the results.

The QWIND approach can only calculate steady state solutions, while RHD simulations are time dependent. Hence, the wind properties at the simulation boundary may not necessarily agree at a single tiem and a time-averaged comparison of the P04 results would be more appropriate. Nonetheless, we expect that the global properties of the wind such as the mass loss rate and kinetic luminosity do not change significantly over time. P04 report an integrated mass-loss rate of $\dot{M}_{\rm wind} \simeq 1.36 \times 10^{25}$ g s^{-1}, while we find a very similar value of $\dot{M}_{\rm wind} \simeq 1.34 \times 10^{25}$ g s^{-1}. Similarly, we have used the reported P04 velocity profile of their Figure 2 to compute the total kinetic luminosity of the wind, which we calculate to be

Parameter	Value
$M_{\rm BH}$ / $\rm M_\odot$	10^8
$\dot{m}$	0.5
$f_{\rm UV}$	0.9
$f_{\rm X}$	0.1
z_0 / $R_{\rm g}$	1.5
$\sigma_{\rm UV}$	0
$\sigma_{\rm X}$	$\sigma_{\rm T}$
$R_{\rm in}$ / $R_{\rm g}$	60
v_0	$v_{\rm th}$
n_0	CAK derivation

Table 4.1: Input QWIND parameters for the simulation run comparing QWIND with P04.

$L_{\rm wind} \simeq 1.96 \times 10^{43}$ g cm^2 s^{-3}, and we find again a comparable result, $L_{\rm wind} \simeq 1.48 \times 10^{43}$ g cm^2 s^{-3}. The momentum rate of the wind differs by a bit more; we calculate the P04's simulated wind momentum rate to be $\dot{p}_{\rm wind} \simeq 3.26 \times 10^{34}$ g cm s^{-2}, while with QWIND3 we obtain $\dot{p}_{\rm wind} \simeq 1.69 \times 10^{34}$ g cm s^{-2}.

We conclude that QWIND is able to give comparable results to other more computationally expensive RHD simulation codes, at a much lower computational cost. In particular, the presented simulation in this section took $\simeq 1$ CPU hour to run, since we are not considering the full radiation transfer calculation involved in calculating $\tau_{\rm UV}$. QWIND can then be used as a complementary tool to explore the BH parameter space in an efficient way, as we show in the next sections.

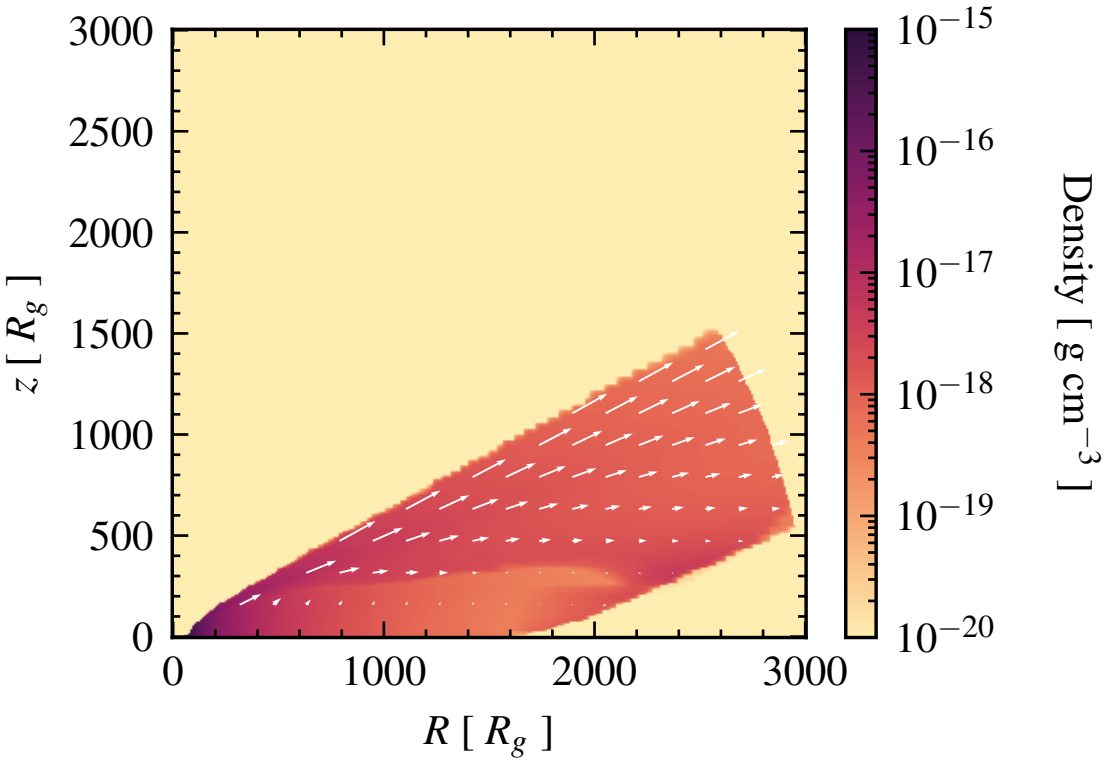

Figure 4.15: Wind density (colour-coded) and velocity (plotted as arrows) of the QWIND simulation run with the same parameters as P04 (Table 4.1)

Chapter 5

Dependence of UV line-driven wind properties on BH parameters

Here, we evaluate the dependence of the wind properties on the initial wind radius, BH mass, and mass accretion rate. We also study the impact of the relativistic corrections on the wind velocity and structure. All of the parameters that are not varied are specified in Table 5.1.

5.1 The fiducial case

To gain some intuition about the structure of the wind trajectories solutions, we first have a close look at our fiducial simulation with $M_{\rm BH} = 10^8\,{\rm M}_\odot$, $\dot{m} = 0.5$, and $R_{\rm in} = 50\,R_{\rm g}$. We run the simulation iterating 50 times through the density field, to make sure that our density grid has converged (see subsection 4.4.1).

In Figure 5.1, we plot the wind streamline shapes, zooming in on the innermost region where we also show the ionisation state of the gas. Figure 4.5 shows that the initial density should be

Parameter	Value
$f_{\rm X}$	0.15
z_0	0
$R_{\rm out}/R_{\rm g}$	1580
μ	0.61
μ_e	1.17
α	0.6
$k_{\rm ic}$	0.03

Table 5.1: Fixed parameters for the results section. Note that $k_{\rm ic}$ refers to the value of k used to compute the initial conditions of the wind (equation 4.3.8), but we use the SK90 parametrisation $k = k(\xi)$ elsewhere.

$\sim 3 \times 10^{12}$ cm^{-3}. Hence the initial ionisation parameter at $R_{\rm in}$ is $\xi = f_{\rm X}\, 0.5\, L_{\rm Edd}/(n_{\rm in} R_{\rm in}^2) \sim$ 800 so the base of the wind is already in the regime where the X-ray opacity is high. The wind starts, but the drop in density as the material accelerates means it reaches a high ionisation parameter where the force multiplier is low before it reaches escape velocity. Hence the material falls back to the disc as a failed wind region.

The failed wind region has a size characterised by $\tau_x \lesssim 5$, acting as a shield to the outer wind from the central X-ray source. The X-ray obscuration is especially large in the failed wind shadow, due to the jump in X-ray opacity at $\xi_0 = 10^5$ erg cm s^{-1} (see contour shown by turquoise line in the left panel of Figure 5.1), but its opening angle may be small (Figure 4.11). The shadow region defines the acceleration region of the wind, where the force multiplier is greatly enhanced and the wind gets almost all of its acceleration. Eventually this acceleration is enough that the material reaches the escape velocity before it emerges from the shadow, and is overionised by the X-ray radiation. The left panel of Fig. 5.1 shows these first escaping streamlines (blue) which are close to $R_{\rm in}$.

Figure 5.2 shows the resulting wind parameters at a distance $r = 5000\, R_{\rm g}$. We plot the wind column density, and density-weighted mean velocity and ionisation parameter as a function of the polar angle $\theta = \arctan(R/z)$. The column is almost constant at $N_H \sim 2 \times 10^{23}$ cm^{-2} (optical depth of ~ 0.1 to electron scattering) across the range $25° < \theta < 85°$. For $\theta > 85°$, the sight-line intercepts the inner failed wind and the column density increases to $N_H \sim 10^{24}$ cm^{-2}. The typical wind velocity at this point is $\simeq (0.1 - 0.4)\, c$ but it is always very ionised ($\xi > 10^5$ erg cm s $^{-1}$) at these large distances. This is too ionised to allow even H- and He-like iron to give visible atomic features in this high velocity gas, although these species may exist at smaller radii where the material is denser. We will explore the observational impact of this in a future work, specifically assessing whether UV line-driving can be the origin of the ultra-fast outflows seen in some AGN (see also Mizumoto et al. 2021).

The escaping wind carries a mass loss rate of $\dot{M}_{\rm wind} \simeq 0.52$ M$_\odot$/ yr, corresponding to $\dot{M}_{\rm wind}/\dot{M} \simeq 22\%$ of the mass accretion rate, and a kinetic luminosity of $L_{\rm kin} \approx 1.4 \times 10^{45}$ erg / s, which is equal to 20% of the bolometric luminosity. As the two bottom panels of Figure 5.2 show, most of the energy and momentum of the wind is located at small polar angles ($\sim 20°$), which is consistent with the initial density profile since the innermost streamlines carry the largest amount of mass.

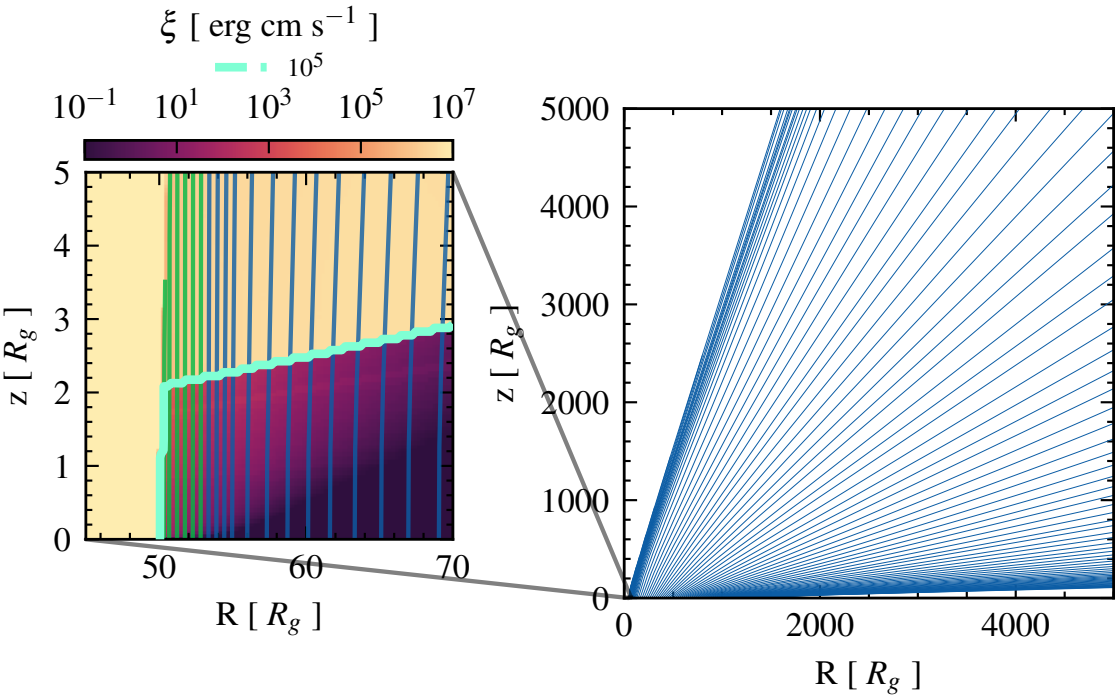

Figure 5.1: Simulated wind trajectories for our fiducial system ($M_{\rm BH} = 10^8 {\rm M}_\odot$, $\dot{m} = 0.5$, and $R_{\rm in} = 50 R_{\rm g}$) zooming in on the failed wind region, where we also colour-plot the ionisation parameter ξ, showing the contour at $\xi = 10^5$ erg cm s^{-1} as the light turquoise line. We plot the failed trajectories in green and the escaping trajectories in blue.

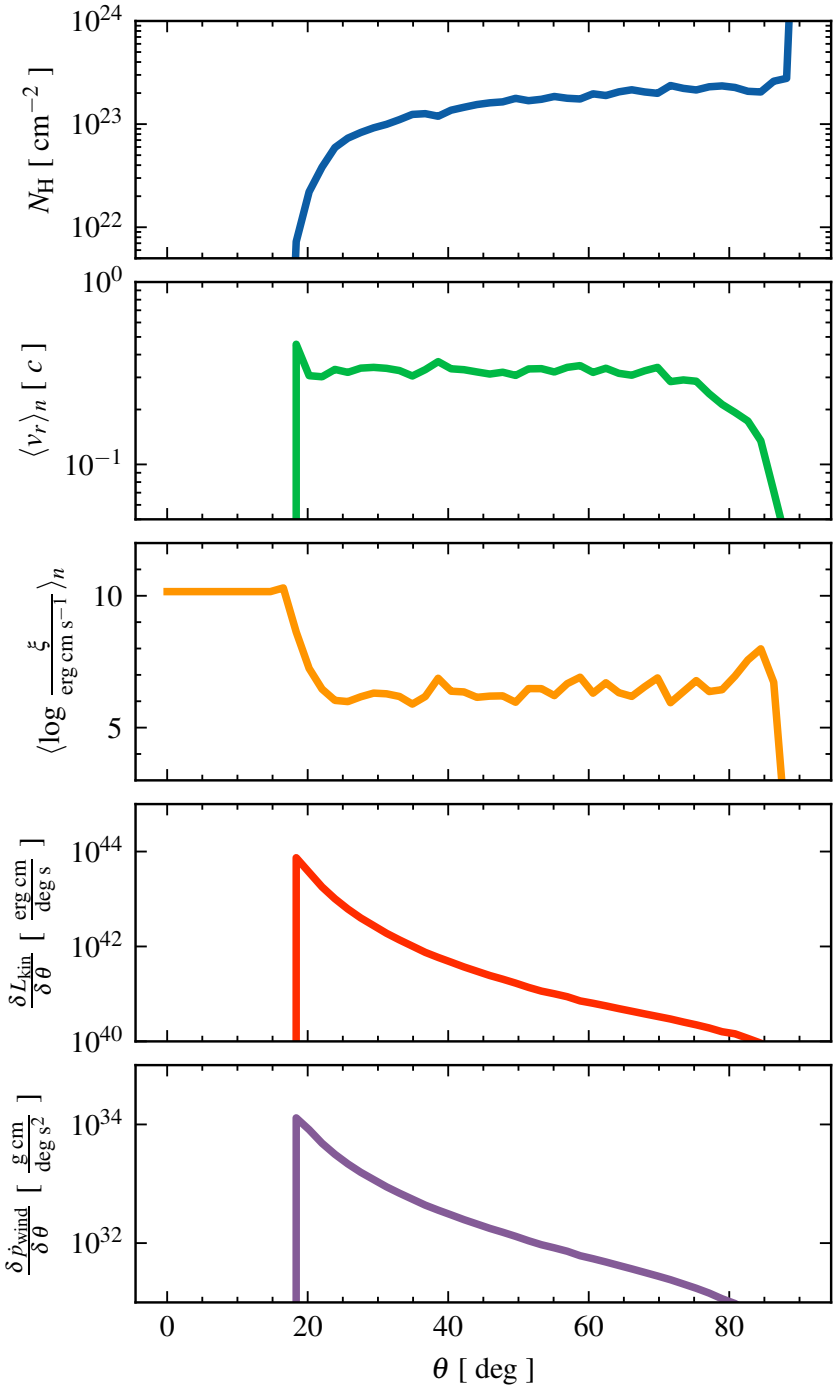

Figure 5.2: Wind properties for a system with $M_{\rm BH} = 10^8 {\rm M}_\odot$, $\dot{m} = 0.5$, $R_{\rm in} = 50 R_{\rm g}$ measured along a sight-line at angle θ at a distance $r = 5000 R_{\rm g}$ from the centre. First panel: column density. Second panel: outward mean velocity weighted by density. Third panel: mean ionisation parameter weighted by density. Fourth panel: kinetic luminosity per unit angle. Fifth panel: wind momentum rate per unit angle.

5.1.1 Verification of the critical point conditions

For our fiducial case, we plot the critical point location compared to the wind trajectories in Figure 5.3. All escaping trajectories are vertical at the critical point, so our treatment of the wind as a 1D flow for the initial conditions derivation is justified. Nonetheless, we emphasise again that this treatment does not hold for the inner failed wind. The wind is highly supersonic (10^3 times the sound speed) at the critical point, as shown in the bottom panel of Figure 5.3, so our assumption $w \gg s$ is validated.

5.2 Dependence on the initial radius $R_{\rm in}$

As we already mentioned in section 4.6, the initial radius of the innermost trajectory ($R_{\rm in}$) is left as a free parameter to explore. This parameter is likely dependent on the structure of the accretion flow, which we do not aim to model here. As we increase $R_{\rm in}$, the amount of mass that can potentially be lifted from the disc decreases, both because of the reduction in the extent of the launching region and the decrease in initial density with radius (Figure 4.5). Furthermore, increasing $R_{\rm in}$ also narrows the failed wind shadow, since it reduces its subtended angle, thus reducing the accelerating region of the wind. We therefore expect the wind to flow at higher polar angles and smaller velocities when increasing $R_{\rm in}$. In Figure 5.4, we plot the predicted normalised mass loss rate, kinetic luminosity, momentum loss rate, and average velocity of the wind as a function of $R_{\rm in}$. As we expected, both the mass loss rate and the kinetic luminosity decrease with $R_{\rm in}$, with the latter decreasing much faster. This difference in scaling is not surprising, since the fastest part of the wind originates from the innermost part of the disc, where most of the UV radiation is emitted. To further illustrate this, we plot the average velocity of the wind for each simulation in the rightmost panel of Figure 5.4, observing that the maximum velocity decreases with initial radius. We note that the wind successfully escapes for $R_{\rm in} \gtrsim 175 R_{\rm g}$, which is a consequence of the initial number density profile (Figure 4.5) sharply declining after $R \gtrsim 100 R_{\rm g}$. There is a physically interesting situation happening at $R_{\rm in} \sim 12 R_{\rm g}$, where the average velocity of the wind drops. This is due to the failed wind being located where most of the UV emission is, thus making the wind optically thick to UV radiation (with respect to electron scattering opacity). Lastly, we note that the wind consistently reaches velocities $\gtrapprox 0.3\ c$ for $R_{\rm in} \lesssim 50\, R_{\rm g}$.

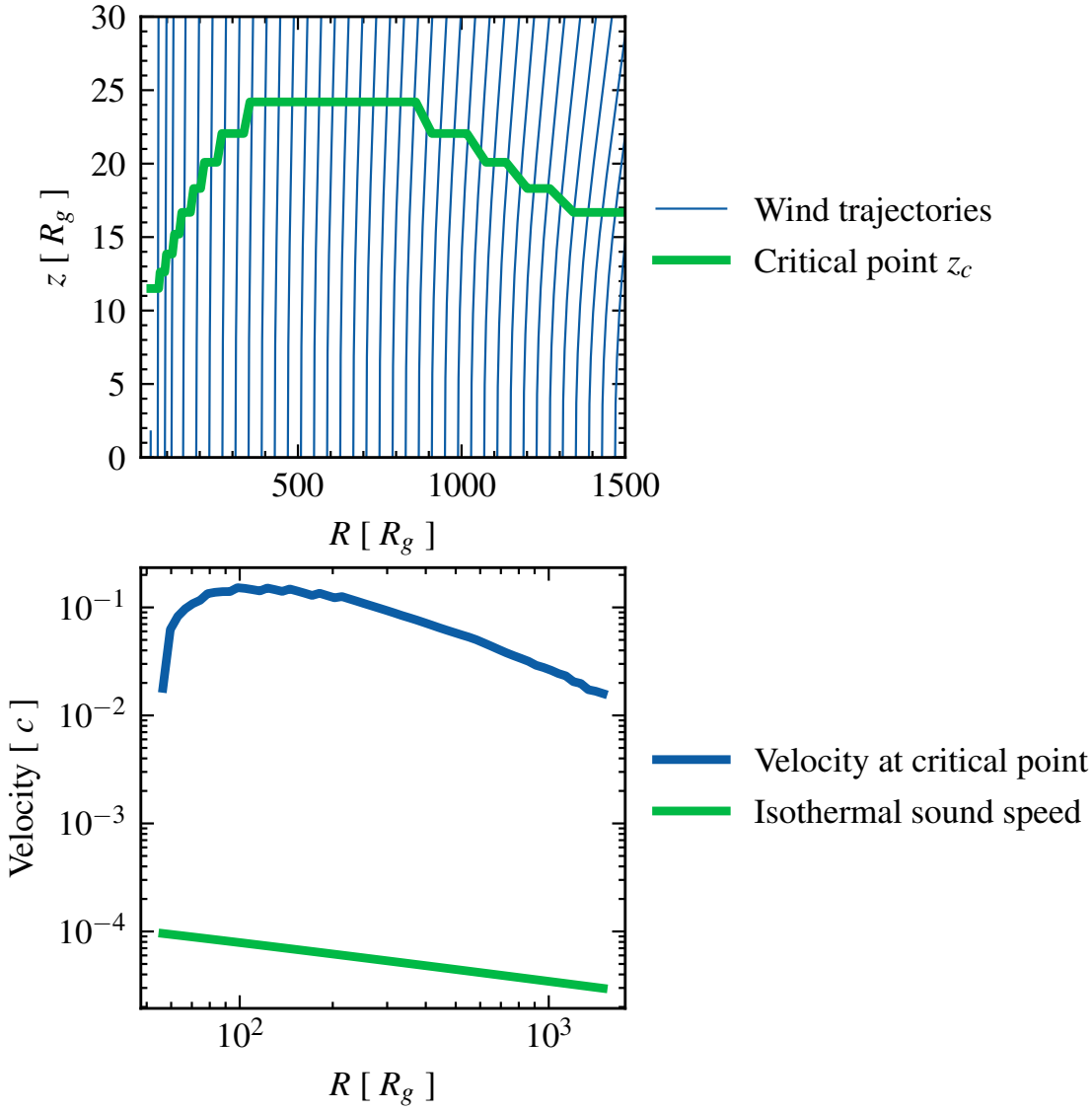

Figure 5.3: Results for fiducial case $M_{\rm BH} = 10^8 {\rm M}_\odot$ and $\dot{m} = 0.5$. Top panel: wind trajectories compared to the critical point position, plotted on a linear scale. Bottom panel: Velocity at the critical point plotted on a log scale

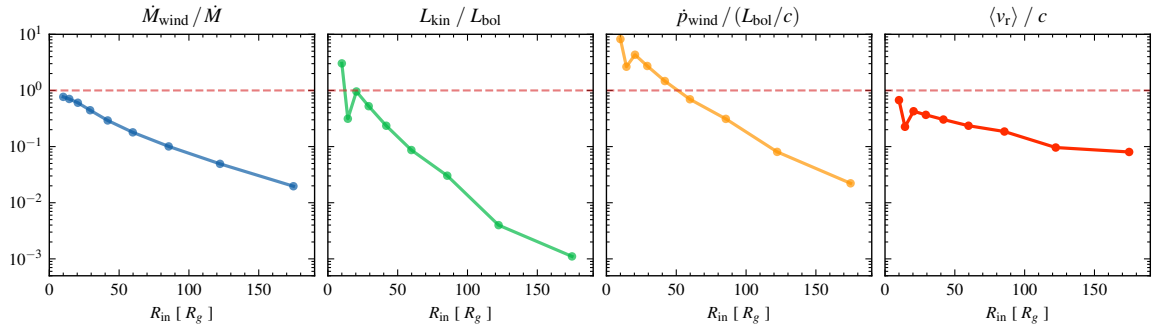

Figure 5.4: Mass loss rate (first panel), kinetic luminosity (second panel), momentum loss rate (third panel) and average velocity (fourth panel) for different values of $R_{\rm in}$, at a fixed $M_{\rm BH} = 10^8 {\rm M}_\odot$ and $\dot{m} = 0.5$. The mass loss rate is normalised to the system's mass accretion rate, while we normalise the luminosity to the bolometric luminosity. The average velocity is taken as $v_{\rm r} = \sqrt{2L_{\rm kin}/\dot{M}_{\rm wind}}$.

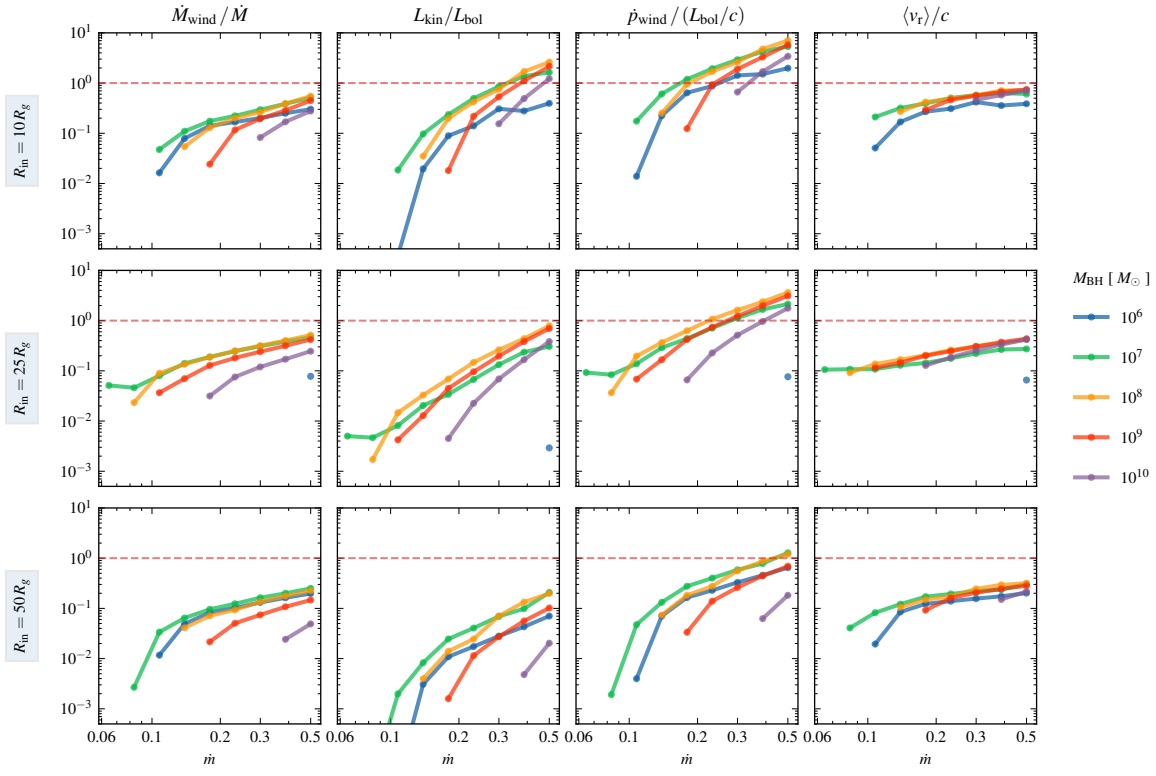

Figure 5.5: Wind mass loss rate normalised by the mass accretion rate (first panel column), kinetic luminosity normalised by bolometric luminosity (second panel column), momentum loss rate normalised by $L_{\rm bol}/c$ (third panel column), and average velocity (fourth panel column) as functions of the Eddington fraction $\dot{m}$ for different $M_{\rm BH}$.The average velocity is taken as $v_{\rm r} = \sqrt{2L_{\rm kin}/\dot{M}_{\rm wind}}$.

5.3 Dependence on BH mass and mass accretion rate

We now investigate the dependence of the wind mass loss rate, kinetic luminosity, momentum loss rate, and average velocity on $M_{\rm BH}$, $\dot{m}$, and $R_{\rm in}$. We scan the BH parameter range for $M_{\rm BH} \in (10^6 - 10^{10})$, $\dot{m} \in (0.01 - 0.5)$, and $R_{\rm in} = (10, 25, 50)R_{\rm g}$. We fix $f_{\rm X} = 0.15$ and recognise that keeping it constant throughout the parameter scan is a limitation, since in reality it depends on $M_{\rm BH}$ and $\dot{m}$. The results are shown in Figure 5.5, where all of the quantities have been normalised to their characteristic scales. The red dashed line denotes the limit when quantities become unphysical since the wind is carrying more mass, energy, or momentum than the disc can provide. The first thing to note is that we do not obtain any wind for $\dot{m} \lesssim 0.06$, regardless of $M_{\rm BH}$. This is initially surprising, as the force multiplier is of order 1000 for cool material, apparently allowing a wind to escape for $\dot{m} > 0.001$. However, the initial density drops as $\dot{m}^{1/\alpha}$ (see subsection 4.3.2) so the X-ray shielding drops dramatically, strongly suppressing the wind. Overall, the weakest winds are seen from the highest ($M_{\rm BH} = 10^{10}\,{\rm M}_\odot$) and lowest ($M_{\rm BH} = 10^{6}\,{\rm M}_\odot$) black hole masses. This can be explained by the behaviour of the UV fraction (Figure 4.1). For the $M_{\rm BH} = 10^{6}\,{\rm M}_\odot$ case, the UV bright disc annuli are located at large radii, where the disc luminosity is lower; for the $M = 10^{10}{\rm M}_\odot$ case, $f_{\rm UV}$ is only high at very small radii, and overall small in the wind launching region. Furthermore, the high disc temperatures expected for the lowest mass systems ($M_{\rm BH} = 10^{6}\,{\rm M}_\odot$), especially at high $\dot{m}$, mean that the disc contributes to the ionising X-ray flux. This effect is not considered in our work here, but makes it likely that even our rather weak UV line-driven wind is an overestimate for these systems.

For the values of $M_{\rm BH}$ where the wind is robustly generated across the rest of the parameter space, $M_{\rm BH} \in (10^7, 10^8, 10^9){\rm M}_\odot$, we find a weak dependence of the normalised wind properties on $M_{\rm BH}$. This is expected, since the initial density profile scales with $M_{\rm BH}$ and $\dot{m}$ as (subsection 4.3.2)

$$n_0 \propto \frac{\dot{m}^{\frac{1}{\alpha}}}{M_{\rm BH}}, \tag{5.3.1}$$

where we ignore the dependence of $f_{\rm UV}$ on $M_{\rm BH}$. The initial wind velocity $v_0 = v_{\rm th} \propto T^{1/2}$, hence

$$v_0 \propto \left(\frac{\dot{m}}{M_{\rm BH}}\right)^{1/8} \tag{5.3.2}$$

(see equation 3.2.5.) This then implies

$$\dot{M}_{\rm wind} \propto n_0\, v_0\, R^2 \propto \left(\frac{\dot{m}^{\frac{1}{\alpha}}}{M_{\rm BH}}\right)\left(\frac{\dot{m}}{M_{\rm BH}}\right)^{1/8}\left(M_{\rm BH}^2\right) \tag{5.3.3}$$

Since scaling due to the dependence on v_0 is particularly weak (it depends on the 1/8-th power), we choose to ignore it so that we can write

$$\frac{\dot{M}_{\rm wind}}{\dot{M}_{\rm acc}} \propto \frac{\dot{m}^{\frac{1}{\alpha}} M_{\rm BH}}{\dot{m} M_{\rm BH}} \propto \dot{m}^{\frac{1}{\alpha}-1}, \tag{5.3.4}$$

where we have used the fact that $\dot{M}_{\rm acc} = \dot{m}\dot{M}_{\rm Edd} \propto \dot{m} M_{\rm BH}$. Similarly,

$$\frac{L_{\rm kin}}{L_{\rm bol}} \propto \frac{\dot{M}_{\rm wind} v_f^2}{\dot{M}_{\rm acc}} = \dot{m}^{1+\frac{1}{\alpha}}, \tag{5.3.5}$$

where v_f is the final wind velocity and we have assumed $v_f \propto \dot{m}$. This last assumption is verified (for $0.1 \lesssim \dot{m} \lesssim 0.5$) in the rightmost panel of Figure 5.5. Consequently, ignoring the scaling of $f_{\rm UV}$, both the normalised mass loss rate and normalised kinetic luminosity are independent of $M_{\rm BH}$. For our value of $\alpha = 0.6$, we find $L_{\rm kin} \propto \dot{m}^{2.7} L_{\rm bol}$. This scaling is significantly different from the one often assumed in models of AGN feedback used in cosmological simulations of galaxy formation, where the energy injection rate is assumed to be proportional to the mass accretion rate and hence to the bolometric luminosity (Schaye et al., 2015; Weinberger et al., 2017; Davé et al., 2019b). However, it is consistent with the results found in the hydrodynamical simulations of Nomura & Ohsuga (2017) and with current observational constraints (Gofford et al., 2015; Chartas et al., 2021).

For the $R_{\rm in} = 10R_{\rm g}$ case, many parameter configurations of $M_{\rm BH}$ and $\dot{m}$ give rise to winds that are unphysical, since they carry more momentum than the radiation field, and have a kinetic luminosity higher than the bolometric luminosity. This is caused by us not considering the impact that the wind mass loss would have on the disc SED, and an underestimation of the UV opacity in our ray tracing calculation of the UV radiation field, in which we only include the Thomson opacity. We also observe that for the lower and upper ends of our $M_{\rm BH}$ range the existence of a wind for different $\dot{m}$ values depends on the value of $R_{\rm in}$. This is a consequence of a complex dependence of the failed wind shadow on the initial density and $R_{\rm in}$.

We now investigate the geometry of the wind: where it originates and at which angles it flows outwards. Despite the strong dependence of the kinetic luminosity on $\dot{m}$, the wind launching region does not vary significantly with $\dot{m}$, as is shown in Figure 5.6, where we plot the average launch radius, weighted by mass loss rate or kinetic luminosity. The exception is the case $R_{\rm in} = 10R_{\rm g}$, where the lower inner density at $R_{\rm in} = 10R_{\rm g}$ (see Figure 4.5), and its decrease with $\dot{m}$ produce a larger failed wind region for $\dot{m} \lesssim 0.15$. The dependence of the mass weighted average radius with $M_{\rm BH}$ is a consequence of the dependence of $f_{\rm UV}$ on

$M_{\rm BH}$. Larger $M_{\rm BH}$ black holes have the $f_{\rm UV}$ peak closer in, so the wind carries more mass at smaller radii.

Finally, we plot the wind opening angle for the scanned parameter space in Figure 5.7. We again find a small dependence on $M_{\rm BH}$, except for near the boundaries of our $M_{\rm BH}$ range, where the angle is quite sensitive to $\dot{m}$. The wind flows closer to the equator as we decrease $\dot{m}$, hence whether the wind is more polar or equatorial depends on the mass accretion rate of the system. This can be explained by considering that lower disc luminosities do not push the wind as strongly from below, and thus the wind escapes flowing closer to the equator.

5.4 Can UV line-driven winds be UFOs?

In Q20, wind trajectories could achieve arbitrarily large velocities, often surpassing the speed of light, due to the neglect of relativistic effects. With the introduction of relativistic corrections (section 4.5), the wind is always sub-luminal, as we show in Figure 5.4 and Figure 5.5. Nonetheless, throughout the simulated parameter space, outflows consistently achieve speeds of $(0.1 - 0.8)$ c, scaling approximately as $\dot{m}$ with little dependence on $M_{\rm BH}$. If we limit ourselves to the simulations that conserve the overall momentum and energy of the system, then the simulated wind still achieve speeds in the range $(0.1 - 0.4)$c. This implies that UV line-driving is a feasible mechanism to produce UFOs even when relativistic corrections are included. The final velocity of the wind depends on how much a gas blob can be accelerated while it is shadowed from the X-ray radiation. In Figure 5.8, we plot the velocity profile for a trajectory starting at $R = 100R_{\rm g}$ in our fiducial simulation density grid for different values of the initial velocity. We find that the final velocity of the trajectory is independent of the initial velocity and that the wind is able to drastically accelerate (up to 6 orders of magnitude in velocity) over a very small distance ($\lesssim 1R_{\rm g}$), which suggests that line-driving can be very effective even when the X-ray shadowed region is very small.

We thus find that UV line-driving is sufficient to reproduce the range of observed UFO velocities, as opposed to the findings of Luminari et al. (2021). We note that their code assumes an initial density (similar to Q20) rather than calculating it from first principles, and does not include the full ray tracing of both UV and X-rays that are considered here. On the other hand, our treatment of the force multiplier is simplified compared to their calculation, where they use the radiative transfer code XSTAR (Kallman & Bautista, 2001) to compute the radiation flux absorbed by the wind. Nonetheless, our results show that a

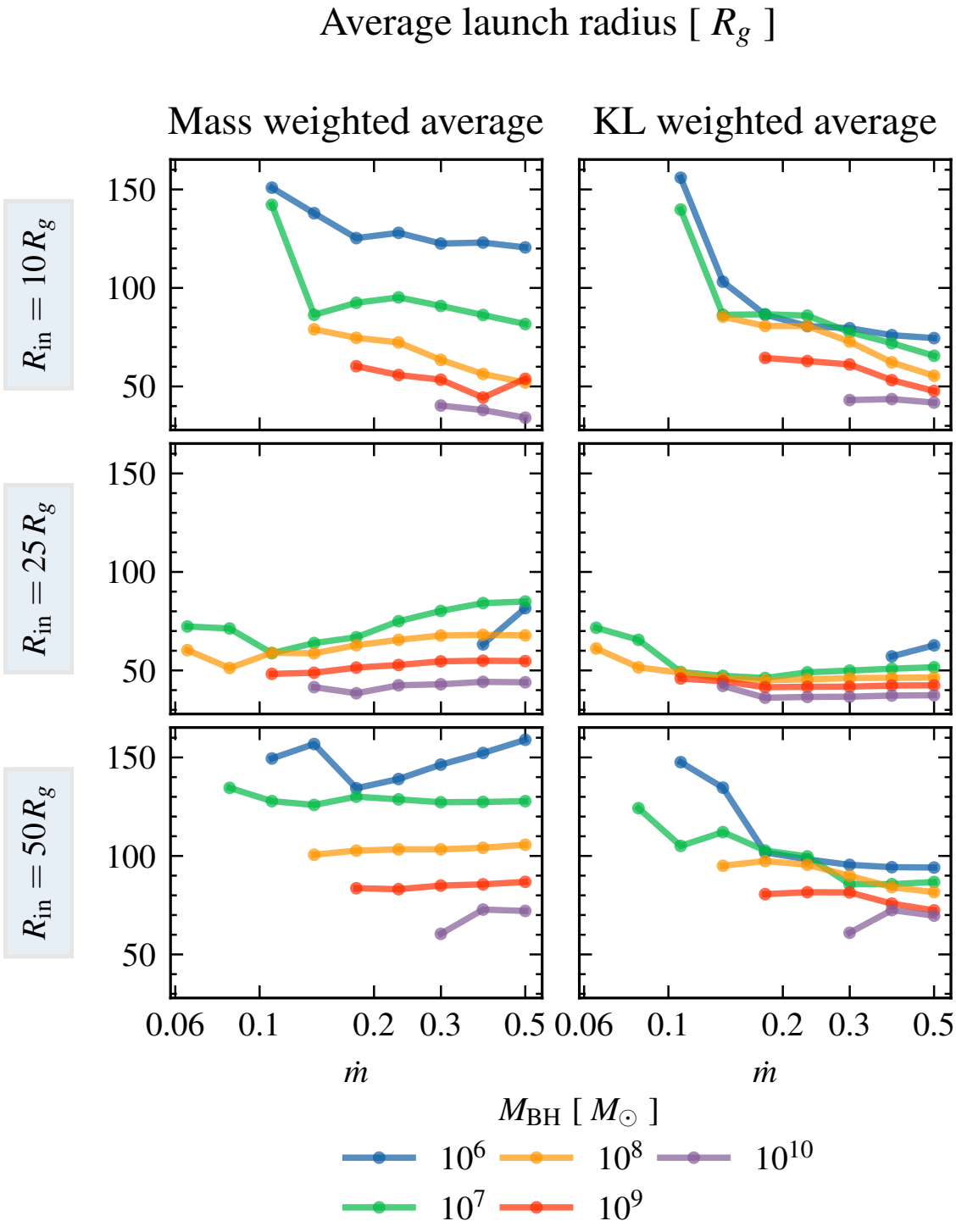

Figure 5.6: Average launch radius weighted by the trajectories' mass loss rate (left panels) and kinetic luminosity (right panels) as a function of $M_{\rm BH}$ and $\dot{m}$ for the 3 values of $R_{\rm in}$.

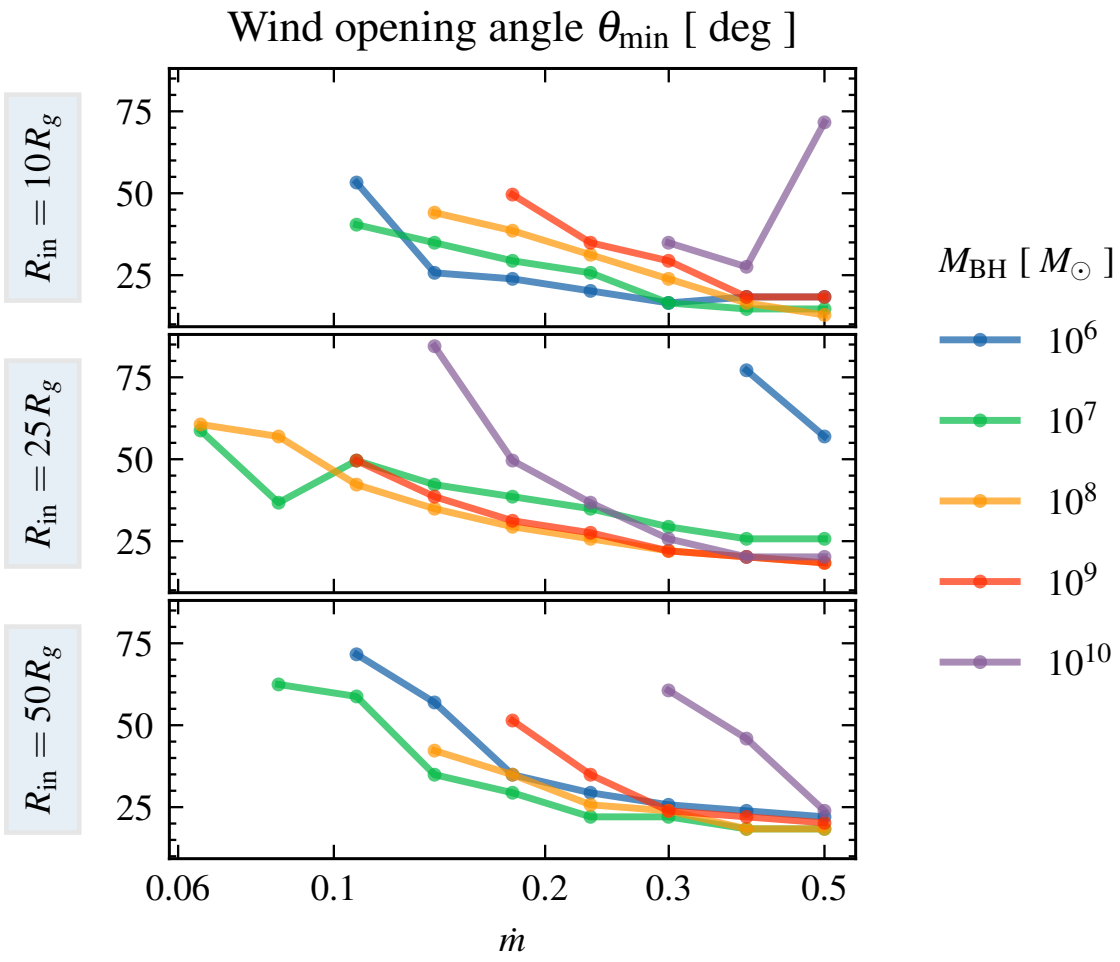

Figure 5.7: Wind opening angle, measured as the smallest polar angle, $\theta_{\rm min}$, of all escaping streamlines as a function of $M_{\rm BH}$ and $\dot{m}$, for the 3 studied $R_{\rm in}$ values.

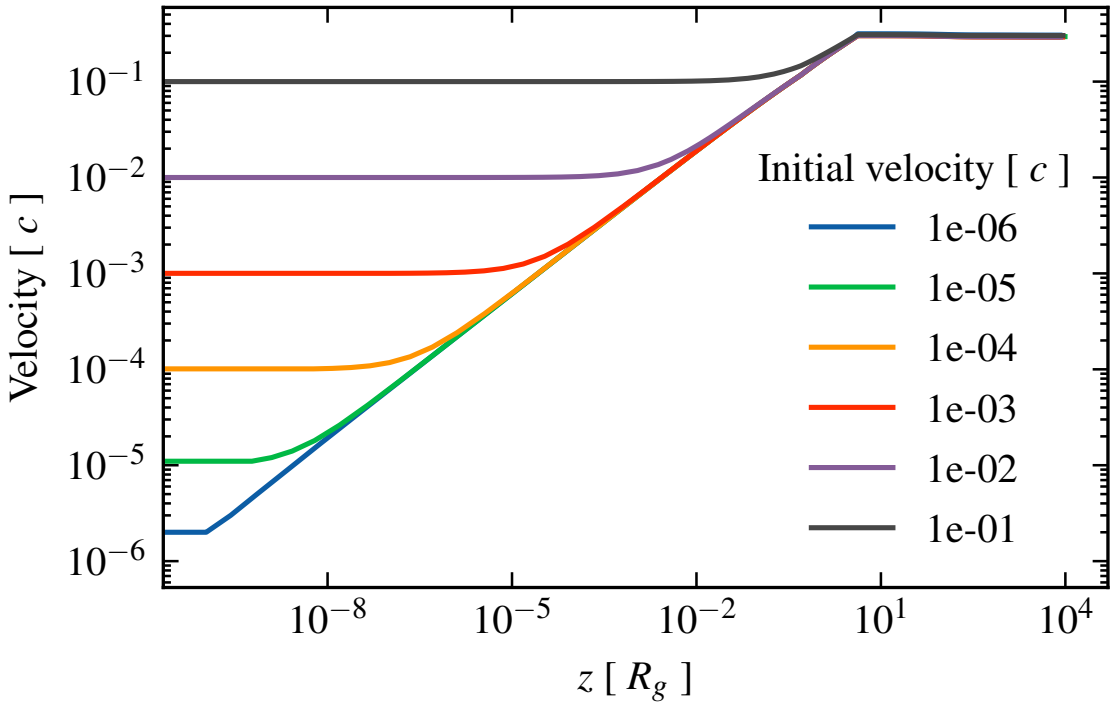

Figure 5.8: Velocity as a function of z for a trajectory starting at $R = 100R_{\rm g}$ for our fiducial model. Different colours correspond to different initial velocities.

small shaded region can produce a very fast wind (see Figure 5.8), and the range of $R_{\rm in}$ that gives rise to velocities $\geq 0.3c$ is quite wide (see Figure 5.6). It then seems quite likely that UV line-driven winds can indeed reach these velocities and hence be the origin of the majority of UFOs seen. There are even higher velocities claimed for a few absorption features in the literature, but these are generally low signal-to-noise detections (Chartas et al., 2021).

Chapter 6

Applications of computational techniques to other sciences

As a PhD student of the Centre for Doctoral Training in Data-Intensive Science[1], I've had the opportunity, during these past 4 years, to undertake research projects with industrial partners as well as working on my PhD. In the spring of 2018, I interned at the X-ray medical imaging company Ibex Innovations Ltd (Sedgefield, UK), where I co-developed a Convolutional Neural Network (CNN) for medical image segmentation. The results were presented at the SPIE Medical Imaging conference (Bullock et al., 2019).

The following spring of 2019, I joined the Boeing's digital aviation lab (Frankfurt, Germany), where I used deep learning assisted object recognition techniques to track aircraft ground operations.

Following the SARS-COV-2 outbreak in Europe at the beginning of 2020, I joined a multidisciplinary team of researchers at Durham University to develop JUNE, a high-resolution agent-based model to simulate the spread of SARS-COV-2 in the UK. The model has proven to be of high value to the National Health Service (NHS) and Public Health England (PHE) in supporting public policy and medical operations at different points of the epidemic. I also collaborated with a team of researchers at the United Nations Global Pulse initiative to adapt the model to the Cox's Bazar refugee camp in Bangladesh, working with on the ground World Health Organization (WHO) officials.

In what follows I write a short abstract of the publications that I have played a core role in developing.

[1] https://ddis.physics.dur.ac.uk/

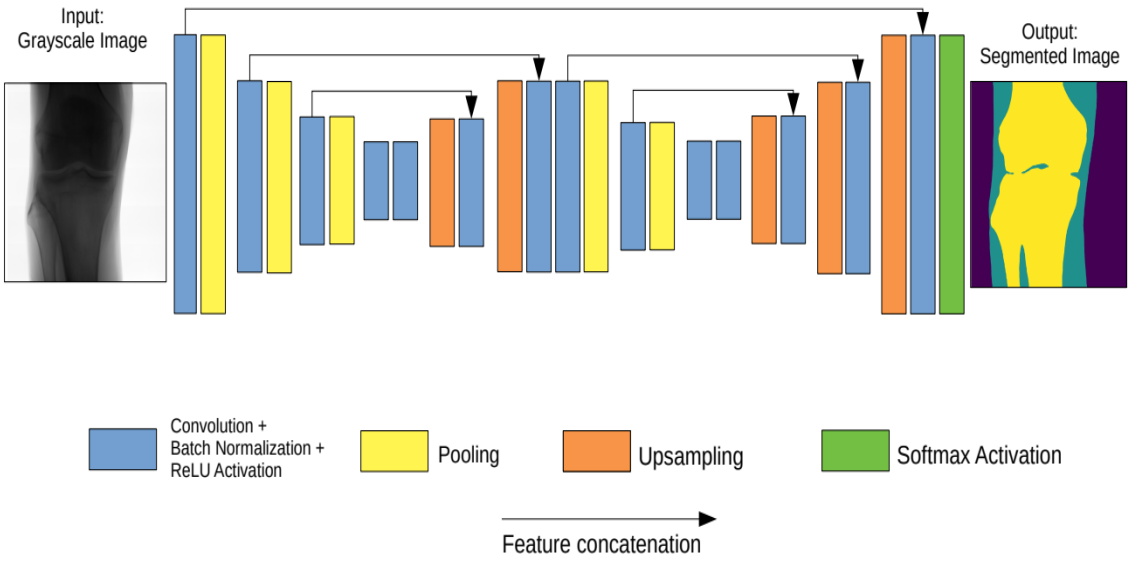

Figure 6.1: Visualisation of XNet architecture including example input image, left, and output segmented mask, right. Feature concatenation of same dimension layers helps to avoid losing fine-grained detail. Softmax activation function provides final pixel-wise classification

6.1 Medical X-ray image segmentation

X-Ray image enhancement, along with many other medical image processing applications, requires the segmentation of images into bone, soft tissue, and open beam regions. This is often a complex task, since the image can have multiple artefacts that can make classic image processing algorithms fail, as well as uncalibrated contrast settings or other irregularities. In (Bullock et al., 2019), I co-developed an end-to-end solution to the segmentation problem using a CNN trained on a small dataset. The algorithm achieved state-of-the-art results, with an overall accuracy of 92%, and it was performed consistently among multiple imaging settings, in contrast to other classical algorithms such as clustering or entropy based methods. Figure 6.1 shows the architecture of the designed CNN, its W-like shape is crucial on allowing the network to efficiently learn the relevant small and large scale features of the image.

In Figure 6.2, I show an example of the model inputs and outputs, where it can be seen that the CNN segments well among images of different body parts.

6.2 Aircraft ground operations

The aircraft turnaround process refers to the set of actions that need to take place to prepare an aircraft in the period it lands until it takes off again. Optimising turnaround time is

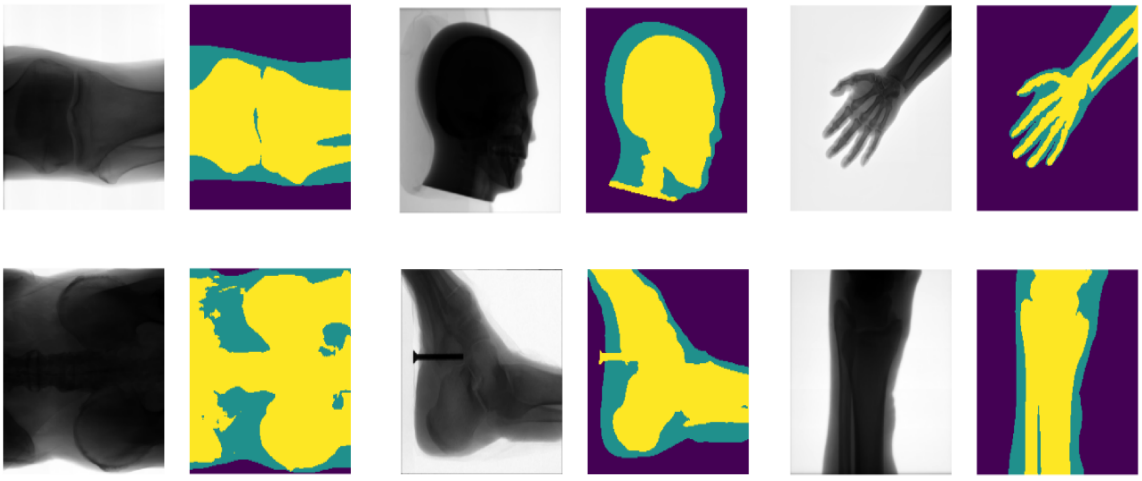

Figure 6.2: Segmentation predictions from the CNN's test set. Top row images show a knee, phantom head and hand. Bottom row shows a pelvis, ankle with a metallic bolt, and the lower half of a leg. The open beam area is shown in purple. Bone is shown in yellow and soft tissue in green.

critical for aircraft operations to prevent delays and reduce costs. Typically, the tracking of the turnaround process is done manually by the airline's operators who may not have access to all the data that could help the tracking process. During my internship at Boeing's digital aviation laboratory, I designed a data processing and machine learning pipeline capable of automatically detecting through video input the different components of the aircraft turnaround phase. In Figure 6.3, I show an example application of this technology, in this case developed by Gorkow (2020).

6.3 JUNE: Modelling the spread of SARS-COV-2 in the UK

Generally speaking, epidemiological modelling approaches are divided between susceptible-infected-recovered (SIR) models (Kermack & McKendrick, 1927) and agent-based models (Abar et al., 2017). The advantage of the latter is the granularity of the results, since each person in a population is modelled independently, however, it often also involves a much greater computational cost and difficulty to interpret the results. As part of the JUNE collaboration (Aylett-Bullock et al., 2021a), I build an open-source agent-based framework (Quera-Bofarull et al., 2022) to model epidemic spread within a geographical context. The attributes of the virtual population such as age and sex are modelled at a very high resolution. Agents can interact in a variety of settings (households, schools, social venues, etc.) with different levels of contact intensities. The population model coupled with a very flexible implementation of the disease progression for the agents makes JUNE one of the most detailed

Figure 6.3: Example of an object detection algorithm applied to an image of the aircraft's turnaround phase. The different kinds of trucks are differentiated and used as a proxy to infer which process is taking place at each time. Image taken from Gorkow (2020).

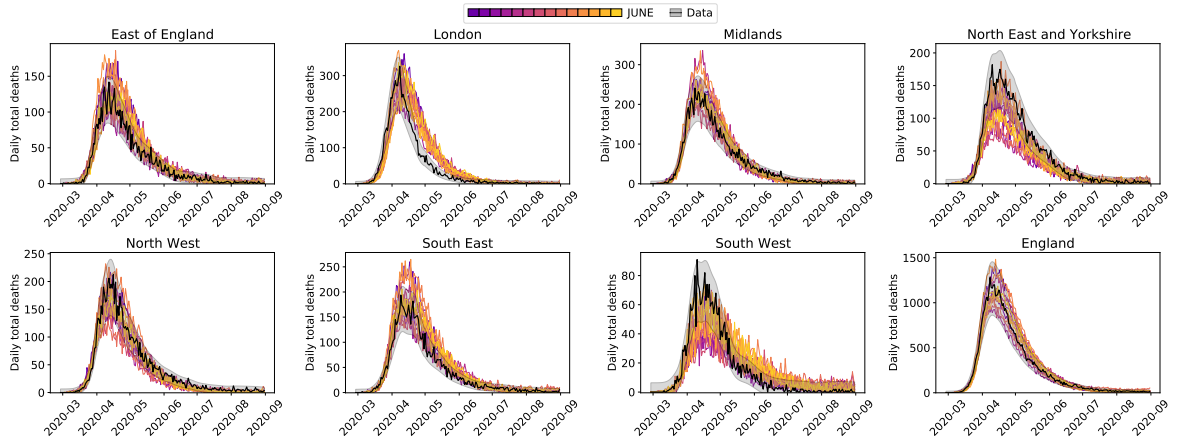

Figure 6.4: Regional daily deaths for the different regions comprising England. Data is shown in black, while the curves in colour denote multiple parameter sets compatible with the data.

epidemiological models to date.

In (Aylett-Bullock et al., 2021a), the model is applied to the case of England's first wave of SARS-COV-2 infections, where the model is calibrated using Bayesian history matching (Andrianakis et al., 2015) against real hospitalisation and deaths data. The resulting best model fits are shown in Figure 6.4, where we can see that JUNE reproduces regional differences without requiring the tuning of region-specific parameters.

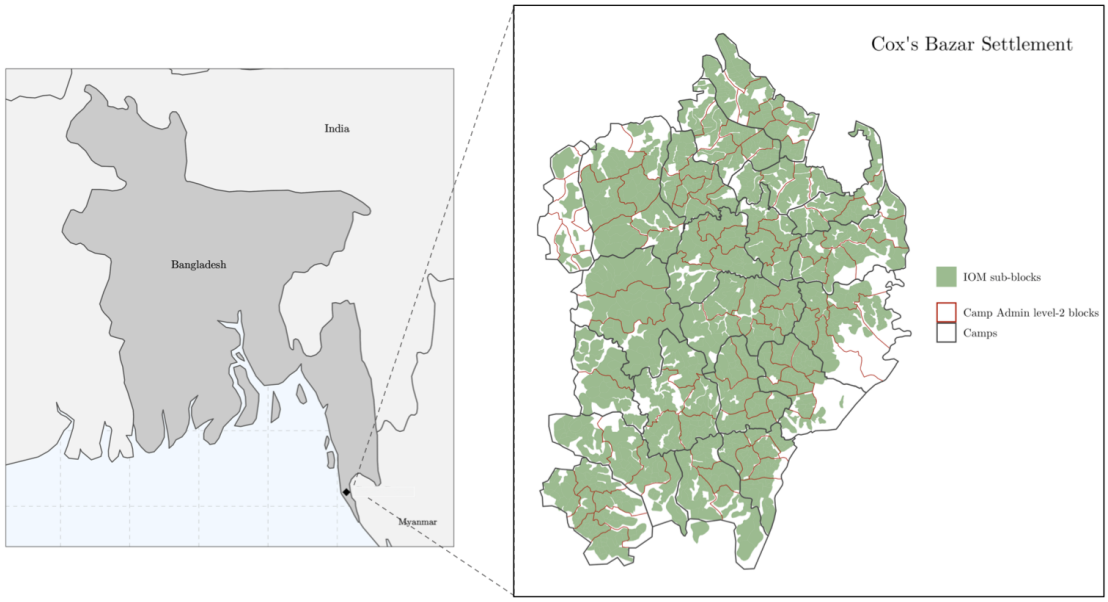

Figure 6.5: The location and structure of the Cox's Bazaar settlement in Bangladesh.

6.4 Applying JUNE to refugee settlements in Bangladesh

JUNE is built with flexibility in mind, and so it can be easily adapted to a variety of geographical and demographical settings. In Aylett-Bullock et al. (2021b), I worked in adapting the JUNE framework to simulate the spread of SARS-COV-2 in the Cox's Bazar refugee settlement in Bangladesh (Figure 6.5). Together with a multidisciplinary team of researchers and camp staff, we developed a visualisation analytics tool which allowed decision makers to make sense of the results produced by different simulations, with the aim of assessing the effectiveness of different non-pharmaceutical interventions (NPI). The impact of several NPI policies was investigated, from mask wearing compliance to the reopening of education centres.

6.5 Studying the safe reopening of schools in England with JUNE

In September 2021, high levels of Delta variant infections were occurring in England, with schools set to reopen with few countermeasures and small vaccination rates among children. In Cuesta-Lazaro et al. (2021), I worked on implementing the vaccination modelling into the JUNE code, so that the effect of children vaccination campaigns on infection rates could be assessed. Additionally, alternative NPI measures were considered, such as quarantine

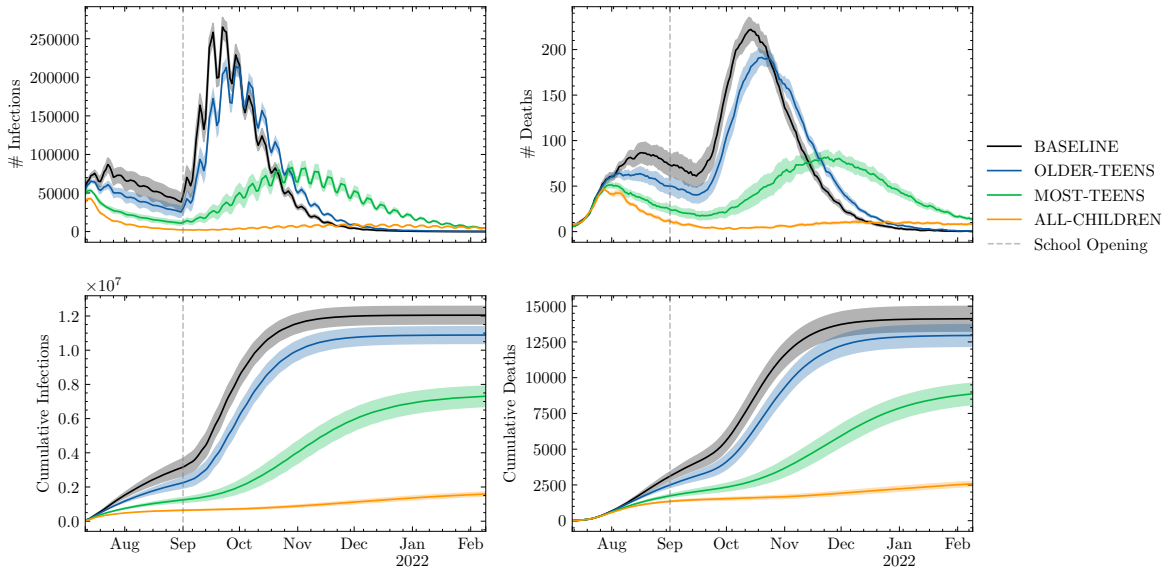

Figure 6.6: Number of new infections (left) and number of deaths (right) per day, daily (upper) and cumulative (lower). Four different scenarios are shown in which $\simeq 80\%$ of the eligible population is vaccinated: BASELINE - only those older than 18 ; OLDER-TEENS - those older than 16 are vaccinated; MOST-TEENS - those older than 12 are vaccinated; and ALL CHILDREN - the entire population is eligible.

policies or social distancing. In Figure 6.6, I show part of the results of this work, where the number of infections and deaths is shown for different vaccination scenarios, corresponding to different age vaccination rates among children. The shadow regions are an estimate of model uncertainty.

Chapter 7

Conclusions and Future Work

In this thesis we have developed a numerical method to calculate the dynamics of UV line-driven winds in AGN accretion discs.

7.1 Summary

In chapter 2, we introduced the physics of UV line-driven winds in AGN and the modelling attempts at understanding their launch and acceleration mechanisms. Radiation-hydrodnyamics (RHD) simulations are often used to study line-driven systems, but they have the disadvantage of being computationally expensive. Risaliti & Elvis (2010) started a new approach to modelling these winds, called Qwind, by using a non-hydrodynamical model that solves the ballistic trajectories of gas blobs moving under the effects of radiation pressure and gravity. In chapter 3, we reviewed how Qwind works, making the integration of the radiation force and the solution of the equations of motion much more numerically robust. The resulting code was named Qwind2 and made available to the community. We also highlighted the importance of the initial conditions in Qwind for launching the wind from the surafce of the disc, given how sensitive the wind is to those. Furthermore, we realised that the wind can easily reach supra-luminal speeds in the absence of relativistic corrections.

A number of the Qwind shortcomings were addressed in chapter 4. First, we calculated the amount of UV radiation emitted at each disc radius, to correctly compute the radiation force with the disc SED. Second, we derived a self-consistent model to calculate the initial conditions of the wind, based on the CAK formalism, removing two free parameters from the original Qwind model that severely limited its predictive power. Third, we presented a ray tracing algorithm capable of computing the attenuation of each individual light ray

coming from the disc while taking into account the full density structure of the wind. Fourth and last, we introduced relativistic corrections to the radiation flux felt by the wind. The resulting code was named QWIND3 and is also publicly available.

The improvements on the treatment of the radiation transfer (RT) of QWIND have a big impact on the wind dynamics (see Figure 4.14) and so it was important to address them. In chapter 3, we compared the results of the classical QWIND model to the RHD simulations of Proga & Kallman (2004). Since we did not have a model to compute the initial conditions from first principles, we chose an initial density profile that fit well the RHD results. This is a bit unsatisfactory, since ideally we would like to use QWIND without having to callibrate a free parameter to the RHD simulations. To that end, in QWIND3 we were able to determine the initial conditions of the wind from first principles, and thus compare to the RHD simulations again in section 4.8 but this time without any room for tuning free parameters. The resulting global properties of the wind were consistent with the RHD results, but obtained with a much lower computational cost, proving the usefulness of the method.

With the assurance of correctness after comparing to the RHD simulations, we used QWIND3 to explore the BH parameter space in chapter 5, investigating the dependence of the wind dynamics on the BH mass, mass accretion rate, and the innermost launching radius. We found that the wind's kinetic luminosity and mass loss rate are highly sensitive to the BH mass accretion rate, scaling like a power-law with the normalised mass accretion rate, $\dot{m}$, but being quite insensitive to $M_{\rm BH}$ over a large range of mass. This last point was expected, since only the dependence of the UV fraction, $f_{\rm UV}$, with $M_{\rm BH}$ breaks the invariance of the normalised wind properties when scaling $M_{\rm BH}$.

The steep dependence with $\dot{m}$ may be a critical factor to modelling AGN feedback in cosmological simulations. Indeed, state-of-the-art models such as Eagle (Schaye et al., 2015) or Illustris (Vogelsberger et al., 2014) assume that a constant fraction of the accreted rest mass energy by the BH gets injected into its surroundings. It is important to consider, however, that, in QWIND3, many of the simulated winds at high accretion rates absorb more momentum and energy from the radiation field than what is available. This is likely a consequence of an incomplete RT calculation, which does not include the line opacity on the UV optical depth calculation. Another factor that could ameliorate this problem would be modelling the disc and the wind as a joint system, that is, taking into account the effect on the disc of the mass loss to the wind, effectively reducing its surface brightness.

Lastly, we addressed the question whether UV line-driven winds can be a good candidate

to explain the observations of UFOs in AGN. The inclusion of relativistic corrections in QWIND3 guaranteed that the wind stays sub-luminal throughout all the scanned parameter space, however, high velocity winds ($> 0.1\ c$) are still achieved, and the final velocity of the wind does not seem to be very sensitive to the BH parameters and it is independent of the initial velocity, which is not a free parameter in QWIND3. The high levels of ionisation often observed in UFOs are not necessarily inconsistent with line-driving, since both the failed wind region and the accelerating region are located at very low heights, thus explaining why lines of sight through the wind can mostly intercept material ionised by the X-rays, while still being accelerated through line-driving. Hence, we conclude line-driving is a plausible mechanism to generate UFOs in the context of AGN.

7.2 Future work

There are 3 important aspects where QWIND needs improvement to consolidate our understanding of UV line-driven winds in AGN. First, the treatment of the X-ray radiation is too simplified. As pointed out in Higginbottom et al. (2014), the ionisation in the wind may be underestimated by neglecting X-ray scattering. Second, the effect of the wind on the disc structure needs to be considered, since the disc's mass loss to the wind would reduce the disc surface density and hence the intensity of the radiation field, likely bringing the most powerful winds down from unphysically high momentum rates and kinetic luminosities. Third, it is important to consider the dependence of the force multiplier on the SED as well as including the effects of line opacity into the calculation of the UV optical depth. Next, I describe possible lines of research to target these issues.

7.2.1 Effect of X-ray scattering.

In QWIND, the only X-ray source considered so far is located at the centre of the grid, where the BH is. This neglects the fact that X-ray photons get scattered by the wind, so the wind itself may also be a source of radiation that can ionise the gas and hence shut down line-driving. The impact of X-ray scattering is assessed in Higginbottom et al. (2014), where they run a two-dimensional RT code on a snapshot of the RHD simulation in Proga & Kallman (2004). The results, already presented in chapter 2 are shown again in Figure 7.1. We can see that the rear part of the wind is significantly more ionised in the case where X-ray scattering is considered (right panel) than the simplified scenario where the only X-ray source is the

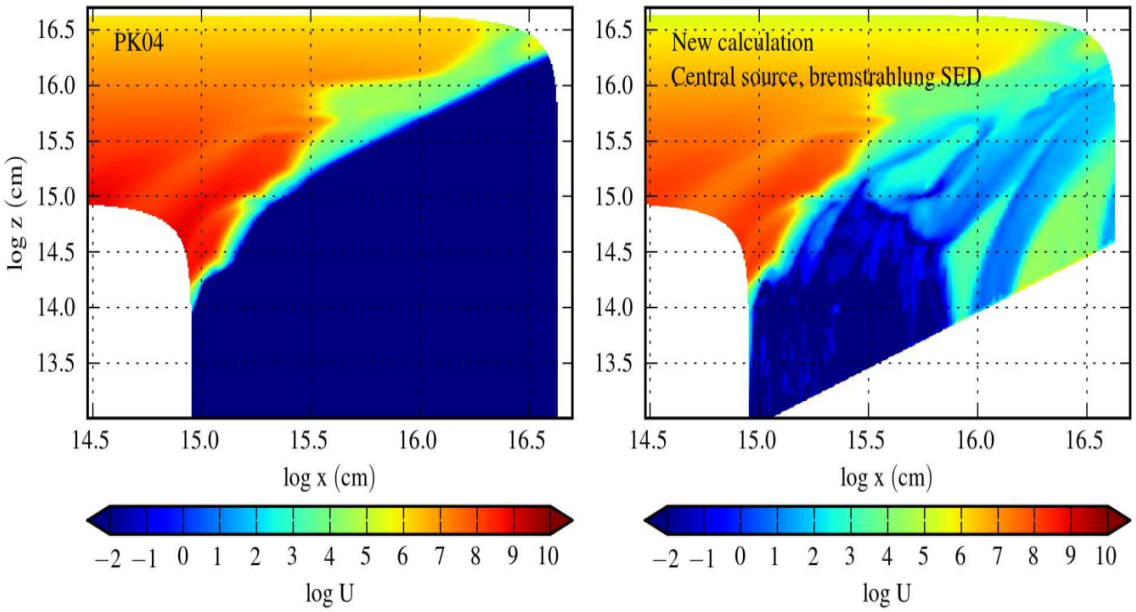

Figure 7.1: Ionisation parameter U related to our presented definition through $\log U = \log \xi - 1.75$ for a snapshot of the simulation Proga & Kallman (2004). The left panel corresponds to the calculation done in the RHD simulation, while the right panel is the result of a full RT calculation done with PYTHON (Long & Knigge, 2002). Figure taken from Higginbottom et al. (2014).

central one (left). This is thus not consistent with the results obtained in the RHD code, since the force multiplier would be dramatically lower in the regions of higher ionisation. Nonetheless, this may not necessarily imply that UV line-driving is not effective at pushing a powerful wind, since the wind could achieve a density and velocity configuration that would make shielding effective again.

To include these effects on Qwind, I envision two complementary approaches.

1. For an RHD simulation, the gas dynamics are updated at each time step of the simulation, implying that each time step would normally require a new calculation of the RT through the wind. One may choose only to update the computed radiation force every few time steps to avoid calling the RT code multiple times, but how to do this correctly is still uncertain. Qwind gives an efficient natural alternative. Because of the dependence of the RT on the structure of the wind, which is also determined by the RT, Qwind does an iterative procedure to find a self-consistent solution. Therefore, between two wind iterations, a fully detailed RT code could be called to compute the ionisation structure of the wind to correctly determine the force multiplier and thus the radiation force. Assuming that the convergence speed is not altered significantly, this would imply that the RT code only needs to be called $\sim$ 10 times, and the problem

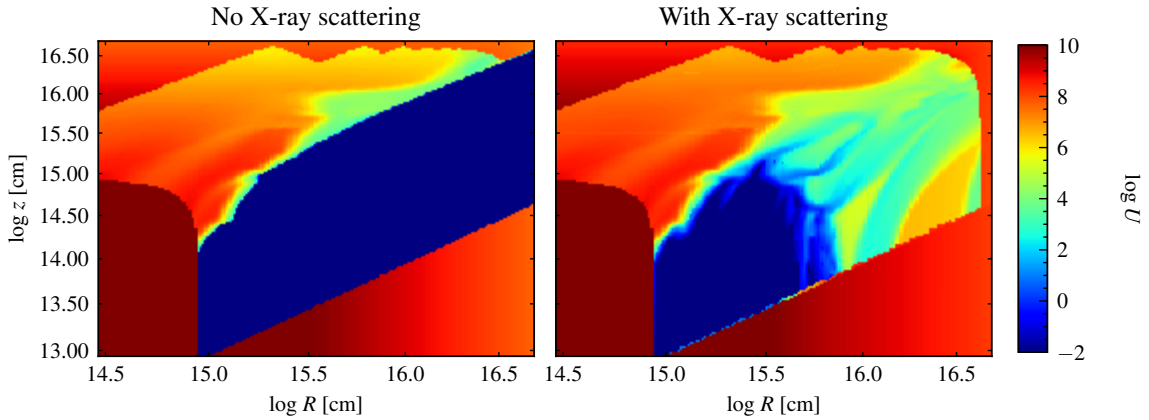

Figure 7.2: Wind ionisation parameter ($\log U = \log \xi - 1.75$) with no X-ray scattering (left) and with it (right). The scattering results are obtained with a first order algorithm built into QWIND.

remains computationally tractable.

2. The second approach is to build a first order approximation of X-ray scattering into QWIND. By making use of the RT algorithm presented in section 4.4, we can calculate the amount of X-ray luminosity absorbed by each grid cell. We then treat each grid cell as a source of X-ray radiation emitting the same amount of power they have absorbed. In both calculations, the attenuation of the light rays is taken into account. As defined, this method is a first order approximation to the full problem of scattering, since it does not consider secondary scatters, which would be relevant at the innermost regions of the wind, where the density is high. The results of the current implementation are shown in Figure 7.2, where we used the density field of the same snapshot of Proga & Kallman (2004) as in Figure 7.1. The two approaches give reasonably similar results, with the differences likely being a result of our first order treatment as well as our algorithm not taking into the full spectrum of interactions between radiation and matter with the same detail as the PYTHON code (Long & Knigge, 2002).

Developing both approaches is useful, since while the second approach is likely to be much faster, it may be oversimplified, but the comparison between the two methods would help us understand the physical mechanisms that are relevant for line-driving in AGN.

7.2.2 Decrease of mass accretion rate with radius

As already commented in chapter 5, for high mass accretion rates, QWIND computes winds to have momentum rates and kinetic luminosities higher that the allowed physical values.

This is a consequence of an inaccurate calculation of the radiation transport, but taking into account the mass loss of the disc to the wind could also bring the wind into physically sensible values. A simple approach to consider this, would be to adjust the local flow rate rate in the disc to take into account the wind mass loss, that is,

$$\dot{M}(R) = \dot{M} - \int_R^\infty \dot{M}_{\rm wind}(R')\mathrm{d}R', \tag{7.2.1}$$

where $\dot{M}$ is the global mass accretion rate and $\dot{M}_{\rm wind}$ is the local mass loss to the wind. The corresponding radiation flux (equation 3.2.5) would then be diminished, and the velocity of the wind would decrease. This is an approximation to the change in the radiation flux, since we have assumed that the disc solution remains the same, apart from the change in $\dot{M}$, which now depends on radius. A more accurate approach would be to solve the Navier-Stokes equation for the accretion disc with a mass loss term, as it is done in Laor & Davis (2014), and compute the new emitted flux.

7.2.3 Force multiplier with varying SED

The spectral shape of the UV and X-ray sources plays an important role on determining the force multiplier values. Ideally, one would use some kind of 2-dimensional RT code to determine the radiation force based on the local physical parameters of the wind such as density and chemical composition and the SED of the radiation source. This procedure is, for now, too computationally expensive to perform without approximations, since it would involve a vast amount of computations at each simulation time step. The classical approach of CAK is to parametrise the force multiplier as a function of local properties of the wind, such as the density and the velocity gradient, and use this parametrisation to solve the equations of motion of the wind.

Going forward, similar approaches could be taken to improve on these issue as the ones we described for including X-ray scattering. The radiation force could be computed between Qwind iterations with a more sophisticated RT code, giving the correct ionisation structure, and thus the correct force multiplier that also considers the particular SED. This approach would also make it possible to include line opacity in the UV optical depth calculation.

7.2.4 New AGN feedback models

Finally, one of the main motivations to develop the Qwind model was for it to be used as a new AGN feedback prescription model. The obtained scaling of the outflow properties

with $M_{\rm BH}$ and $\dot{m}$ may have important consequences for galaxy formation models, since it is quite different than the one used in typical simulations suites. Thus an interesting line of research would be to use the QWIND scalings in a simulation of galaxy formation with AGN feedback, and to analyse if the energy injection rate predicted by QWIND can be succesful at reproducing observables without much need of extra calibration.

Bibliography

Abar, S., Theodoropoulos, G.K., Lemarinier, P., et al. *Agent Based Modelling and Simulation tools: A review of the state-of-art software.* Computer Science Review, **24** (2017), 13. ISSN 1574-0137.

Abbott, D.C. *The theory of radiatively driven stellar winds. II. The line acceleration.* The Astrophysical Journal, **259** (1982), 282. ISSN 0004-637X.

Abramowicz, M.A., Chen, X., Kato, S., et al. *Thermal Equilibria of Accretion Disks.* The Astrophysical Journal, **438** (1995), L37. ISSN 0004-637X.

Andersson, C., Führer, C., Åkesson, J. *Assimulo: A unified framework for ODE solvers.* Mathematics and Computers in Simulation, **116** (2015), 26. ISSN 0378-4754.

Andrianakis, I., Vernon, I.R., McCreesh, N., et al. *Bayesian History Matching of Complex Infectious Disease Models Using Emulation: A Tutorial and a Case Study on HIV in Uganda.* PLoS Computational Biology, **11** (2015), e1003968.

Arav, N. *The "Ghost of LY alpha " as Evidence for Radiative Acceleration in Quasars.* The Astrophysical Journal, **465** (1996), 617. ISSN 0004-637X.

Arav, N., Korista, K.T., Barlow, T.A., et al. *Radiative acceleration of gas in quasars.* Nature, **376** (1995), 576. ISSN 0028-0836.

Arav, N., Li, Z.Y. *The Role of Radiative Acceleration in Outflows from Broad Absorption Line QSOs. I. Comparison with O Star Winds.* The Astrophysical Journal, **427** (1994), 700. ISSN 0004-637X.

Aylett-Bullock, J., Cuesta-Lazaro, C., Quera-Bofarull, A., et al. *JUNE: open-source individual-based epidemiology simulation.* Royal Society Open Science, **8** (2021a), 210506.

Aylett-Bullock, J., Cuesta-Lazaro, C., Quera-Bofarull, A., et al. *Operational response simulation tool for epidemics within refugee and IDP settlements: A scenario-based case study*

of the Cox's Bazar settlement. PLOS Computational Biology, **17**(10) (2021b), e1009360. ISSN 1553-7358.

Balbus, S.A., Hawley, J.F. *Instability, turbulence, and enhanced transport in accretion disks.* Reviews of Modern Physics, **70**(1) (1998), 1.

Baldry, I.K., Driver, S.P., Loveday, J., et al. *Galaxy And Mass Assembly (GAMA): the galaxy stellar mass function at z \textless 0.06.* Monthly Notices of the Royal Astronomical Society, **421** (2012), 621. ISSN 0035-8711.

Baskin, A., Laor, A. *Dust inflated accretion disc as the origin of the broad line region in active galactic nuclei.* Monthly Notices of the Royal Astronomical Society, **474** (2018), 1970. ISSN 0035-8711.

Beasley, D. *Most Powerful Eruption in the Universe Discovered.* Chandra Press Release (2005), 1.

Begelman, M.C., McKee, C.F., Shields, G.A. *Compton heated winds and coronae above accretion disks. I. Dynamics.* The Astrophysical Journal, **271** (1983), 70. ISSN 0004-637X.

Berntsen, J., Espelid, T.O., Genz, A. *An adaptive algorithm for the approximate calculation of multiple integrals.* ACM Transactions on Mathematical Software, **17**(4) (1991), 437. ISSN 0098-3500.

Bertone, G., Hooper, D., Silk, J. *Particle dark matter: evidence, candidates and constraints.* Physics Reports, **405** (2005), 279. ISSN 0370-1573.

Bezanson, J., Edelman, A., Karpinski, S., et al. *Julia: A Fresh Approach to Numerical Computing.* SIAM Review, **59**(1) (2017), 65. ISSN 0036-1445.

Blades, J.C., Turnshek, D.A., Norman, C.A. *QSO absorption lines: Probing the universe.* Cambridge University Press (1988). Publication Title: Proceedings of the QSO Absorption Line Meeting ADS Bibcode: 1988qsal.proc.....B.

Blandford, R.D., Payne, D.G. *Hydromagnetic flows from accretion disks and the production of radio jets.* Monthly Notices of the Royal Astronomical Society, **199** (1982), 883.

Blandford, R.D., Znajek, R.L. *Electromagnetic extraction of energy from Kerr black holes.* Monthly Notices of the Royal Astronomical Society, **179** (1977), 433.

Bogovalov, S., Tsinganos, K. *On the magnetic acceleration and collimation of astrophysical outflows.* Monthly Notices of the Royal Astronomical Society, **305** (1999), 211. ISSN 0035-8711.

Bower, R.G., Benson, A.J., Crain, R.A. *What shapes the galaxy mass function? Exploring the roles of supernova-driven winds and active galactic nuclei.* Monthly Notices of the Royal Astronomical Society, **422** (2012), 2816. ISSN 0035-8711.

Bower, R.G., Benson, A.J., Malbon, R., et al. *Breaking the hierarchy of galaxy formation.* Monthly Notices of the Royal Astronomical Society, **370** (2006), 645. ISSN 0035-8711.

Bowler, R.A.A., Hewett, P.C., Allen, J.T., et al. *Line-driven radiative outflows in luminous quasars.* Monthly Notices of the Royal Astronomical Society, **445**(1) (2014), 359. ISSN 0035-8711.

Braun, E., Milgrom, M. *A Non–Steady State Line Locking in Broad Absorption Line Quasi-stellar Objects.* The Astrophysical Journal, **342** (1989), 100. ISSN 0004-637X. ADS Bibcode: 1989ApJ...342..100B.

Bullock, J., Cuesta-Lázaro, C., Quera-Bofarull, A. *XNet: a convolutional neural network (CNN) implementation for medical x-ray image segmentation suitable for small datasets.* In *Medical Imaging 2019: Biomedical Applications in Molecular, Structural, and Functional Imaging*, volume 10953. SPIE (2019), pages 453–463.

Cannizzo, J.K., Pudritz, R.E. *A New Angular Momentum Loss Mechanism for Cataclysmic Variables.* The Astrophysical Journal, **327** (1988), 840. ISSN 0004-637X.

Castor, J.I., Abbott, D.C., Klein, R.I. *Radiation-driven winds in Of stars.* The Astrophysical Journal, **195** (1975), 157. ISSN 0004-637X.

Chartas, G., Cappi, M., Vignali, C., et al. *Multiphase Powerful Outflows Detected in High-z Quasars.* The Astrophysical Journal, **920**(1) (2021), 24. ISSN 0004-637X.

Chelouche, D., Netzer, H. *Non-Sobolev modelling of radiation-pressure-driven flows in active galactic nuclei.* Monthly Notices of the Royal Astronomical Society, **344** (2003), 223. ISSN 0035-8711.

Choi, E., Ostriker, J.P., Naab, T., et al. *Radiative and Momentum-based Mechanical Active Galactic Nucleus Feedback in a Three-dimensional Galaxy Evolution Code.* The Astrophysical Journal, **754** (2012), 125. ISSN 0004-637X.

Condon, J.J., Cotton, W.D., Greisen, E.W., et al. *The NRAO VLA Sky Survey.* The Astronomical Journal, **115** (1998), 1693. ISSN 0004-6256.

Cordova, F.A., Mason, K.O. *High-velocity winds from a dwarf nova during outburst.* The Astrophysical Journal, **260** (1982), 716. ISSN 0004-637X.

Cottis, C.E., Goad, M.R., Knigge, C., et al. *Searching for the signature of radiative line driving: on the absence of Lyα-NV line-locking features in a large sample of BALQSOs.* Monthly Notices of the Royal Astronomical Society, **406** (2010), 2094. ISSN 0035-8711.

Crain, R.A., Eke, V.R., Frenk, C.S., et al. *The baryon fraction of ΛCDM haloes.* Monthly Notices of the Royal Astronomical Society, **377** (2007), 41. ISSN 0035-8711.

Crenshaw, D.M., Kraemer, S.B. *Feedback from Mass Outflows in Nearby Active Galactic Nuclei. I. Ultraviolet and X-Ray Absorbers.* The Astrophysical Journal, **753**(1) (2012), 75.

Croton, D.J., Springel, V., White, S.D.M., et al. *The many lives of active galactic nuclei: cooling flows, black holes and the luminosities and colours of galaxies.* Monthly Notices of the Royal Astronomical Society, **365** (2006), 11. ISSN 0035-8711.

Cuesta-Lazaro, C., Quera-Bofarull, A., Aylett-Bullock, J., et al. *Vaccinations or Non-Pharmaceutical Interventions:Safe Reopening of Schools in England.* medRxiv (2021), 2021.09.07.21263223.

Czerny, B., Hryniewicz, K. *The origin of the broad line region in active galactic nuclei.* Astronomy and Astrophysics, **525** (2011), L8. ISSN 0004-6361.

Czerny, B., Nikołajuk, M., Różańska, A., et al. *Universal spectral shape of high accretion rate AGN.* Astronomy and Astrophysics, v.412, p.317-329 (2003), **412** (2003), 317. ISSN 0004-6361.

Dannen, R.C., Proga, D., Kallman, T.R., et al. *Photoionization Calculations of the Radiation Force Due To Spectral Lines in AGNs.* The Astrophysical Journal, **882**(2) (2019), 99. ISSN 1538-4357.

Davé, R., Anglés-Alcázar, D., Narayanan, D., et al. *SIMBA: Cosmological simulations with black hole growth and feedback.* Monthly Notices of the Royal Astronomical Society, **486** (2019a), 2827. ISSN 0035-8711.

Davé, R., Anglés-Alcázar, D., Narayanan, D., et al. *SIMBA: Cosmological simulations with black hole growth and feedback*. Monthly Notices of the Royal Astronomical Society, **486** (2019b), 2827. ISSN 0035-8711.

Davis, M., Efstathiou, G., Frenk, C.S., et al. *The evolution of large-scale structure in a universe dominated by cold dark matter*. The Astrophysical Journal, **292** (1985), 371. ISSN 0004-637X.

Dekel, A., Silk, J. *The Origin of Dwarf Galaxies, Cold Dark Matter, and Biased Galaxy Formation*. The Astrophysical Journal, **303** (1986), 39. ISSN 0004-637X.

Done, C., Davis, S.W., Jin, C., et al. *Intrinsic disc emission and the soft X-ray excess in active galactic nuclei*. Monthly Notices of the Royal Astronomical Society, **420** (2012), 1848. ISSN 0035-8711.

Done, C., Tomaru, R., Takahashi, T. *Thermal winds in stellar mass black hole and neutron star binary systems*. Monthly Notices of the Royal Astronomical Society, **473** (2018), 838. ISSN 0035-8711.

Dorodnitsyn, A., Kallman, T. *Active Galactic Nucleus Obscuration from Winds: From Dusty Infrared-driven to Warm and X-Ray Photoionized*. The Astrophysical Journal, **761** (2012), 70. ISSN 0004-637X. ADS Bibcode: 2012ApJ...761...70D.

Dorodnitsyn, A., Kallman, T., Proga, D. *Parsec-scale Accretion and Winds Irradiated by a Quasar*. The Astrophysical Journal, **819** (2016), 115. ISSN 0004-637X. ADS Bibcode: 2016ApJ...819..115D.

Dyda, S., Proga, D. *Effects of radiation field geometry on line driven disc winds*. Monthly Notices of the Royal Astronomical Society, **481**(2) (2018a), 2745.

Dyda, S., Proga, D. *Non-axisymmetric line-driven disc winds - I. Disc perturbations*. Monthly Notices of the Royal Astronomical Society, **475**(3) (2018b), 3786.

Dyda, S., Proga, D. *Non-axisymmetric line-driven disc winds II - full velocity gradient*. Monthly Notices of the Royal Astronomical Society, **478**(4) (2018c), 5006.

Eggum, G.E., Coroniti, F.V., Katz, J.I. *Radiation Hydrodynamic Calculation of Super-Eddington Accretion Disks*. The Astrophysical Journal, **330** (1988), 142. ISSN 0004-637X.

Esin, A.A., McClintock, J.E., Narayan, R. *Advection-Dominated Accretion and the Spectral States of Black Hole X-Ray Binaries: Application to Nova Muscae 1991*. The Astrophysical Journal, **489** (1997), 865. ISSN 0004-637X.

Fabian, A.C. *Observational Evidence of Active Galactic Nuclei Feedback*. Annual Review of Astronomy and Astrophysics, **50** (2012), 455.

Fabian, A.C., Celotti, A., Erlund, M.C. *Radiative pressure feedback by a quasar in a galactic bulge*. Monthly Notices of the Royal Astronomical Society, **373** (2006), L16. ISSN 0035-8711.

Fath, E.A. *The spectra of some spiral nebulae and globular star clusters*. Lick Observatory Bulletin, **149** (1909), 71. ISSN 0075-9317.

Foltz, C.B., Chaffee, Jr., F.H., Hewett, P.C., et al. *The APM QSO Survey. I. Initial MMT Results*. The Astronomical Journal, **94** (1987a), 1423. ISSN 0004-6256.

Foltz, C.B., Weymann, R.J., Morris, S.L., et al. *The Complex Absorption Spectrum of the Broad Absorption Line QSO 1303+308*. The Astrophysical Journal, **317** (1987b), 450. ISSN 0004-637X.

Frank, J., King, A., Raine, D.J. *Accretion Power in Astrophysics: Third Edition*. Cambridge University Press (2002).

Friend, D.B., Abbott, D.C. *The Theory of Radiatively Driven Stellar Winds. III. Wind Models with Finite Disk Correction and Rotation*. The Astrophysical Journal, **311** (1986), 701. ISSN 0004-637X.

Fukumura, K., Kazanas, D., Shrader, C., et al. *Magnetic origin of black hole winds across the mass scale*. Nature Astronomy, **1**(4) (2017), 0062. ISSN 2397-3366.

Gabor, J.M., Davé, R., Oppenheimer, B.D., et al. *Quenching massive galaxies with on-the-fly feedback in cosmological hydrodynamic simulations*. Monthly Notices of the Royal Astronomical Society, **417** (2011), 2676. ISSN 0035-8711.

Ganguly, R., Brotherton, M.S., Cales, S., et al. *Outflows and the Physical Properties of Quasars*. The Astrophysical Journal, **665**(2) (2007), 990.

Garrett, J. *SciencePlots (v1.0.9)* (2021).

George, I.M., Fabian, A.C. *X-ray reflection from cold matter in Active Galactic Nuclei and X-ray binaries.* Monthly Notices of the Royal Astronomical Society, **249** (1991), 352. ISSN 0035-8711.

Gofford, J., Reeves, J.N., McLaughlin, D.E., et al. *The Suzaku view of highly ionized outflows in AGN - II. Location, energetics and scalings with bolometric luminosity.* Monthly Notices of the Royal Astronomical Society, **451**(4) (2015), 4169. ISSN 0035-8711.

Gorkow, M. *Aircraft Turnaround Management Using Computer Vision* (2020). Publication Title: Medium.

Greenstein, J.L., Oke, J.B. *RW Sex, a disk with a hot, high-velocity wind.* The Astrophysical Journal, **258** (1982), 209. ISSN 0004-637X.

Grudić, M.Y., Guszejnov, D., Hopkins, P.F., et al. *STARFORGE: Towards a comprehensive numerical model of star cluster formation and feedback.* Monthly Notices of the Royal Astronomical Society, **506** (2021), 2199. ISSN 0035-8711.

Haardt, F., Maraschi, L. *A Two-Phase Model for the X-Ray Emission from Seyfert Galaxies.* The Astrophysical Journal, **380** (1991), L51. ISSN 0004-637X.

Haardt, F., Maraschi, L. *X-Ray Spectra from Two-Phase Accretion Disks.* The Astrophysical Journal, **413** (1993), 507. ISSN 0004-637X.

Hagino, K., Odaka, H., Done, C., et al. *The origin of ultrafast outflows in AGN: Monte Carlo simulations of the wind in PDS 456.* Monthly Notices of the Royal Astronomical Society, **446** (2015), 663. ISSN 0035-8711.

Hamann, F., Chartas, G., McGraw, S., et al. *Extreme-velocity quasar outflows and the role of X-ray shielding.* Monthly Notices of the Royal Astronomical Society, **435** (2013), 133. ISSN 0035-8711.

Hameury, J.M., Viallet, M., Lasota, J.P. *The thermal-viscous disk instability model in the AGN context.* Astronomy and Astrophysics, Volume 496, Issue 2, 2009, pp.413-421, **496**(2) (2009), 413. ISSN 0004-6361.

Harris, C.R., Millman, K.J., Walt, S.J.v.d., et al. *Array programming with NumPy.* Nature, **585**(7825) (2020), 357. Publisher: Springer Science and Business Media LLC.

Harrison, C. *Observational constraints on the influence of active galactic nuclei on the evolution of galaxies.* PhD Thesis, Durham University (2014).

Heap, S.R., Boggess, A., Holm, A., et al. *IUE observations of hot stars : HZ 43, BD +75 325, NGC 6826, SS Cyg, eta Car.* Nature, **275** (1978), 385. ISSN 0028-0836.

Higginbottom, N., Proga, D., Knigge, C., et al. *Line-driven Disk Winds in Active Galactic Nuclei: The Critical Importance of Ionization and Radiative Transfer.* The Astrophysical Journal, **789**(1) (2014), 19. ISSN 0004-637X, 1538-4357.

Hindmarsh, A.C., Brown, P.N., Grant, K.E., et al. *SUNDIALS: Suite of nonlinear and differential/algebraic equation solvers.* ACM Transactions on Mathematical Software, **31**(3) (2005), 363. ISSN 0098-3500.

Ho, L.C. *The Spectral Energy Distributions of Low-Luminosity Active Galactic Nuclei.* The Astrophysical Journal, **516** (1999), 672. ISSN 0004-637X.

Hopkins, P.F., Elvis, M. *Quasar feedback: more bang for your buck.* Monthly Notices of the Royal Astronomical Society, **401**(1) (2010), 7. ISSN 0035-8711.

Hopkins, P.F., Wetzel, A., Kereš, D., et al. *FIRE-2 simulations: physics versus numerics in galaxy formation.* Monthly Notices of the Royal Astronomical Society, **480** (2018), 800. ISSN 0035-8711.

Hoyle, F., Fowler, W.A. *Nature of Strong Radio Sources.* Nature, **197** (1963), 533. ISSN 0028-0836.

Icke, V. *Radiative acceleration of gas above a luminous disk.* Nature, **266** (1977), 699. ISSN 0028-0836.

Iono, D., Wilson, C.D., Takakuwa, S., et al. *High-Resolution Imaging of Warm and Dense Molecular Gas in the Nuclear Region of the Luminous Infrared Galaxy NGC 6240.* The Astrophysical Journal, **659** (2007), 283. ISSN 0004-637X.

Johnson, S.G. *JuliaMath/Cubature.jl* (2021).

Kallman, T., Bautista, M. *Photoionization and High-Density Gas.* The Astrophysical Journal Supplement Series, **133** (2001), 221. ISSN 0067-0049.

Kato, S., Yamasaki, T., Abramowicz, M.A., et al. *Thermal Instability of Advection-Dominated Disks against Revised Local Perturbations.* Publications of the Astronomical Society of Japan, **49** (1997), 221. ISSN 0004-6264.

Kermack, W.O., McKendrick, A.G. *A Contribution to the Mathematical Theory of Epidemics.* Proceedings of the Royal Society of London Series A, **115** (1927), 700. ISSN 0080-46301364-5021.

King, A.R., Pringle, J.E., Livio, M. *Accretion disc viscosity: how big is alpha?* Monthly Notices of the Royal Astronomical Society, **376** (2007), 1740. ISSN 0035-8711.

Knigge, C. *The effective temperature distribution of steady-state, mass-losing accretion discs.* Monthly Notices of the Royal Astronomical Society, **309** (1999), 409. ISSN 0035-8711.

Knigge, C., Scaringi, S., Goad, M.R., et al. *The intrinsic fraction of broad-absorption line quasars.* Monthly Notices of the Royal Astronomical Society, **386** (2008), 1426. ISSN 0035-8711.

Koide, S., Shibata, K., Kudoh, T., et al. *Extraction of Black Hole Rotational Energy by a Magnetic Field and the Formation of Relativistic Jets.* Science, **295** (2002), 1688. ISSN 0036-8075.

Konigl, A., Kartje, J.F. *Disk-driven Hydromagnetic Winds as a Key Ingredient of Active Galactic Nuclei Unification Schemes.* The Astrophysical Journal, **434** (1994), 446. ISSN 0004-637X.

Kormendy, J., Fisher, D.B., Cornell, M.E., et al. *Structure and Formation of Elliptical and Spheroidal Galaxies.* The Astrophysical Journal Supplement Series, **182** (2009), 216. ISSN 0067-0049.

Kormendy, J., Ho, L.C. *Coevolution (Or Not) of Supermassive Black Holes and Host Galaxies.* Annual Review of Astronomy and Astrophysics, vol. 51, issue 1, pp. 511-653, **51**(1) (2013), 511. ISSN 0066-4146.

Krolik, J.H., Kriss, G.A. *Warm Absorbers in Active Galactic Nuclei: A Multitemperature Wind.* The Astrophysical Journal, **561** (2001), 684. ISSN 0004-637X.

Kubota, A., Done, C. *A physical model of the broad-band continuum of AGN and its implications for the UV/X relation and optical variability.* Monthly Notices of the Royal Astronomical Society, **480** (2018), 1247. ISSN 0035-8711.

Lacey, C., Cole, S. *Merger rates in hierarchical models of galaxy formation.* Monthly Notices of the Royal Astronomical Society, **262** (1993), 627. ISSN 0035-8711.

Lam, S.K., Pitrou, A., Seibert, S. *Numba: a LLVM-based Python JIT compiler*. In *Proceedings of the Second Workshop on the LLVM Compiler Infrastructure in HPC - LLVM '15*. ACM Press, Austin, Texas (2015). ISBN 978-1-4503-4005-2, pages 1–6.

Lamers, H.J.G.L.M., Cassinelli, J.P. *Introduction to Stellar Winds*. Cambridge University Press (1999).

Laor, A., Davis, S.W. *Line-driven winds and the UV turnover in AGN accretion discs*. Monthly Notices of the Royal Astronomical Society, **438** (2014), 3024. ISSN 0035-8711.

Laor, A., Netzer, H. *Massive thin accretion discs. - I. Calculated spectra.* Monthly Notices of the Royal Astronomical Society, **238** (1989), 897. ISSN 0035-8711.

Lattimer, A.S., Cranmer, S.R. *An Updated Formalism for Line-driven Radiative Acceleration and Implications for Stellar Mass Loss*. The Astrophysical Journal, **910** (2021), 48. ISSN 0004-637X.

Lin, C.C., Shu, F.H. *On the Spiral Structure of Disk Galaxies.* The Astrophysical Journal, **140** (1964), 646. ISSN 0004-637X.

Liu, G., Zakamska, N.L., Greene, J.E., et al. *Observations of feedback from radio-quiet quasars - II. Kinematics of ionized gas nebulae*. Monthly Notices of the Royal Astronomical Society, **436** (2013), 2576. ISSN 0035-8711.

Long, K.S., Knigge, C. *Modeling the Spectral Signatures of Accretion Disk Winds: A New Monte Carlo Approach*. The Astrophysical Journal, **579** (2002), 725. ISSN 0004-637X.

Luminari, A., Nicastro, F., Elvis, M., et al. *Speed limits for radiation-driven SMBH winds*. Astronomy and Astrophysics, **646** (2021), A111. ISSN 0004-6361.

Luminari, A., Tombesi, F., Piconcelli, E., et al. *The importance of special relativistic effects in modelling ultra-fast outflows*. Astronomy and Astrophysics, **633** (2020), A55. ISSN 0004-6361.

Magdziarz, P., Blaes, O.M., Zdziarski, A.A., et al. *A spectral decomposition of the variable optical, ultraviolet and X-ray continuum of NGC 5548*. Monthly Notices of the Royal Astronomical Society, **301** (1998), 179. ISSN 0035-8711.

Mehdipour, M., Branduardi-Raymont, G., Kaastra, J.S., et al. *Multiwavelength campaign on Mrk 509. IV. Optical-UV-X-ray variability and the nature of the soft X-ray excess*. Astronomy & Astrophysics, **534** (2011), A39. ISSN 0004-6361.

Mineshige, S., Kawaguchi, T., Takeuchi, M., et al. *Slim-Disk Model for Soft X-Ray Excess and Variability of Narrow-Line Seyfert 1 Galaxies.* Publications of the Astronomical Society of Japan, **52** (2000), 499. ISSN 0004-6264.

Mizumoto, M., Done, C., Tomaru, R., et al. *Thermally driven wind as the origin of warm absorbers in AGN.* Monthly Notices of the Royal Astronomical Society, **489** (2019), 1152. ISSN 0035-8711.

Mizumoto, M., Nomura, M., Done, C., et al. *UV line-driven disc wind as the origin of UltraFast Outflows in AGN.* Monthly Notices of the Royal Astronomical Society, **503** (2021), 1442. ISSN 0035-8711.

Moreira, A.J.C., Santos, M.Y. *Concave hull: A k-nearest neighbours approach for the computation of the region occupied by a set of points.* In J. Braz, P.P. Vázquez, J.M. Pereira, editors, *GRAPP (GM/R).* INSTICC - Institute for Systems and Technologies of Information, Control and Communication (2007). ISBN 978-972-8865-71-9, pages 61–68.

Murray, N., Chiang, J., Grossman, S.A., et al. *Accretion Disk Winds from Active Galactic Nuclei.* The Astrophysical Journal, **451** (1995), 498.

Naddaf, M.H., Czerny, B., Szczerba, R. *The Picture of BLR in 2.5D FRADO: Dynamics and Geometry.* The Astrophysical Journal, **920** (2021), 30. ISSN 0004-637X.

Nagar, N.M., Falcke, H., Wilson, A.S., et al. *Radio Sources in Low-Luminosity Active Galactic Nuclei. I. VLA Detections of Compact, Flat-Spectrum Cores.* The Astrophysical Journal, **542** (2000), 186. ISSN 0004-637X.

Narayan, R., McClintock, J.E., Yi, I. *A New Model for Black Hole Soft X-Ray Transients in Quiescence.* The Astrophysical Journal, **457** (1996), 821. ISSN 0004-637X.

Narayan, R., Yi, I. *Advection-dominated Accretion: A Self-similar Solution.* The Astrophysical Journal, **428** (1994), L13. ISSN 0004-637X.

Narayan, R., Yi, I. *Advection-dominated Accretion: Self-Similarity and Bipolar Outflows.* The Astrophysical Journal, **444** (1995), 231. ISSN 0004-637X.

Netzer, H. *Revisiting the Unified Model of Active Galactic Nuclei.* Annual Review of Astronomy and Astrophysics, vol. 53, p.365-408, **53** (2015), 365. ISSN 0066-4146.

Noebauer, U.M., Sim, S.A. *Self-consistent modelling of line-driven hot-star winds with Monte Carlo radiation hydrodynamics.* Monthly Notices of the Royal Astronomical Society, **453** (2015), 3120. ISSN 0035-8711.

Nomura, M., Ohsuga, K. *Line-driven disk wind model for ultra-fast outflows in active galactic nuclei – Scaling with luminosity.* Monthly Notices of the Royal Astronomical Society, **465**(3) (2017), 2873. ISSN 0035-8711, 1365-2966.

Nomura, M., Ohsuga, K., Done, C. *Line-driven disc wind in near-Eddington active galactic nuclei: decrease of mass accretion rate due to powerful outflow.* Monthly Notices of the Royal Astronomical Society, **494** (2020), 3616. ISSN 0035-8711.

Nomura, M., Ohsuga, K., Takahashi, H.R., et al. *Radiation Hydrodynamic Simulations of Line-Driven Disk Winds for Ultra Fast Outflows.* Publications of the Astronomical Society of Japan, **68**(1) (2016), 16. ISSN 0004-6264, 2053-051X.

Nomura, M., Ohsuga, K., Wada, K., et al. *Modeling Line-Driven Disk Wind for Broad Absorption Lines of Quasars.* Publications of the Astronomical Society of Japan, **65** (2013), 40.

Nomura, M., Omukai, K., Ohsuga, K. *Radiation hydrodynamics simulations of line-driven AGN disc winds: metallicity dependence and black hole growth.* arXiv e-prints (2021), arXiv:2107.14256.

North, M., Knigge, C., Goad, M. *A new sample of broad absorption-line quasars exhibiting the ghost of Lyman α.* Monthly Notices of the Royal Astronomical Society, **365** (2006), 1057. ISSN 0035-8711.

Novikov, I.D., Thorne, K.S. *Astrophysics of black holes.* Black Holes (Les Astres Occlus) (1973).

Odaka, H., Aharonian, F., Watanabe, S., et al. *X-Ray Diagnostics of Giant Molecular Clouds in the Galactic Center Region and Past Activity of Sgr A*.* The Astrophysical Journal, **740** (2011), 103. ISSN 0004-637X.

Ogata, E., Ohsuga, K., Yajima, H. *Hoyle-Lyttleton accretion on to black hole accretion disks with super-Eddington luminosity for dusty gas.* Publications of the Astronomical Society of Japan, **73** (2021), 929. ISSN 0004-6264.

Ohsuga, K., Mori, M., Nakamoto, T., et al. *Supercritical Accretion Flows around Black Holes: Two-dimensional, Radiation Pressure-dominated Disks with Photon Trapping.* The Astrophysical Journal, **628** (2005), 368. ISSN 0004-637X.

Pauldrach, A., Puls, J., Kudritzki, R.P. *Radiation-driven winds of hot luminous stars. Improvements of the theory and first results.* Astronomy and Astrophysics, Vol. 164, p. 86-100 (1986), **164** (1986), 86. ISSN 0004-6361.

Percival, W.J., Cole, S., Eisenstein, D.J., et al. *Measuring the Baryon Acoustic Oscillation scale using the Sloan Digital Sky Survey and 2dF Galaxy Redshift Survey.* Monthly Notices of the Royal Astronomical Society, **381** (2007), 1053. ISSN 0035-8711.

Pereyra, N.A. *Further Criteria for the Existence of Steady Line-driven Winds.* The Astrophysical Journal, **622**(1) (2005), 577. ISSN 0004-637X, 1538-4357.

Pereyra, N.A., Hillier, D.J., Turnshek, D.A. *On the Steady Nature of Line-driven Disk Winds: Application to Cataclysmic Variables.* The Astrophysical Journal, **636** (2006), 411. ISSN 0004-637X.

Pereyra, N.A., Kallman, T.R., Blondin, J.M. *Hydrodynamical Models of Line-driven Accretion Disk Winds.* The Astrophysical Journal, **477** (1997), 368. ISSN 0004-637X.

Pereyra, N.A., Owocki, S.P., Hillier, D.J., et al. *On the Steady Nature of Line-Driven Disk Winds.* The Astrophysical Journal, **608** (2004), 454. ISSN 0004-637X.

Peterson, J.R., Kahn, S.M., Paerels, F.B.S., et al. *High-Resolution X-Ray Spectroscopic Constraints on Cooling-Flow Models for Clusters of Galaxies.* The Astrophysical Journal, **590** (2003), 207. ISSN 0004-637X.

Petrucci, P.O., Ursini, F., De Rosa, A., et al. *Testing warm Comptonization models for the origin of the soft X-ray excess in AGNs.* Astronomy & Astrophysics, Volume 611, id.A59, \textlessNUMPAGES\textgreater19\textless/NUMPAGES\textgreater pp., **611** (2018), A59. ISSN 0004-6361.

Planck Collaboration, P., Ade, P.a.R., Aghanim, N., et al. *Planck 2015 results. XIII. Cosmological parameters.* Astronomy & Astrophysics, **594** (2016), A13. ISSN 0004-6361.

Ponti, G., Fender, R.P., Begelman, M.C., et al. *Ubiquitous equatorial accretion disc winds in black hole soft states.* Monthly Notices of the Royal Astronomical Society, **422** (2012), L11. ISSN 0035-8711.

Pounds, K.A., King, A.R., Page, K.L., et al. *Evidence of a high-velocity ionized outflow in a second narrow-line quasar PG 0844+349.* Monthly Notices of the Royal Astronomical Society, **346**(4) (2003a), 1025.

Pounds, K.A., Reeves, J.N., King, A.R., et al. *A high-velocity ionized outflow and XUV photosphere in the narrow emission line quasar PG1211+143.* Monthly Notices of the Royal Astronomical Society, **345**(3) (2003b), 705.

Pringle, J.E. *Thermal instabilities in accretion discs.* Monthly Notices of the Royal Astronomical Society, **177** (1976), 65. ISSN 0035-8711.

Pringle, J.E. *Accretion discs in astrophysics.* In: Annual review of astronomy and astrophysics. Volume 19. (A82-11551 02-90) Palo Alto, CA, Annual Reviews, Inc., 1981, p. 137-162., **19** (1981), 137. ISSN 0066-4146.

Proga, D., Kallman, T.R. *Dynamics of Line-driven Disk Winds in Active Galactic Nuclei. II. Effects of Disk Radiation.* The Astrophysical Journal, **616** (2004), 688. ISSN 0004-637X.

Proga, D., Kallman, T.R., Drew, J.E., et al. *Resonance Line Profile Calculations Based on Hydrodynamical Models of Cataclysmic Variable Winds.* The Astrophysical Journal, **572** (2002), 382. ISSN 0004-637X.

Proga, D., Stone, J.M., Drew, J.E. *Radiation-driven winds from luminous accretion discs.* Monthly Notices of the Royal Astronomical Society, **295**(3) (1998), 595.

Proga, D., Stone, J.M., Kallman, T.R. *Dynamics of Line-driven Disk Winds in Active Galactic Nuclei.* The Astrophysical Journal, **543** (2000), 686. ISSN 0004-637X.

Quataert, E., Di Matteo, T., Narayan, R., et al. *Possible Evidence for Truncated Thin Disks in the Low-Luminosity Active Galactic Nuclei M81 and NGC 4579.* The Astrophysical Journal, **525** (1999), L89. ISSN 0004-637X.

Quera-Bofarull, A., Cuesta, C., Aylett-Bullock, J., et al. *JUNE* (2022).

Quera-Bofarull, A., Done, C., Lacey, C., et al. *Qwind code release: a non-hydrodynamical approach to modelling line-driven winds in active galactic nuclei.* Monthly Notices of the Royal Astronomical Society, **495**(1) (2020), 402. ISSN 0035-8711, 1365-2966.

Rackauckas, C., Nie, Q. *DifferentialEquations.jl – A Performant and Feature-Rich Ecosystem for Solving Differential Equations in Julia.* The Journal of Open Research Software, **5**(1) (2017).

Ramirez-Velasquez, J.M., Klapp, J., Gabbasov, R., et al. *IMPETUS: New Cloudy's radiative tables for accretion onto a galaxy black hole.* The Astrophysical Journal Supplement Series, **226**(2) (2016), 22. ISSN 1538-4365.

Rees, M.J., Silk, J.I., Werner, M.W., et al. *Infrared Radiation from Dust in Seyfert Galaxies.* Nature, **223** (1969), 788. ISSN 0028-0836.

Reeves, J.N., O'Brien, P.T., Braito, V., et al. *A Compton-thick Wind in the High-luminosity Quasar, PDS 456.* The Astrophysical Journal, **701**(1) (2009), 493.

Reynolds, C.S., Fabian, A.C. *Warm absorbers in active galactic nuclei.* Monthly Notices of the Royal Astronomical Society, **273** (1995), 1167. ISSN 0035-8711.

Riess, A.G., Filippenko, A.V., Challis, P., et al. *Observational Evidence from Supernovae for an Accelerating Universe and a Cosmological Constant.* The Astronomical Journal, **116** (1998), 1009. ISSN 0004-6256.

Risaliti, G., Elvis, M. *A non-hydrodynamical model for acceleration of line-driven winds in active galactic nuclei.* Astronomy and Astrophysics, **516** (2010), A89. ISSN 0004-6361.

Rubin, V.C., Ford, Jr., W.K., Thonnard, N. *Rotational properties of 21 SC galaxies with a large range of luminosities and radii, from NGC 4605 (R=4kpc) to UGC 2885 (R=122kpc).* The Astrophysical Journal, **238** (1980), 471. ISSN 0004-637X.

Rybicki, G.B., Lightman, A.P. *Radiative Processes in Astrophysics.* Radiative Processes in Astrophysics, by George B. Rybicki, Alan P. Lightman, pp. 400. ISBN 0-471-82759-2. Wiley-VCH , June 1986. (1986).

Salpeter, E.E. *Accretion of Interstellar Matter by Massive Objects.* The Astrophysical Journal, **140** (1964), 796. ISSN 0004-637X.

Scargle, J.D. *The production of discrete, quantized outflow velocities by radiation pressure in stars, Seyfert nuclei, and quasi-stellar objects.* The Astrophysical Journal, **179** (1973), 705. ISSN 0004-637X.

Schaye, J., Crain, R.A., Bower, R.G., et al. *The EAGLE project: simulating the evolution and assembly of galaxies and their environments.* Monthly Notices of the Royal Astronomical Society, **446**(1) (2015), 521.

Shakura, N.I., Sunyaev, R.A. *Black holes in binary systems. Observational appearance.* Astronomy and Astrophysics, **24** (1973), 337. ISSN 0004-6361.

Shapiro, S.L., Lightman, A.P., Eardley, D.M. *A two-temperature accretion disk model for Cygnus X-1: structure and spectrum.* The Astrophysical Journal, **204** (1976), 187. ISSN 0004-637X.

Shimada, M.R., Ito, M., Hirata, B., et al. *Radiatively driven winds of OB stars* (1994).

Shlosman, I., Vitello, P.A., Shaviv, G. *Active galactic nuclei - Internal dynamics and formation of emission clouds.* The Astrophysical Journal, **294** (1985), 96. ISSN 0004-637X.

Silk, J., Rees, M.J. *Quasars and galaxy formation.* Astronomy and Astrophysics, v.331, p.L1-L4 (1998), **331** (1998), L1. ISSN 0004-6361.

Snyder, G.F., Torrey, P., Lotz, J.M., et al. *Galaxy morphology and star formation in the Illustris Simulation at z = 0.* Monthly Notices of the Royal Astronomical Society, **454** (2015), 1886. ISSN 0035-8711.

Sobolev, V.V. *Moving envelopes of stars.* Harvard University Press (1960).

Stagner, L. *lstagner/ConcaveHull.jl* (2021).

Stevens, I.R., Kallman, T.R. *X-Ray Illuminated Stellar Winds: Ionization Effects in the Radiative Driving of Stellar Winds in Massive X-Ray Binary Systems.* The Astrophysical Journal, **365** (1990), 321. ISSN 0004-637X.

Stone, J.M., Norman, M.L. *ZEUS-2D: A Radiation Magnetohydrodynamics Code for Astrophysical Flows in Two Space Dimensions. I. The Hydrodynamic Algorithms and Tests.* The Astrophysical Journal Supplement Series, **80** (1992), 753. ISSN 0067-0049.

Sutter, P.M., Ricker, P.M. *Examining Subgrid Models of Supermassive Black Holes in Cosmological Simulation.* The Astrophysical Journal, **723** (2010), 1308. ISSN 0004-637X.

Svensson, R., Zdziarski, A.A. *Black Hole Accretion Disks with Coronae.* The Astrophysical Journal, **436** (1994), 599. ISSN 0004-637X.

Tananbaum, H., Gursky, H., Kellogg, E., et al. *Observation of a Correlated X-Ray Transition in Cygnus X-1.* The Astrophysical Journal, **177** (1972), L5. ISSN 0004-637X.

Thorne, K.S. *Disk-Accretion onto a Black Hole. II. Evolution of the Hole.* The Astrophysical Journal, **191** (1974), 507. ISSN 0004-637X.

Tinker, J., Kravtsov, A.V., Klypin, A., et al. *Toward a Halo Mass Function for Precision Cosmology: The Limits of Universality.* The Astrophysical Journal, **688** (2008), 709. ISSN 0004-637X.

Tomaru, R., Done, C., Ohsuga, K., et al. *The thermal-radiative wind in low-mass X-ray binary H1743-322: radiation hydrodynamic simulations.* Monthly Notices of the Royal Astronomical Society, **490** (2019), 3098. ISSN 0035-8711.

Tombesi, F., Cappi, M., Reeves, J.N., et al. *Evidence for ultra-fast outflows in radio-quiet AGNs. I. Detection and statistical incidence of Fe K-shell absorption lines.* Astronomy and Astrophysics, **521** (2010), A57.

Urry, C.M., Padovani, P. *Unified Schemes for Radio-Loud Active Galactic Nuclei.* Publications of the Astronomical Society of the Pacific, **107** (1995), 803. ISSN 0004-6280.

Van Rossum, G., Drake, F.L. *Python 3 Reference Manual.* CreateSpace, Scotts Valley, CA (2009). ISBN 1-4414-1269-7.

Virtanen, P., Gommers, R., Oliphant, T.E., et al. *SciPy 1.0: Fundamental Algorithms for Scientific Computing in Python.* Nature Methods, **17** (2020), 261.

Vogelsberger, M., Genel, S., Springel, V., et al. *Introducing the Illustris Project: simulating the coevolution of dark and visible matter in the Universe.* Monthly Notices of the Royal Astronomical Society, **444** (2014), 1518. ISSN 0035-8711.

Voit, G.M., Weymann, R.J., Korista, K.T. *Low-Ionization Broad Absorption Lines in Quasars.* The Astrophysical Journal, **413** (1993), 95. ISSN 0004-637X.

Walter, F., Weiss, A., Scoville, N. *Molecular Gas in M82: Resolving the Outflow and Streamers.* The Astrophysical Journal, **580** (2002), L21. ISSN 0004-637X.

Warner, B. *Cataclysmic Variable Stars.* Cambridge University Press (2003).

Weinberger, R., Springel, V., Hernquist, L., et al. *Simulating galaxy formation with black hole driven thermal and kinetic feedback.* Monthly Notices of the Royal Astronomical Society, **465** (2017), 3291. ISSN 0035-8711.

Weymann, R.J., Morris, S.L., Foltz, C.B., et al. *Comparisons of the Emission-Line and Continuum Properties of Broad Absorption Line and Normal Quasi-stellar Objects.* The Astrophysical Journal, **373** (1991), 23. ISSN 0004-637X.

Zel'dovich, Y.B. *The Fate of a Star and the Evolution of Gravitational Energy Upon Accretion.* Soviet Physics Doklady, **9** (1964), 195.

Zwicky, F. *Die Rotverschiebung von extragalaktischen Nebeln.* Helvetica Physica Acta, **6** (1933), 110. ISSN 0018-0238.